ABSTRACT

Title of Document:	CHARACTERIZATION OF HEAT TRANSFER AND PRESSURE DROP OF NORMAL FLOW HEAT EXCHANGERS IN COUNTER FLOW CONFIGURATION.
	Rohit S. Andhare, MS, 2014
Directed By:	Professor Michael.M.Ohadi

In today's times, successful technology advancement lies in making systems that are highly compact, offer superior energy efficiency, while sustainable and cost effective . There is interest in developing small heat exchangers having better flow distribution control rather than bulky heat exchangers which are energy intensive. Microchannels and microreactors controlled by microprocessors are slowly taking over energy conversion, transportation and process industry. The nature inspired − Fractal arrangement of manifold-microchannels has the potential to provide enormous heat transfer capabilities at an attractive coefficient of performance. However majority of such fractal flow manifolds are very short and operate with short counterpart microchannel. They have not been completely adopted for counter flow configuration required by majority of the industrial processes. The work covered under this thesis is focused on adopting of high performance fractal microchannel arrangement to counter flow configuration heat exchangers that are required by industrial processes. Two

single phase solution heat exchangers were developed using this approach. The solution heat exchanger is an essential component in absorption refrigeration cycle to convert waste heat into cooling. The study also utilized the novel additive manufacturing process of 3D printing to develop a tubular manifold in order to promote the fractal normal flow on tubular surfaces. The heat exchangers developed as a part of this thesis show enhancement in the overall performance and demonstrate high potential of the proposed technology.

CHARACTERIZATION OF HEAT TRANSFER AND PRESSURE DROP OF
NORMAL FLOW HEAT EXCHANGERS IN COUNTER FLOW
CONFIGURATION

By

Rohit S. Andhare

Thesis submitted to the Faculty of the Graduate School of the
University of Maryland, College Park, in partial fulfillment
of the requirements for the degree of
Master of Science
2014

Advisory Committee:
 Professor Michael M. Ohadi, Chair
 Professor Reinhard Radermacher
 Professor Marino diMarzo

To my Grandparents for their courage, faith, love and dedication

Acknowledgements

This thesis would not have come to fruition without the able guidance and support of my faculty advisor Prof. Michael M. Ohadi. His trust in my abilities gave me confidence and self-belief. I would also like to thank the Petroleum Institute of Abu Dhabi, ADGAS and GASCO for their sponsorship for this project. The financial support was critical for the successful completion of this study.

I would like to specially thank Dr. Serguei Dessiatoun, for being a mentor throughout my research experience. He has been generous to share his valuable knowledge accumulated over years of experience. He has been a constant source of encouragement and support which made my research experience truly pleasurable. His mentorship has played a major role in shaping me as an adept engineer. I will miss the firm hand shake which is his way of greeting students every morning at the lab.

I would also like to thank Dr. Amir Shooshtari for his guidance. His technical knowledge has helped me solve many conceptual problems which has also contributed to the successful completion of this thesis.

Finally, many of my colleagues contributed directly or indirectly to this work. I would like to specially thank Anupam Anand, Sahil Popli, Josh Fody, Meera Mahadevan, Vibhash Jha, David Boyea, Rapheal Mandel, Harish Ganapathy, Arjun Sharma and Dr. Kyosung Choo for making each day a pleasurable working experience at the lab.

Most importantly, I would like to thank the tremendous support of my fiancé – Foram Joshi and my beloved parents and grandparents for the tremendous belief and love. Their constant encouragement gave me strength to surmount daily challenges.

Table of Contents

List of Tables

List of Figures

Nomenclature

A	Area	m^2
C	Heat Capacity	J/K
Cp	Specific heat capacity	J/(kg-K)
D	Diameter	m
D_h	Hydraulic diameter	m
f,f_{Darcy}	Darcy's friction factor	
h	Heat transfer coefficient, height	$W/(m^2\text{-}K)$
hi	Inside heat transfer coefficient	$W/(m^2\text{-}K)$
ho	Outside heat transfer coefficient	$W/(m^2\text{-}K)$
ID	Inside or Internal diameter	m
k	Thermal Conductivity	W/(m-K)
l	Length	m
LMTD	Log mean temperature difference	°C
$\dot{m}$	Mass flow rate	kg/s
n	Number of passes	
Nu	Nusselt number	
OD	Outside or external diameter	m
P	Pressure	Pa
Perimeter	Perimeter	m
Q	Heat Transfer	W
Re	Reynold's number	

t	Thickness	m
T	Temperature	°C
U	Overall heat transfer coefficient	W/(m^2-K)
v	Velocity	m/s
w	Width	m
x*	Characteristic thermal entry length	

Greek Letters

α	Aspect ratio	
β	Chevron angle	Degrees
ε	Effectiveness	
ρ	Density	kg/m^3
φ	Diameter	m
μ	Dynamic viscosity	kg/(m-s)

Subscripts

hot	Hot side
cold	Cold side
in	Inlet
out	Outlet
inside,i	Inside or Internal
outside,o	Outside or external
channel	Microchannel
surface	Surface area
exp	Experimental

manifold	Manifold side
base	Heat exchanger base material
FD	Fully developed
actual	Experimental
flow	Flow cross section
pass	Manifold pass
mean	Averaged value
max	Maximum value
min	Minimum value

CHAPTER 1:   INTRODUCTION

This chapter introduces the research work covered under this thesis and provides potential gaps in research which this thesis has attempted to address.

1.1   Background, Motivation and Literature Survey

For effective performance of heat exchangers, direction of flow of fluid is critical. While under operation, orientation of flow determines the effectiveness and Log Mean Temperature Difference (LMTD). Depending on the, heat exchangers are broadly divided into three types:

1) Counter flow

2) Parallel Flow

3) Cross flow
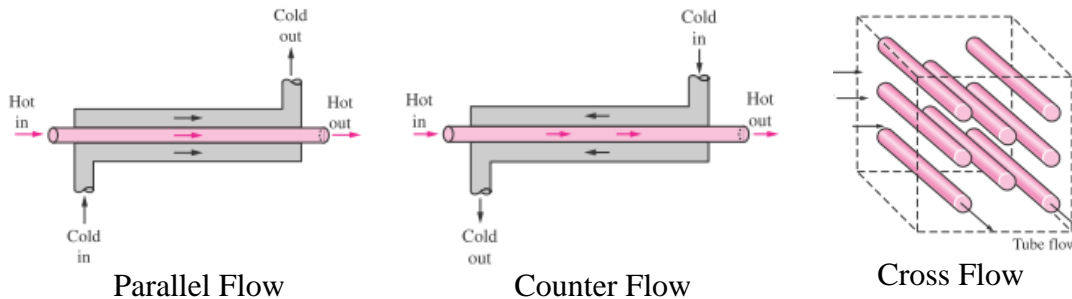
Figure 1-1: Types of heat exchangers based on orientation of flow [1]

In case of parallel flow heat exchangers, inlet or outlet of both fluids is at the same end of the heat exchanger. So, both fluids flow in the same direction from inlet side to outlet side. As a result, maximum temperature difference between both fluids occurs at inlet. This temperature difference and, as a consequence, the heat transfer

decreases as the flow moves from the inlet to the outlet. This puts a restriction on the maximum performance which can be availed from such type of a heat exchanger. It is for this reason, that parallel flow heat exchangers are relatively less preferred as compared to other flow configurations.

The counter flow heat exchanger as the name suggests, has both fluids flowing in opposing direction. Inlet of the hot fluid is on the same side as outlet of the cold fluid and vice versa. Because of such a configuration, a constant temperature difference value is maintained throughout the heat exchanger length. As a result, the heat transfer across the heat exchanger remains relatively constant throughout the length of the heat exchanger. This allows better utilization of heat exchanger surface area. Figure 1-2 below describes the temperature profile of both fluid streams for parallel and counter flow configuration.
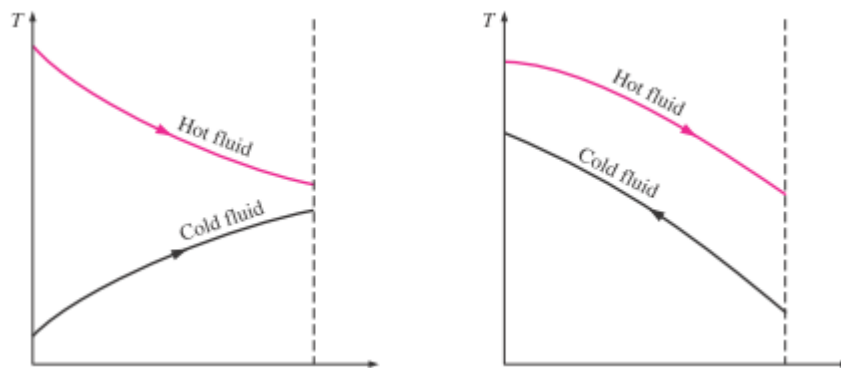
Figure 1-2: Temperature profiles of Parallel flow and Counter flow heat exchangers [1]

From the Figure 1-2 it may be observed that in a counter flow heat exchanger, for a given mass flow rate and specific heat capacity, it may be possible for the cold fluid at the outlet to attain a temperature higher than the hot fluid at the outlet. Such a condition is practically impossible for a parallel flow heat exchanger. Therefore, for the same flow rate and the same inlet and outlet temperatures, a larger size of heat

exchanger would be required while operating in parallel flow as against counter flow [1].

A third type of heat exchanger which is ideally suited for gas to liquid and gas to gas heat transfer is the cross flow heat exchanger. This heat exchanger has flow of both fluids in perpendicular direction or normal to each other. Such type of heat exchanger is used in car radiators, in shell and tube heat exchangers, condenser coils, air cooled condensers etc. It is also the only type of heat exchanger which has the orientation of both the fluid flow directions normal to each other. The cross flow heat exchanger is also known for its high surface area to volume ratio ($\geq$700m^2/m^3). The surface area to volume ratio of heat exchangers is a property which defines the compactness of the heat exchanger. For e.g. car radiators are cross flow heat exchangers. They have a surface area to volume ratio of almost 1000 m^2/m^3.[1]

For industrial processes and applications, the Shell and tube heat exchanger is commonly used. The heat exchanger consists of an external casing which is called the shell. Inside the shell, bundles of tubes are stacked which exchange heat with the fluid inside the shell. Baffles are provided to increase the number of passes which the shell side fluid makes as it exchanges heat with the tubes. This also provides a certain degree of cross flow as the fluid is made to flow perpendicular to the bundle of tubes. It is for this reason that the shell and tube heat exchanger is considered to have a cross-counter flow orientation. The provision of baffles enhances the heat transfer by increasing the effective length traveled by the fluid in the shells. If these baffles were not provided, in order to attain the same capacity, the heat exchanger would have to a larger heat transfer area. This indicates, that direction and orientation of flow has a significant impact on

size and performance of a heat exchanger The Figure 1-3 below shows a shell and tube heat exchanger having the cross-counter flow orientation.
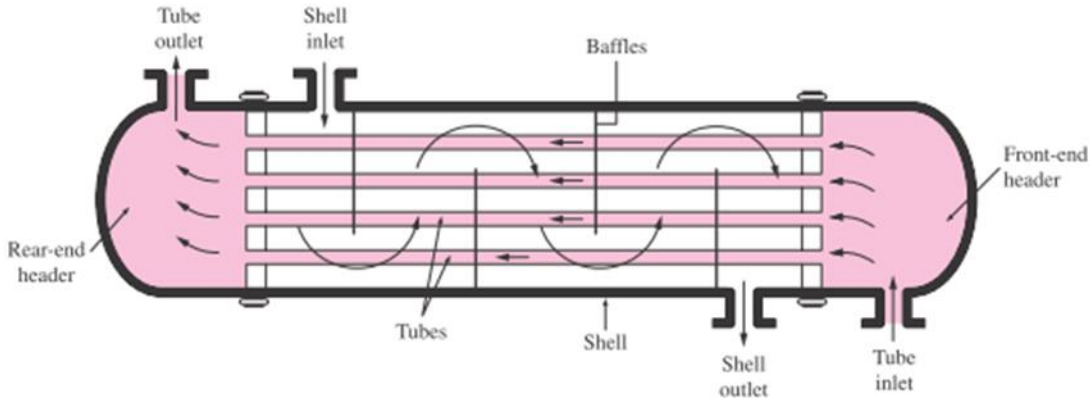
Figure 1-3: Multi-pass shell and tube heat exchanger [1]

Keeping these attributes in mind, many research works have been devoted to studying the effect of different flow orientations of heat exchangers. Vali et al. [2] studied the performance of a liquid to air heat exchanger having a counter-cross flow orientation. The Figure 1-4 [2] below shows the flow orientation studied by them for a plate heat exchanger.
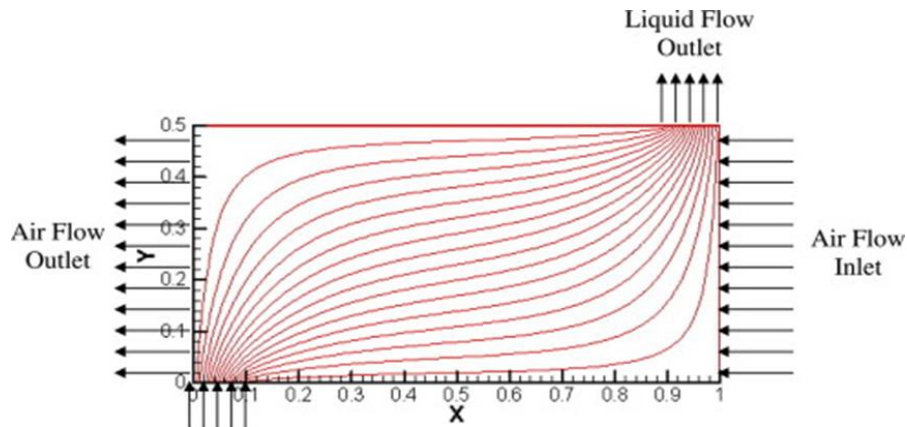
Figure 1-4: Cross-counter flow heat exchanger

Results obtained by them suggest that for the same heat transfer area, effectiveness of a counter-cross flow arrangement is higher than cross flow arrangement but lower as compared to counter flow arrangement. In another study,

4

conducted by Zhan et al. [3] the M-cycle – dew point cooling system was adopted to counter flow heat exchangers. The system was compared with a conventional cross flow model in order to observe the performance enhancement. The results show that counter flow arrangement offered around 20% higher cooling capacity as compared to the cross flow design. Kays et al. [4] developed a cross flow header as a feed mechanism for a larger counter flow heat exchanger.

Based on literature survey, the counter flow heat exchanger is preferable due to its greater thermal performance. As studies also suggest, attempts have been made to develop cross-counter flow configuration of heat exchangers, however, the general conclusion has been that the counter flow arrangement has superior performance.

An advantage of using cross flow design is the ease with which a flow distributing manifold may be implemented. This is because in cross flow heat exchangers the flow is oriented normal to the heat exchanging surface. Therefore, adapting a manifold to a cross flow heat exchanger such that it wets the entire heat transfer surface, is very convenient. On the contrary, using a manifold to distribute the flow for a counter flow heat exchanger may be difficult. The Figure 1-5 [5] below depicts how manifolds are used in cross flow heat exchangers:
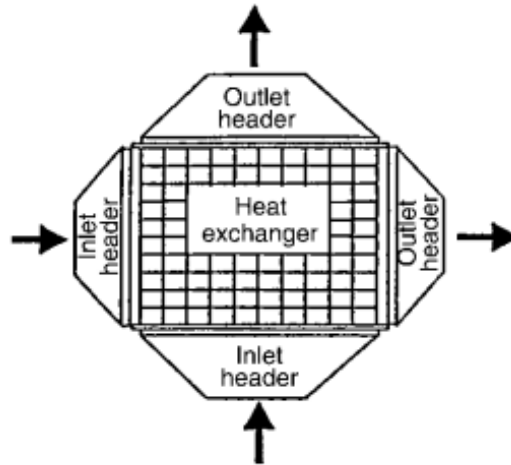
Figure 1-5: Cross flow heat exchanger with headers

One of the key purpose of this thesis is to develop a counter flow microchannel heat exchanger with normal flow feed using a manifold. By doing so, a mechanism for uniform flow distribution can be developed which improves the performance of the heat exchanger. This mechanism is known as Normal Flow Feed Mechanism (NFFM).

An important attribute of using a flow distributing manifold, is the ability to impart Fractal flow arrangement. Commonly prevalent in nature, this arrangement has the capability to evenly distribute flow throughout the heat exchanger, by successively dividing into smaller streams. The circulatory and respiratory system of mammals follows the same approach. The Figure 1-6 shows the fractal arrangement present in human circulatory system [6].
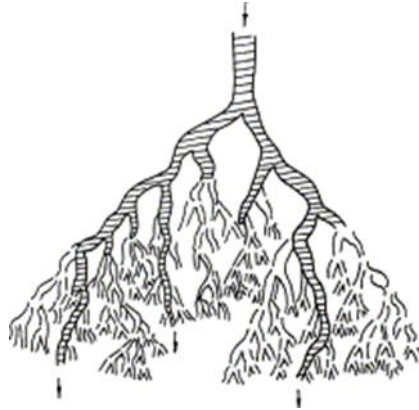
Figure 1-6: Fractal geometry in humans

The manifold which has been developed allows the flow to divide into two smaller streams. This division of flow is achieved through a baffled and multi-pass arrangement of the manifold. The detailed description of this arrangement is provided in the CHAPTER 2:. Literature survey suggests that Fractal flow arrangement has been applied to manifold-microchannel systems in the past. Chen et al. [6] concluded that the fractal arrangement for microchannel heat exchangers can increase heat transfer performance as well as reduce pressure drop. Similarly, Wang et al.[7] observed that there were significant benefits of flow and temperature distribution by using fractal arrangement for microchannel heat sinks.

Studies suggest that Fractal flow arrangement is limited to electronics cooling applications such as microchannel heat sinks which typically have small flow lengths. Such microchannel heat sinks are inherently configured to have parallel flow. In a heat sink, the objective is to maintain the base temperature to a constant value. Thus, achieving uniform temperature distribution is critical. This can only be made possible by using a proper flow distribution mechanism. As the heat transfer fluid, exchanges heat with the base of the heat sink, it tries to achieve the temperature of the base. This

7

relationship between base temperature and fluid temperature is similar to a parallel flow heat exchanger.

In order to expand the arrangement to a large scale counter flow heat exchanger, a multi pass arrangement was designed. In such a case, every pass of the manifold microchannel heat exchanger acts as an independent heat sink. This was applied to single phase microchannel heat exchangers and these heat exchangers were experimentally tested with water on both sides. The application of manifold microchannel arrangement offers significant volume reduction while maintaining the thermal performance. Another advantage is the potential of reducing pressure drop in the heat exchanger. This is possible because by using the manifold microchannel in fractal flow arrangement, the entire microchannel is divided into smaller flow lengths. This contributes to the reduction in pressure drop. The description of this type flow arrangement is explained further in CHAPTER 2:.

1.2   Literature Review on Microchannel Heat Exchangers

Microgrooved surfaces have proved effective for high heat flux applications. In addition to these benefits, micro-channel heat exchanger also provide high surface area to volume ratios and low cooling fluid requirements which makes the heat exchangers more compact and economical to use. There exists plenty of study devoted to investigating flow and heat transfer characteristics of micro-channel heat exchanging surfaces.

Tuckerman and Pease [8] developed an embedded water cooled heat sink which initiated research interest in microchannels. The heat sink developed by them used the high aspect ratio of microchannels to increase the surface area which lead to decrease

in the thermal resistance. Samalam [9] conducted a mathematical investigation of the governing equations for high aspect ratio and low aspect ratio microchannel heat sinks. In other relevant works considerable number of correlations have been developed by researchers to study the characteristics of heat transfer performance and frictional factor. Adams et al. [10] [11] studied the effect of turbulent flow in circular and non-circular microchannels. The hydraulic diameters for the circular microchannels were in the range of 0.76 mm to 0.109 mm. The study concluded with a correlation for the Nusselt number which is a modified version of the Gnielinski [12] correlation for turbulent flow in channels. Lee et al. [13] experimentally investigated single phase heat transfer and pressure drop in rectangular microchannels ranging from (194-534 microns). The results obtained by them were validated by a numerical analysis. Harms et al. [14] also conducted experiments on rectangular channels to observe the heat transfer and pressure drop in microchannels. Grigull and Tratz [15] demonstrated the variation of the Nusselt Number with Graetz Number for different temperature gradients. Rahman et al. [16] conducted an investigation to observe the flow and heat transfer characteristics in different microchannel geometries such as I-channel and U-channel. The experimental results obtained were much higher than correlations developed for larger channel diameters. Owahib and Palm [17] conducted experiments using R134a for single phase flow and heat transfer in circular channels. They reported that the experimental results were in good agreement with the classical correlations for channel flow. However, their data did not match any of the correlations developed by other researchers. Papautskey et al. [18] conducted experiments to obtain the pressure drop in microchannels. They reported an early transition to turbulent flow conditions

in microchannels. Moreover, their observation was that the friction factor in microchannels was found to be 20% higher than theoretical predictions. Peng et al. [19] conducted an experimental study to observe the heat transfer and flow characteristics of methanol in rectangular channels fabricated on a flat plate. They studied the effect of different parameters such as fluid velocity, fluid properties and microchannel geometry on the thermal and flow characteristics of the microchannels. Their results seem to suggest that there exists a transition region beyond which the heat transfer coefficient is independent of wall temperature. In another study by Wang and Peng [20], the authors reported that the transition to turbulent region is dependent on the liquid temperature, velocity and microchannel size. In general, many uncertainties lie in the literature with regards to performance of single phase flow in microchannels. This is summed up correctly by Kandlikar et al. [21] in an article on the research needs in microchannel flow research. There is no doubt about the fact that heat transfer performance enhancement does result from the reduction in the hydraulic diameter of the microchannel. This is what has been reported in the literature survey as well. However, the fact remains that there is still no general consensus on the performance characteristics of microchannels. While some research suggests that the classical correlations are applicable to microchannels. Many experimental results have deviated from the theoretical predictions. Additionally, the actual transition from Laminar to Turbulent flow conditions still remains uncertain. Many summary and review papers have reported such observations with regards to single phase flow research for microchannels. Palm [22] conducted a summary on the single phase and two phase flow correlations reported on literature. The author also provided explanations on the

possible reasons for deviation of the results from classical theory. According to Palm [22] one of the reason could be due to the difficulty and uncertainty in measurements due to the micro scale level of investigation. Sobhan and Garimella [23] have also created an exhaustive summary on the different correlations which have been obtained by researchers for different working fluids, channel shapes and single phase and two phase flows. In their review as well, the authors demonstrated wide discrepancies between the experimental and theoretical predictions. Although, discrepancies exist, a majority of the research suggest significant enhancement in thermal performance due to single phase flow in microchannels. In order to summarize all the related works carried out by different researchers, the Figure 1-7 and Figure 1-8 given below show the different correlations on a single graph. These graphs were compiled by Sobhan and Garimella [23] . The first set of graphs show the variation of friction factor:

(a)

(b)
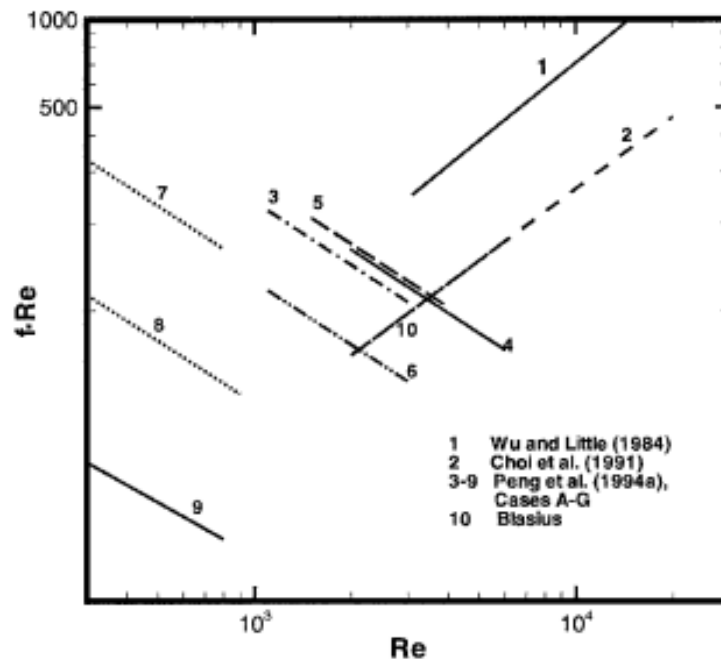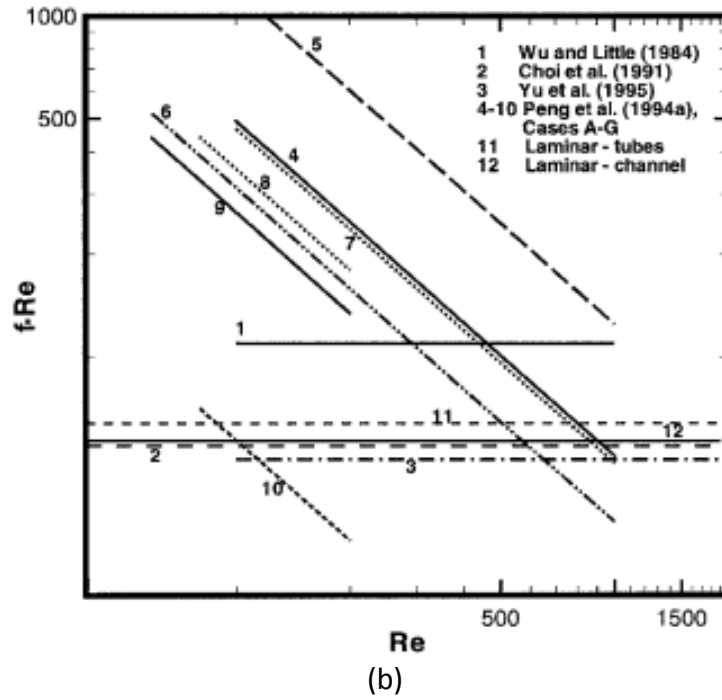
Figure 1-7: Correlations forPoisuelle number (fRe) for microchannels for (a) Laminar flow and (b) Turbulent flow

The Figure 1-8 below shows variation of Nusselt number as reported by

different studies [23]:

(a)
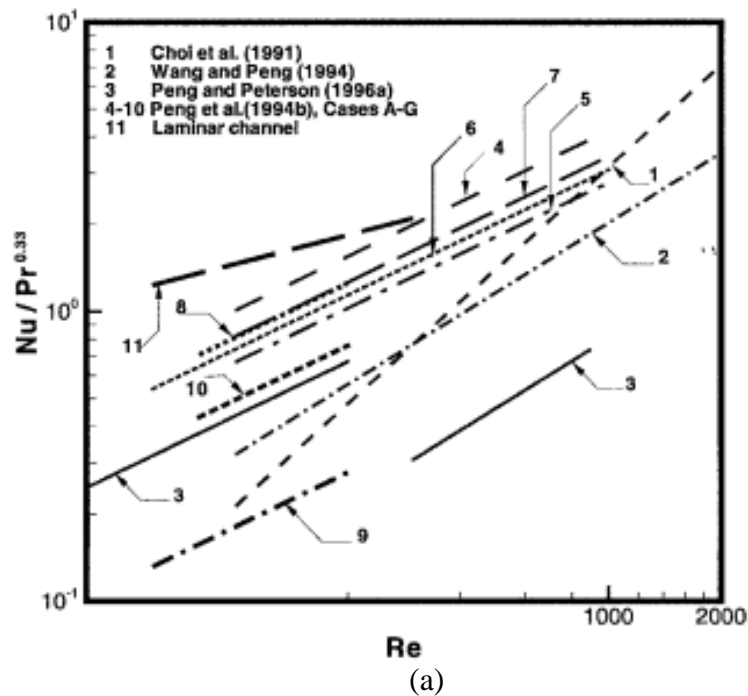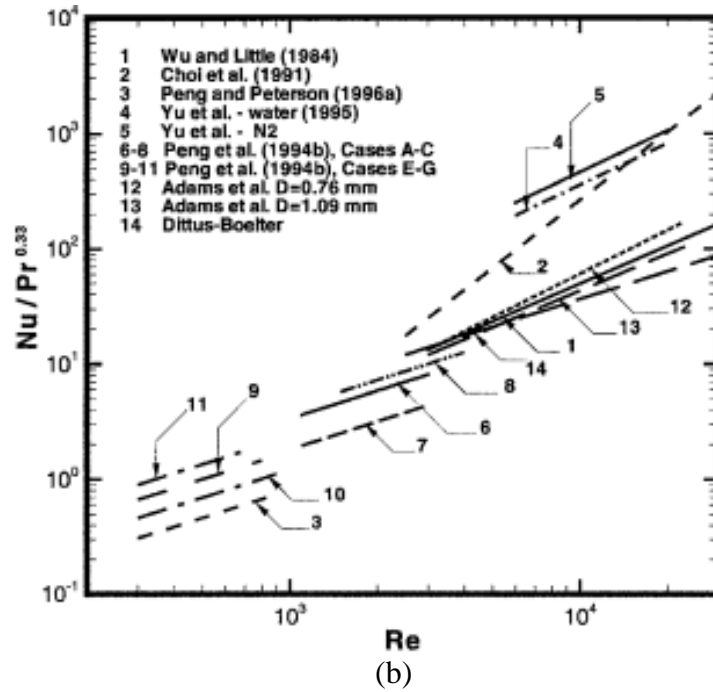
Figure 1-8: Correlations for Nusselt number for microchannels for (a) Laminar flow (b) Turbulent flow

One of the limiting factors which has prevented the entry of microchannel heat exchangers in the industrial, processing and energy sector is pressure drop.

$$\Delta P = \frac{\rho f_{Darcy} l v^2}{2D}$$ **Eq. 1**

For Laminar flow in circular tubes,

$$f_{Darcy} = \frac{64}{Re} = \frac{64 * \mu}{\rho v D}$$ **Eq. 2**

Substituting this in Eq. 1 we get:

$$\Delta P = \left(\frac{\rho l v^2}{2D}\right) * \left(\frac{64\mu}{\rho v D}\right) = (32\mu l) * \left(\frac{v}{D^2}\right) \qquad \text{Eq. 3}$$

$$v = \frac{\dot{m}}{\rho A_{flow}} \qquad \text{Eq. 4}$$

Substituting v in the Eq. 4 we get:

$$\Delta P = \frac{128\mu l \dot{m}}{\pi\rho} * \left(\frac{1}{D^4}\right) = \frac{constant}{D^4} \qquad \text{Eq. 5}$$

This equation (Eq. 5) suggests that for the same mass flow rate and channel length, as the microchannel size is reduced, the pressure drop increases by the fourth power of the hydraulic diameter. This is where the concern lies. This research has attempted to address this problem by utilizing normal fractal flow which is capable of reducing the pressure drop by dividing the microchannel into smaller flow lengths. Detailed explanation of this mechanism is provided in CHAPTER 2:.

1.3   Waste heat recovery systems

According to U.S. Department of Energy, the Industrial sector accounts for about one-third of the total energy consumption in the U.S. According to their estimates close to 20-50% of this energy is wasted to the atmosphere in the form of cooling water, exhaust gases and other emissions [24]. Therefore, there exists a tremendous opportunity to recover this waste heat and utilize it for operating energy systems or for energy storage. It is estimated that by improving waste heat recovery, energy efficiency can be increased by 10-50%. [24]

The source of such waste heat is usually from exhaust for generator sets and furnaces, steam discharge of thermal power plants or exhaust from gas turbine plants

etc. Usually, any function which involves combustion of fossil fuels has a waste heat associated with it. In many applications, waste heat may also be utilized from solar thermal collectors and be used for cooling building environments. Different kinds of heat driven systems may be operated using this waste heat. Some of the prominent systems which may potentially be used are indicated Figure 1-9 below:
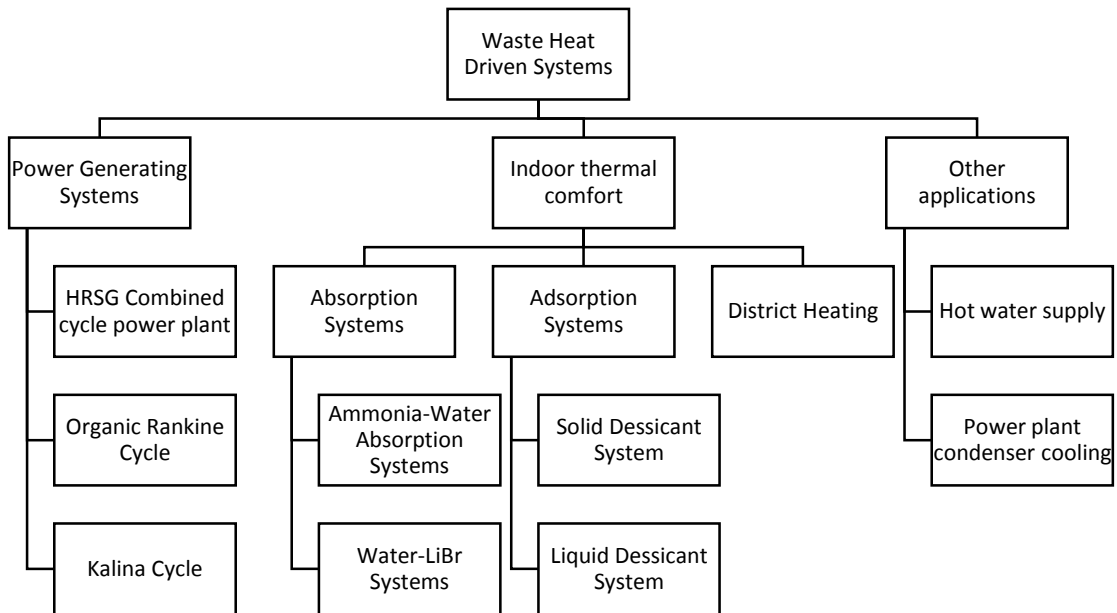
Figure 1-9: Waste heat recovery applications

Many ongoing projects in this area indicate the relevance utilization of waste heat has in the current global scenario. For example, EPRI [25] is working in collaboration with Allcomp, to develop a green chiller which would run by utilizing the waste energy recovered from discharged steam from the thermal power plant turbine. The tightening of emission regulations and increasing fossil fuel prices have generated significant interest in developing waste heat recovery systems. By doing so, higher levels of energy efficiency would be attained which would ultimately reduce fuel consumption. For example, a stand-alone gas turbine power plant would have an

efficiency of about 25-30% [26]. However, when a combined cycle is used where the un-utilized energy discharged from gas turbine is used to drive a steam power plant, efficiencies close to 50-60% [26] and above may be achieved. This ensures optimum utilization of the fuel and has the potential to lower operating costs. In spite of the increasing interest in waste heat driven systems, the fact remains that the waste heat obtained is low grade energy i.e. it is a high entropy form of energy. Therefore, in order to extract any useful energy, the waste heat temperature needs to be substantially high. Based on the temperature waste heat recovery systems can be divided into High, Medium and Low energy systems. This is as shown in the Table 1-1 [27] below:

Table 1-1: Grades of waste heat based on temperature.

Category	Source	Temperature (°C)	Advantages & Disadvantages	Typical recovery methods
High (> 650 ºC)	Glass melting furnace	1300-1540	High quality energy, high heat flux, higher power generation	Steam generation
	Steel electric furnace, etc.	1370-1650		
	Hydrogen plants	650-980	Thermal stresses on heat exchanger components, and increased chemical activities	Combustion air preheats, etc.

	Gas turbine exhaust	370-540	More compatibility with heat exchanger materials, Practical for power generation	Steam generation,
Medium (230-650 ºC)	Steam boiler exhaust	230-480		Organic Rankine cycle, etc.
	IC engines ,etc	320-590		
Low (< 230 ºC)	Exhaust gases from gas-fired boilers, ethylene furnaces, etc.	70-230	Large quantities available from numerous product streams.	Space and domestic water heating Upgrading heat Organic Rankine cycle.
	Cooling water from furnace doors, IC engines, air compressors or refrigerant condensers	30-120		

Although theoretically, extracting and utilizing waste heat may be a simple process, practically, it is not as easy. One of the concern is supply of adequate waste heat. Moreover, equipment size and cost associated with this process may be substantially higher and may involve longer payback periods. Furthermore, COP (Coefficient of Performance) of waste heat driven systems is also quite low. But considering that the energy supplied is actually free or would have been wasted if not utilized, gives such systems some relevance. Thus, developing waste heat recovery

systems is a trade-of between the amount of energy available against the capital cost for the set up and ultimately how much energy is actually going to be delivered as useful energy.

Absorption systems are one type of heat driven systems. Their working principle is based on the property of certain compounds to readily dissolve or absorb water at different concentrations depending on the temperature. As the temperature increases i.e. when heat is supplied the concentration decreases and so desorption takes place. As temperature decreases, absorption process takes place. This absorption and desorption process together constitute a thermally driven compressor system. A typical absorption cycle is shown in the Figure 1-10 below [28]:
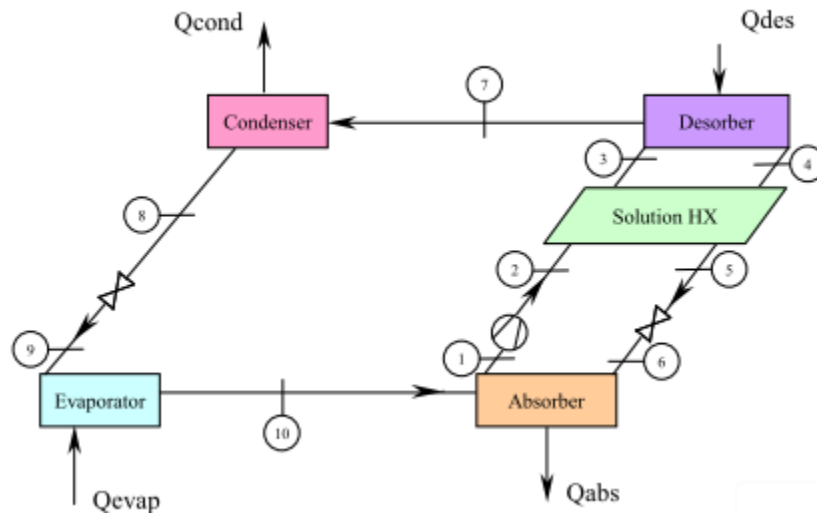
Figure 1-10: Typical ammonia - water absorption refrigeration system

The loop on the right, which shows the absorber and the desorber, performs a function similar to a compressor in a typical vapor compression cycle. The waste heat necessary to drive this system is provided at the desorber where the refrigerant separates from the absorbing solution. Similar to a vapor compression cycle, the condenser condenses the refrigerant vapor and the evaporator provides the cooling. In

18

the solution loop, the solution leaving the absorber is a low temperature high concentration solution while the solution leaving the desorber is low concentration and high temperature. This provides an opportunity to exchange heat between these two lines. By doing so, it would be possible to pre heat the rich solution before it enters the desorber. This reduces the total heat input required to operate and maintain the capacity of the system. This exchange of heat between the two solution lines is facilitated by a solution heat exchanger. Depending on the refrigerant and absorbent combination, vapor absorption cycles are divided into two:

1) Ammonia water Absorption cycle (Ammonia is the refrigerant water is the absorbent)

2) Water – LiBr Absorption cycle (Water is the refrigerant and LiBr is the absorbent)

The difference between the two systems is provided in the Table 1-2 [27] below :

Table 1-2: Difference between water - LiBr cycle and Ammonia-water Absorption refrigeration system

Water/Lithium bromide chillers	Ammonia water chillers
Has been widely used since 1950's	Used since late 1800's. Used for ice production prior to vapor compression technology
Water is refrigerant. Doesn't require rectifier due to low vapor of salt.	Ammonia is used as refrigerant. Requires rectifier as water is volatile.
Typically used as water chillers for air condition applications. Main competing technology is vapor compression chillers.	Large tonnage industrial applications requiring low temperatures for process work. Also sold as air-cooled and gas-fired air conditioning component, Solar cooling.

0.7 < COP < 1.2	Typically around 0.5. However, triple effect - two stage - absorption air conditioner can show a COP of 1.7 too.
Cannot operate below zero and dangers of crystallization. Works at sub atomic pressures.	Can work at much lower temperatures. Works at higher pressures.
Mostly compatible with all materials. But corrosion can be a concern due to presence of aqueous salt solution. Good compatibility with most rubber and polymer compounds.	Ammonia is toxic at high ppm and not compatible with copper. But is inexpensive, environmentally compatible and have excellent thermodynamic properties.

It is important to note here that the COP of a vapor absorption system ranges from 0.5-1. Since, Absorption systems are essentially thermally driven systems, this COP is calculated based on the total heat input as against the electric power input in vapor compression cycles.

$$COP_{abs} = \frac{Q_{evap}}{Q_{des}}$$
<div align="right">**Eq. 6**</div>

As a part of this project, the aim is to develop a solution heat exchanger for an ammonia-water absorption system which would provide excellent thermal transport, resist corrosive effects of ammonia, have low pressure drops and would be compact and light. The objectives and contributions in this project has been described in the succeeding topic.

1.4   Objective

As described earlier, the aim of this thesis is to adopt the fractal flow arrangement which is typically used for manifold microchannel heat sinks, to counter flow large scale heat exchangers. This has been carried out by developing a manifold which provides fractal arrangement by orienting the feed to the microchannels in the normal direction to the surface of the heat exchanger. The Figure 1-11 below describes this arrangement. [27]
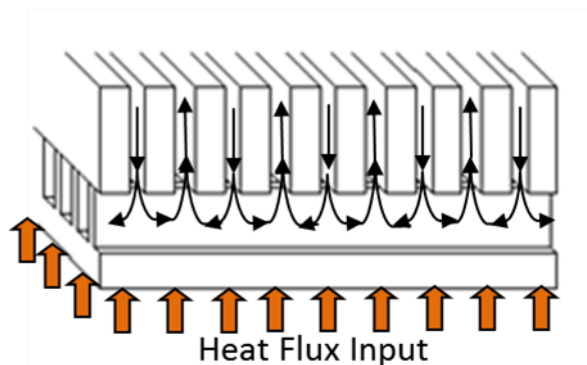
Figure 1-11: Manifold - microchannel normal flow feed mechanism with fractal flow arrangement

In order to expand this micro-scale arrangement to large scale heat exchangers, a multipass manifold was conceptualized. The manifold provides normal flow to the heat exchanger base and therefore this mechanism is named as Normal Flow Feed Mechanism (NFFM). The single phase heat exchangers developed through this approach were developed for their application as solution heat exchangers for a waste heat recovery system which uses ammonia water absorption refrigeration cycle. The objective of the project was to develop an 11 kW solution heat exchanger by using

NFFM. The pictorial representation of the ammonia water absorption refrigeration cycle shows the current focus of this project (Figure 1-12):
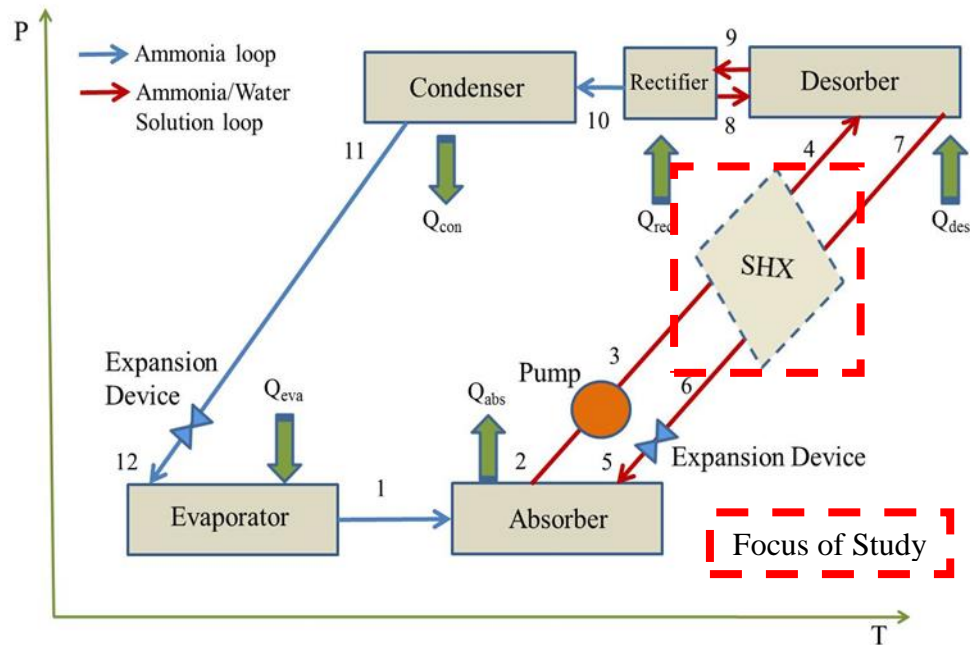
Figure 1-12: Focus of study - Solution heat exchanger

The following contributions were made towards this project:

1) Developed a counter flow flat plate microchannel solution heat exchanger with a flat 20 pass manifold. The manifold provides the Normal flow to the base of the microchannel. The development of this heat exchanger has been described in CHAPTER 3:. Results obtained through experimental tests were validated with numerical simulations

2) A counter flow tubular microchannel heat exchanger prototype was also developed. The manifold for this unique tubular heat exchanger was developed from 3D printing. Since the manifold is not required to have high thermal properties, it is possible to develop the manifold from polymer based materials. This gives scope to technologies such as additive manufacturing or 3D printing

22

to be involved in development of high performance heat exchangers. This has been discussed in detail in CHAPTER 4:.

In order to test the heat exchangers, the following (Table 1-3) test conditions were provided. The heat exchangers were tested in lab using water on both sides. The Figure 1-13 shows the temperature gradient of both the hot and the cold fluid across the heat exchanger. Although the temperatures mentioned in the table go beyond 100°C, for in-lab testing with water, the maximum temperature was kept below 30-32°C. The flow rates were varied within the range specified in the Table 1-3[29].

Table 1-3: Absorber state points

Direction	Temp (C)	Pressure (kPa)	Mass Flow (kg/s)
From Absorber	78.2	3160.52	0.0867875
To Desorber	141.1	3153.63	0.0874818
To Absorber	82.2	3043.31	0.075852
From Desorber	156.7	3060.21	0.075852
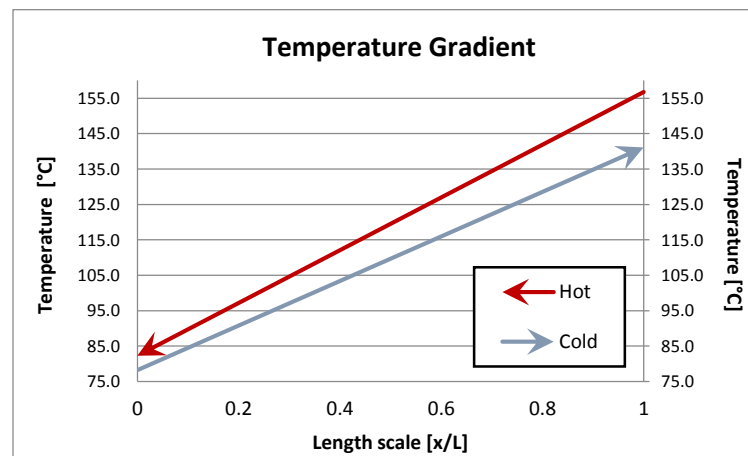
Figure 1-13: Temperature gradient of fluids across the heat exchanger length

To summarize, the following points have been the motivating factor behind the research and development for this thesis:

23

1) Manifold microchannel heat exchangers which use fractal flow arrangement offer high heat transfer performance and reduce pressure drop. They also provide enhanced flow distribution which also contributes to performance enhancement.

2) Fractal flow enabled manifold microchannel systems are easily possible in cross flow configuration. Additionally, manifold-microchannel heat sinks demonstrate parallel flow configuration. The implementation of such an arrangement for counter flow configuration is not easy.

3) Moreover, the manifold microchannel arrangement is typically used for small flow lengths in electronics cooling applications where flow distribution and temperature distribution is critical to reduce hot spots.

4) In order to expand this approach to large scale counter flow heat exchangers, a multi pass manifold microchannel system was designed which was capable of providing fractal normal flow to the microchannels

5) Most of the earlier designs of heat exchangers which were developed in lab using the manifold microchannel approach were two phase heat exchangers.

6) To the best knowledge of the author, this is the first time that manifold microchannel heat exchangers have been designed and tested in counter flow arrangement.

7) The heat exchangers which were developed were for application as solution heat exchangers in ammonia water absorption systems for waste heat recovery

8) Two solution heat exchangers: a flat plat and a tubular prototype version were built using this unique flow arrangement and were tested with water on both sides.

CHAPTER 2:   NORMAL FLOW FEED

MECHANISM

In spite of all potential benefits published by all investigators, there exists one aspect of microchannel heat exchangers which particularly puts a limitation on its use. This is the increased pressure drop which occurs due to the reduction in flow area. In electronics cooling applications this problem is less important because for microscale heat exchangers, the flow lengths are shorter and so pressure drop is also small. However, in an effort to expand the use of microchannel heat exchangers to large scale – low heat flux applications, limiting pressure drop becomes all the more critical.

Another question which still remains unanswered is how to implement a fractal normal flow mechanism to a counter flow heat exchanger. Implementing a proper feed mechanism for microchannels is also important. Because of small size of channels, distributing the flow equally and sufficiently to all channels is a challenge. Bo et al. [30] obtained a 14.8% increase in cooling capacity due to improved flow distribution for a microchannel heat exchanger. In another numerical study, conducted by Boteler et al.[31] a manifold microchannel cooler was found to enhance heat transfer coefficient by 50%. The study also found substantial reduction in pressure drop and uniform surface temperature distribution. This observation was also supported by the results reported by Ryu et al. [32] According to their study, thermal resistance of a manifold microchannel heat sink was 50% lower as compared to a traditional microchannel cooler when operated at same pumping power and heat flux condition.

Looking into these inherent benefits associated with flow distribution, a unique multipass manifold was developed. By using this manifold it was possible to expand

the short normal flow heat sinks, to large scale counter flow heat exchangers. This is mechanism of flow feed is called the Normal Flow Feed Mechanism (NFFM). This approach uses a manifold which branches the flow into smaller channels and distributes it to the microchannels. The manifold sits on top of the microchannels in the manner shown in the Figure 2-1 below:
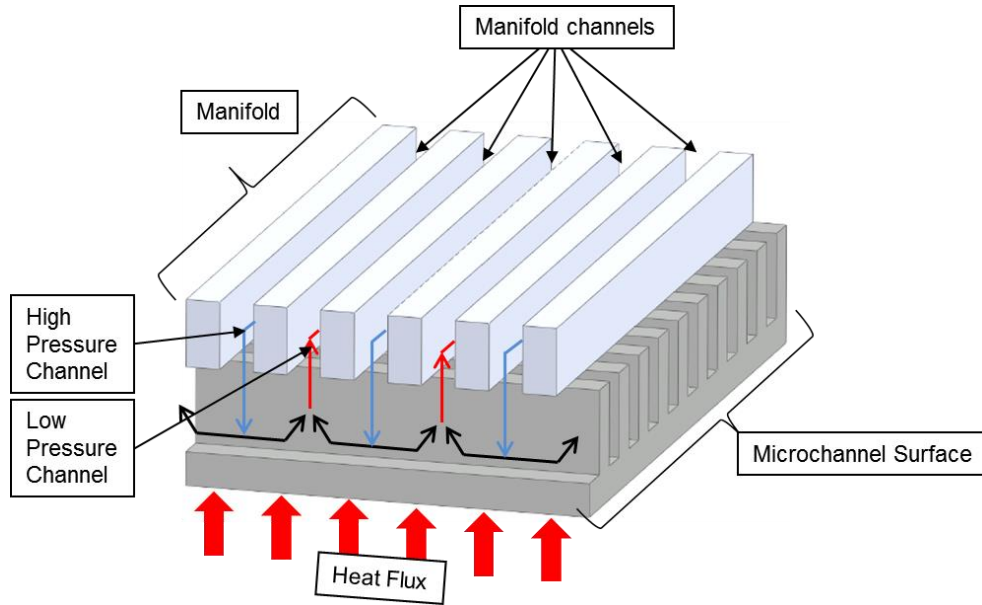
Figure 2-1: Normal Flow Feed Mechanism (NFFM)

The manifold consists of a series of channels. Every alternate channel is blocked using a baffle. This allows entry of fluid in only half of the channels. These open channels may also be called "high pressure channels". As fluid enters these channels, high pressure of the fluid forces it into the microchannels. While going from the manifold channel to the microchannels, the fluid encounters its first 90° bend accompanied by a reduction in the flow area. The fluid enters the microchannels from a direction which is normal to the base of the microchannel and hits the base. This creates a stagnation zone near the base where conductive heat transfer through the fluid media dominates the thermal transport phenomena. As the fluid moves through the

27

microchannel high static pressure of imparts momentum to the fluid as it moves through the constricted microchannel area. This increased velocity not only increases pressure drop but also contributes to a considerable increase in heat transfer coefficient. As the flow nears the outlet manifold, it encounters another stagnation zone. The fluid undertakes another 90° bend and enters the manifold. A fourth 90° bend takes place as the fluid orients itself to flow through the "low pressure channel". The fluid from rest of the microchannels is collected by this low pressure channel. This entire process completes one pass of a manifold microchannel using normal flow feed mechanism.

Based on the description and on the Figure 2-1, a few conclusions can be made about the characteristics of this kind of flow mechanism. The Figure 2-1, resembles a one side of the entire heat exchanger. This is similar to a manifold microchannel heat sink having a constant heat flux or constant surface temperature boundary condition. The temperature profile of the fluid as it flows through the heat sink resembles a parallel flow heat exchanger. Since the main objective of a heat sink is to maintain a the temperature of electronics, cold fluid which enters the heat sink exchanges heat with the base and tries to achieve the temperature as close as possible to the base temperature. The Figure 2-2 below describes temperature profile clearly:

(a)   (b)
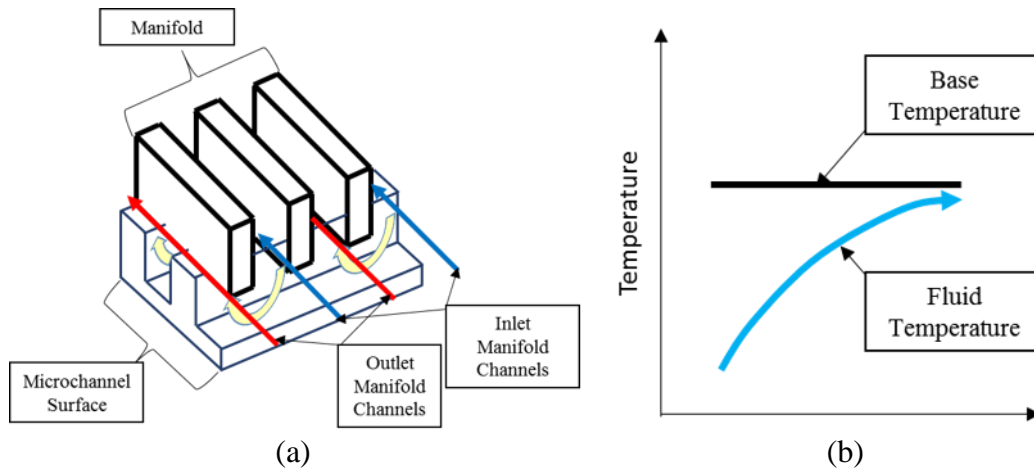
Figure 2-2: (a) Manifold microchannel heat sink (one pass); (b) Temperature profile of manifold microchannel heat sink

To expand this design to a heat exchanger, a multipass arrangement would be required. This can be done by arranging individual heat sinks in a series such that the outlet of the heat sink would provide the inlet for the next pass. This arrangement is shown in the Figure 2-3 below:
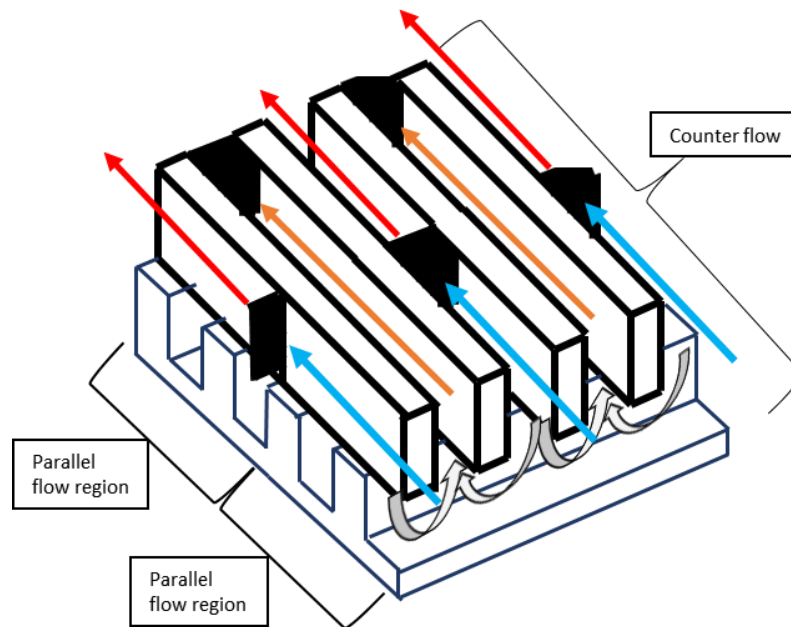
Figure 2-3: Multipass manifold microchannel heat sink

As described in the figure above, the high pressure manifold channel in the previous pass is blocked by a baffle. While the manifold channel which had low pressure in the previous pass now has all the collected fluid and is therefore a high pressure manifold channel in the next pass. The Figure 2-4 below shows the working mechanism of the normal flow feed mechanism.
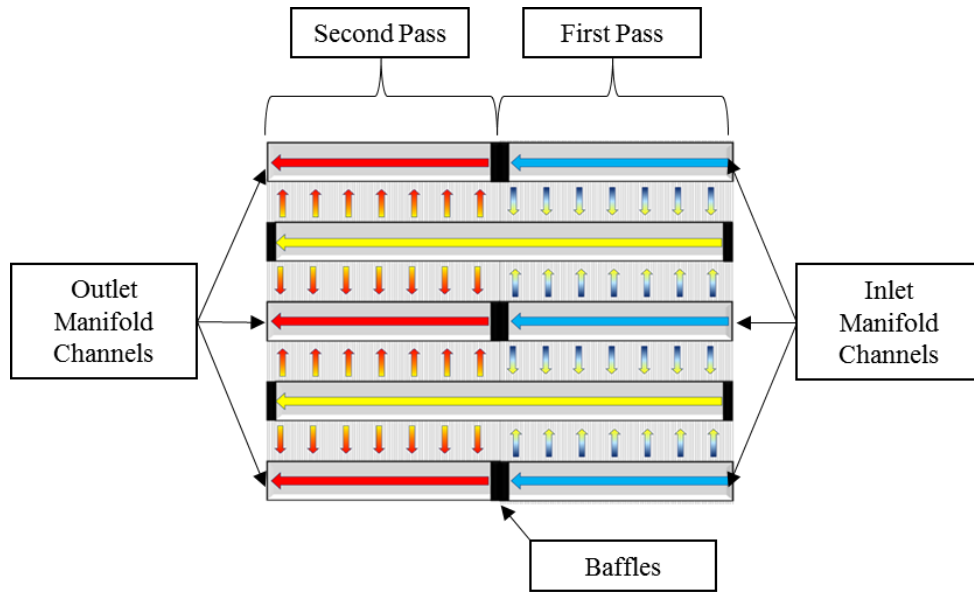
(a)
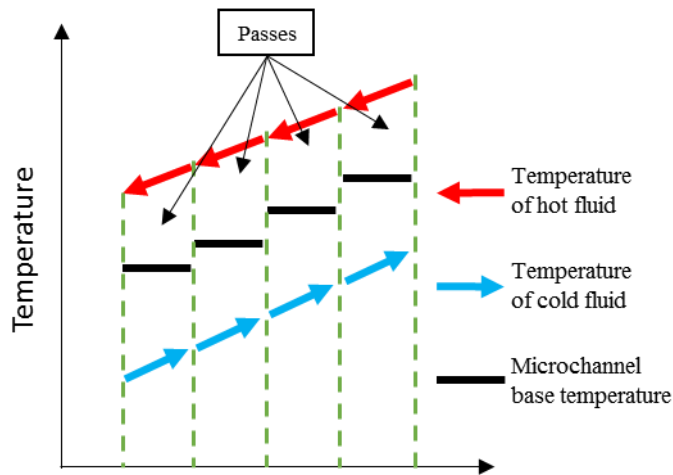
(b)

Figure 2-4: NFFM using a manifold

The temperature profile obtained in the Figure 2-4 is when a fluid is used on the other end to transfer heat across a conducting surface – namely a heat exchanger. More importantly, the temperature profile is characteristic of a counter flow heat exchanger. In order to assess the flow of fluid through a single microchannel was observed through simulations.
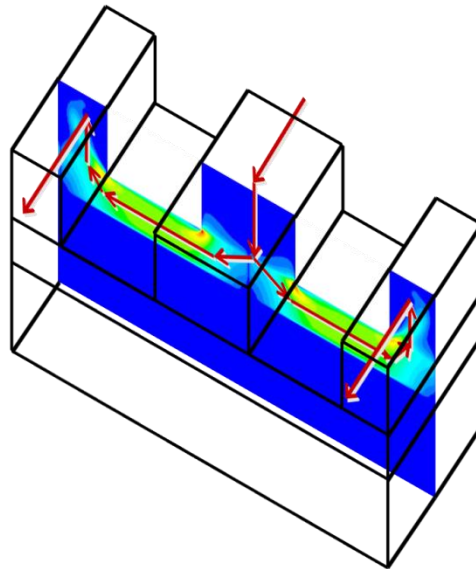
Figure 2-5: Flow of fluid through microchannels by using NFFM

The contour plot in Figure 2-5 above was taken from one of the simulation results clearly shows the flow of the fluid through the manifold and the microchannel. This normal flow feed mechanism was adopted to both the solution heat exchangers i.e. The flat plate heat exchanger and the tubular heat exchanger. The performance enhancement obtained due to this arrangement was later compared with conventional state of the art heat exchangers such as chevron plate heat exchanger.

The bullet points below summarize the possible reasons for the enhancement of thermal performance of the microchannel heat exchangers due to the Normal Feed Flow Mechanism:

1) As the fluid moves from the manifold to the microchannel, the fluid is induced into the developing region. As a consequence, the heat transfer coefficient in this region would be higher than the heat transfer coefficient for fully developed flow. So, as the flow is made to pass through a number of short microchannel sections, the fluid repeatedly enters the developing flow regime. This first point explains the enhancement of heat transfer.

2) Due to the two 90° bends in the flow from the manifold to the microchannel and out to the manifold, the flow attains a component of centripetal acceleration. This centripetal acceleration pushes the fluid against the base of the microchannel, which causes the shearing of the viscous layers formed close to the base of the microchannel. This influences the heat transfer coefficient at the base. The Figure 2-6 below describes this centripetal motion of the fluid through the microchannels.
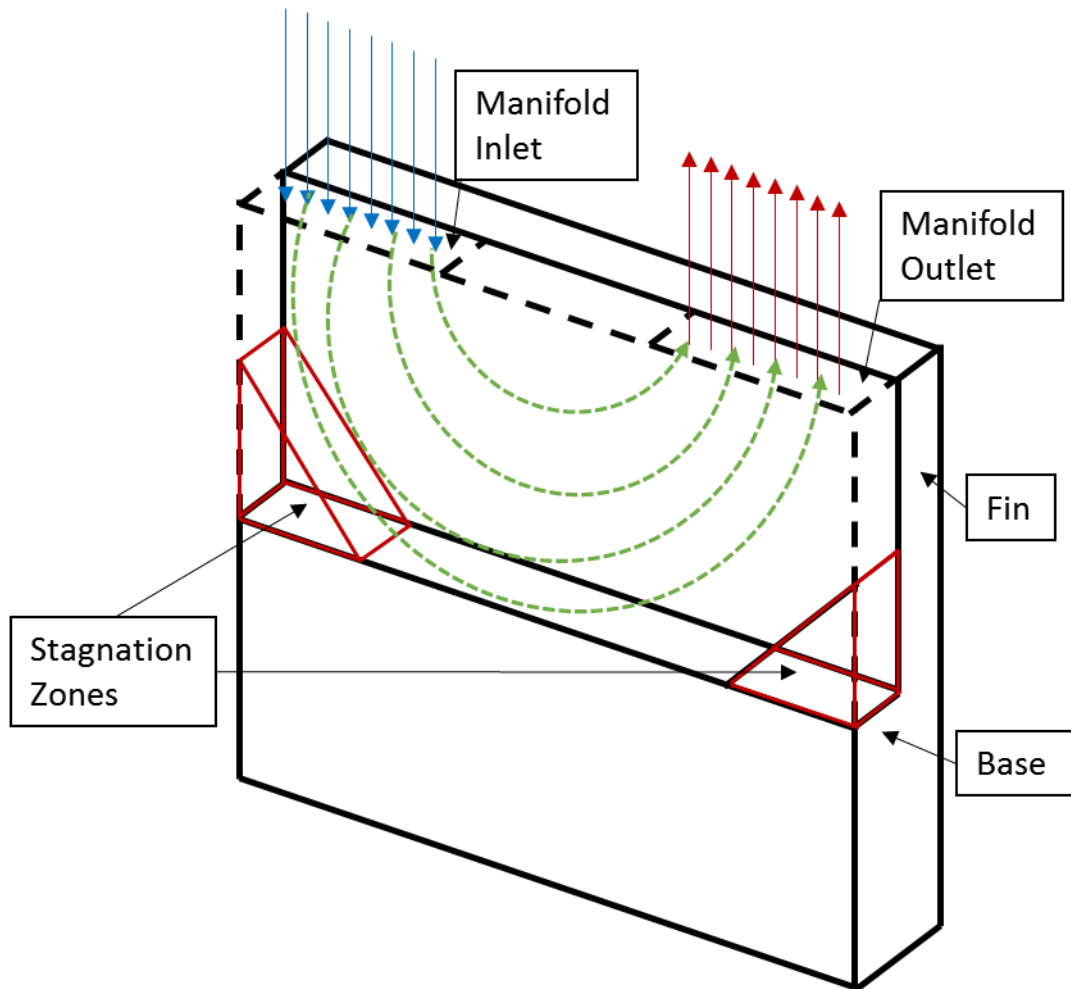
Figure 2-6: Centripetal motion of flow by using NFFM

3) Increase in velocity due to reduction in the flow area is also one of the contributors of high thermal performance. The reduction in area results in high flow velocities which shears the laminar sub layer near the surface of the wall. This further enhances thermal transport.

CHAPTER 3: COUNTER FLOW FLAT PLATE MICROCHANNEL HEAT EXCHANGER

The heat exchanger discussed under this chapter was developed to perform under conditions of low mass flow rates and operating pressures as high as 30 bar. The microgroove plates were made of Nickel while the other inner sub assembly plates were made out of Stainless steel. Owing to the high corrosion resistance and better thermal properties of nickel (as compared to stainless steel) this heat exchanger was develop to withstand corrosive fluids such as Ammonium hydroxide solution (in solution heat exchangers). The heat exchanger was developed using the NFFM, which was discussed in the previous chapter (CHAPTER 2:) A Teflon manifold with multiple passes, was used to provide where the fluid passing through the manifold is forced into the microgrooves.

Preliminary testing was carried out using single phase − water on both sides. Results indicate promising performance of close to 20,000W/m^{2}K. This is much higher than state of the art heat exchangers. In addition to the experimental results, a numerical validation was carried out to assess the experimental results. It was observed that there is close agreement between both the experimental and numerical results.

3.1 Design and Construction

The heat exchanger uses a series of plates which channel the flow of the fluid over the microgroove plates. There are four different types of plates which are used for the construction and working of the entire heat exchanger.

1) Microgroove Plate: This plate, made of nickel, has 40 micron grooves on both sides. The fin width is also 90 micron with an aspect ratio of 4. The Figure 3-2 and Figure 3-1 shows the microgroove plate being used and the surface of the plate. This plate will provide the main heat exchanging surface for the heat exchanger. Using NFFM, fluid will be pushed into the microgrooves, thus enabling higher contact of the fluid with surface.
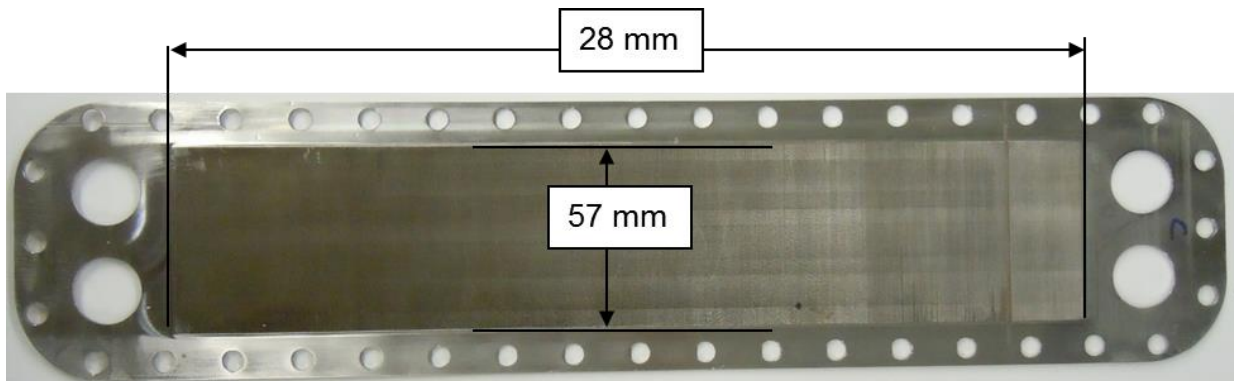
Figure 3-1: Microgroove Nickel plate
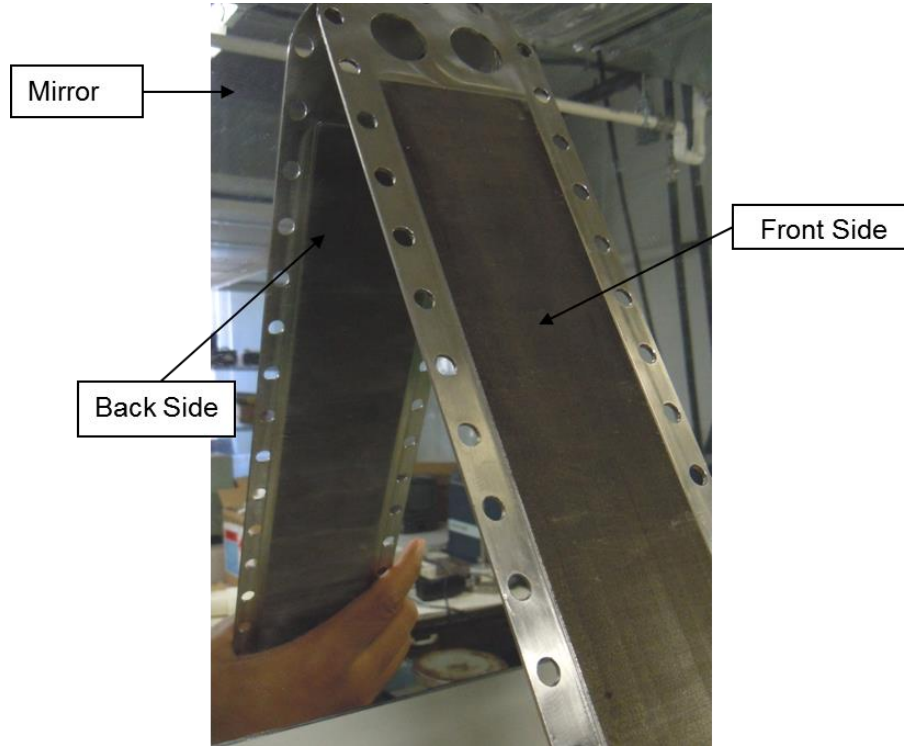
Figure 3-2: Microgroove plate surface

2) Manifold: One of the most important components of the plate heat exchanger
   is the manifold. This was essentially a 4.26 mm thick Teflon plate which was
   fabricated with minichannels grooved into it. The minichannels provided a feed
   mechanism of working liquid to the microchannels. There were two types of
   manifold which were considered for the assembly. For the end plates, the
   manifold had minichannels on one single side. The other side was left un-
   fabricated and was pressed against the shim plates thereby preventing any flow
   through the bare side. The second type of manifold which was used had mini-
   channels on both the sides. This manifold was to be used with the internal heat
   transfer plates when using a multi-plate arrangement. The geometry for both
   the type of manifolds are shown in

3) Figure 3-3 and Figure 3-4 below:

Figure 3-3: Internal manifold   **Figure 3-4: End plate manifold**

The other important aspect about the manifold was the baffles which were used to provide a multi-pass system for the manifold. These baffles were used to provide NFFM to the microchannels. The baffles were arranged in such a way that the manifold provided a 20-pass flow arrangement. The description of the NFFM in the manifold is shown in Figure 3-5 below:
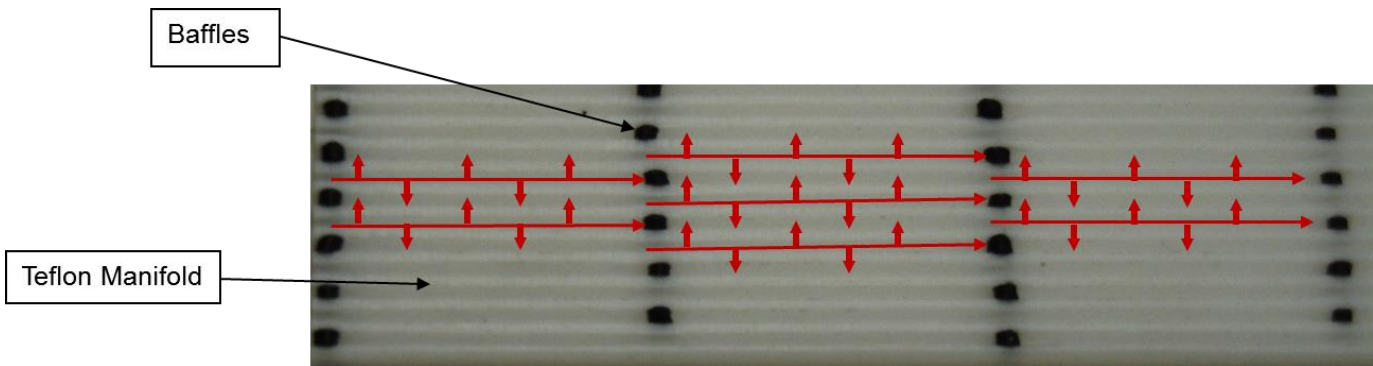
Figure 3-5: Flat plate heat exchanger manifold with flow description

The manifold therefore, forms a critical component of the heat exchanger, it is used to impart normal feed on the microgroove surfaces. The manifold contains multiple baffles as shown in the Figure 3-5 above where the flow through the manifold channels is restricted and is forced to enter the microgrooves of the nickel plate. The fluid which is forced into the microgroove plate then enters the adjacent manifold where it is again restricted by another baffle and is passed into the microgrooves.

37

4) Inner Plate: The Inner plate is made of 316 Stainless Steel. The inner plate houses the manifold, in the center. This plate is essential for directing the flow uniformly into the manifold to enable the NFFM. This inner plate also contains different O rings which provide a face seal against the adjacent micro-grove plate. The Figure 3-6 shows the complete Inner plate sub assembly, with the manifold and O rings.
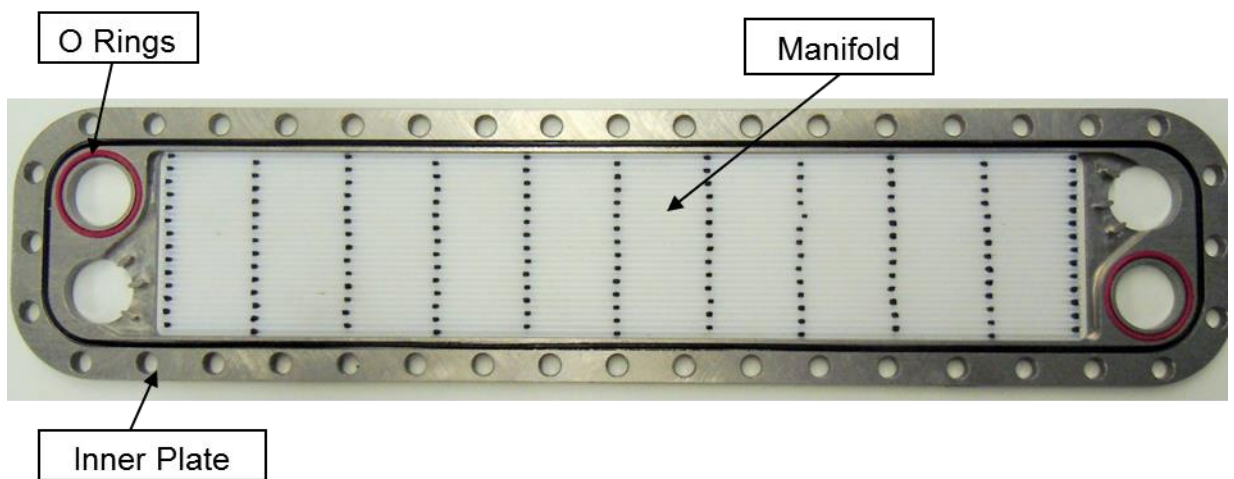
Figure 3-6: Inner Plate Sub Assembly

5) Shim Plate: This plate was a $^3/_{16}$" thick Stainless steel plate which is used to protect the covering – aluminum base plates from corrosion.

6) Base Plate: The base plate was a ½" thick aluminum (Grade 6061) plate which was placed at both the extreme ends of the heat exchanger. The entire system of inner plates and microgroove plates was sandwiched between the base plates as shown in Figure 3-7. One of the base plates was provided with internal threads, which were used for fastening of the entire heat exchanger using hex bolts. The base plate was designed to allow the heat exchanger to operate at

pressures of 30bar. Numerical simulation was done using ANSYS to observe the stress and deformation in the base plate when subjected to a pressure of 30bar. The results indicate a maximum nodal displacement of 0.01mm which was acceptable. The maximum stress within the base plate was also within tolerable limits (75 MPa) as shown in Figure 3-8.
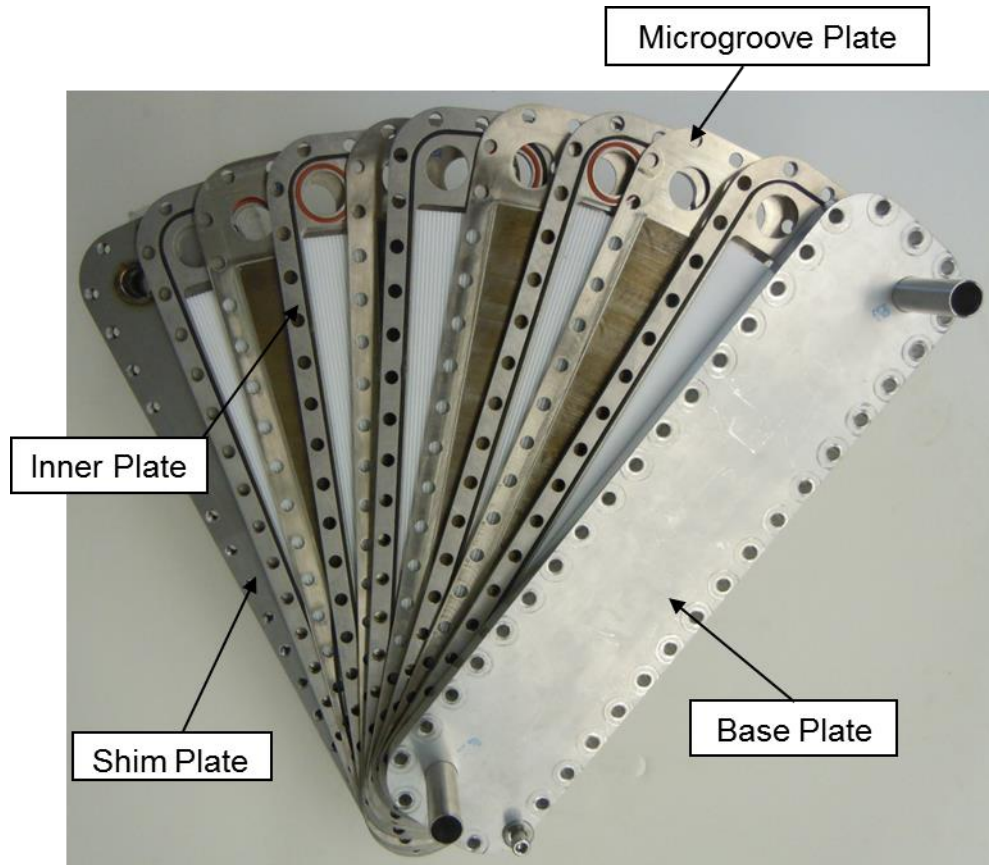
Figure 3-7: Assembly of the Solution Heat Exchanger
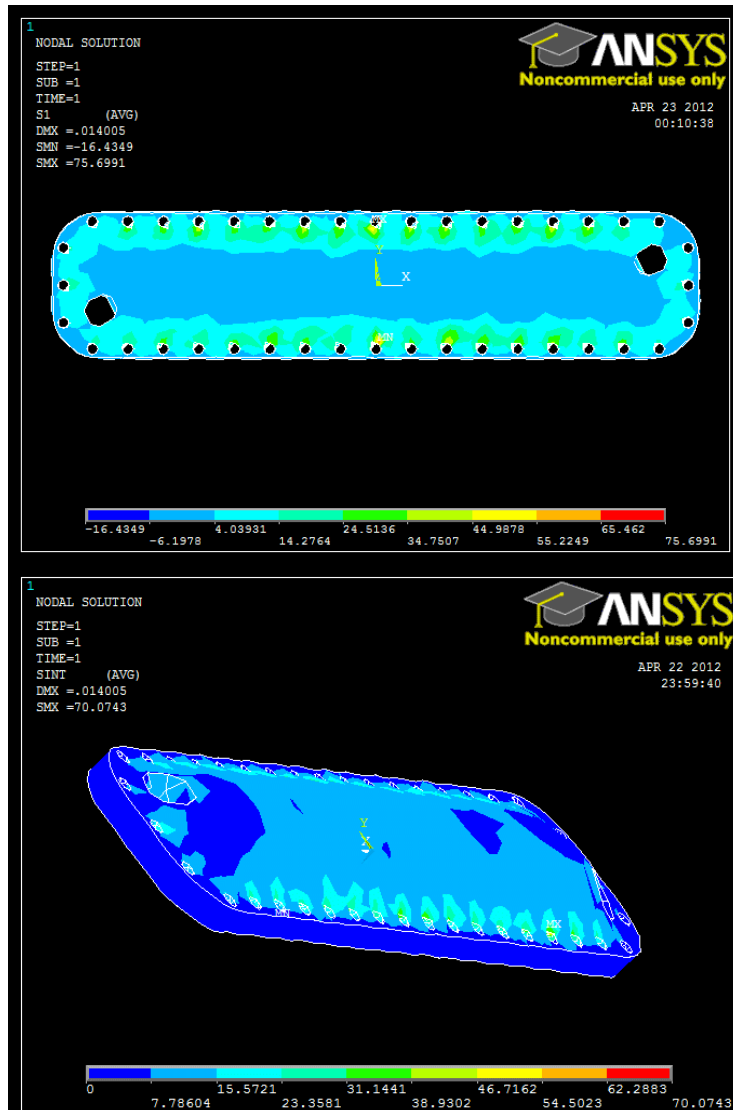
Figure 3-8: ANSYS Stress and Deformation Solution

The summary of all plate heat exchanger components' geometry can be found in Table 3-1 below:

Table 3-1: Geometrical specifications of Flat plate solution heat exchanger

Components	Material	Geometrical parameters
Microgroove Plate	Nickel (Thermal Conductivity –	Total Area:374x84 mm^2 Heat Transfer Base Area:280x57 mm^2 Fin height:360 μm

		Fin thickness:90 μm
	90.9 W/m-K at 25 °C)	Microchannel width:40 μm
		2 inlet and outlet cylindrical slots each: φ20 mm
		40 cylindrical holes for bolts : φ6.5 mm
		Heat Transfer base thickness: 1.76 mm
Manifold	Poly Tetra Fluro Ethene (Teflon) (Thermal conductivity – 0.25 W/m-K at 25 °C)	Double Sided Total Area:280x57 mm^2 Total thickness:3.76 mm Channel thickness:1 mm Fin thickness:1 mm Channel Height: 1.25 mm No. of the channels per side:28 Single Sided Total Area:280x57 mm^2 Total thickness:4.26 mm Channel thickness:1 mm Fin thickness:1 mm Channel Height: 1.25 mm No. of the channels per side:28
Inner Plate	Stainless Steel 316 (Thermal conductivity – 16 W/m-K at 25 °C)	Total Area:374x84 mm^2 Manifold slot Area:280x57 mm^2 Thickness: 3/16" Standard plate thickness 2 inlet and outlet cylindrical slots each: φ20 mm 40 cylindrical holes for bolts : φ6.5 mm
Shim Plate	Stainless Steel 316	Total Area:374x84 mm^2 Thickness: 1/32" Standard plate thickness

	(Thermal conductivity – 16 W/m-K at 25 ºC)	2, 5/8" SS 316 Tubes welded at the inlet and outlet ports 40 cylindrical holes for bolts : φ6.5 mm
Base Plate	Aluminum 6061 (Thermal Conductivity – 205W/m^{2}K at 25°C)	Total Area:374x84 mm^2 Thickness: ½" Standard Plate Thickness 40 cylindrical holes for bolts : φ6.5 mm
Volume of Heat Exchanger		0.004194 m^3
Heat Transfer Area		0.01596 m^2
Heat Transfer area to volume ratio		3.805 m^2/m^3

3.2 Assembly of Flat Plate Heat Exchanger

The flow of the fluid from the microgroove heat exchanger is a C-type path. Its inlet and outlet are on the same side. The fluid flows over the microgroove plates in counter flow configuration in the manner shown in the Figure 3-9 below.
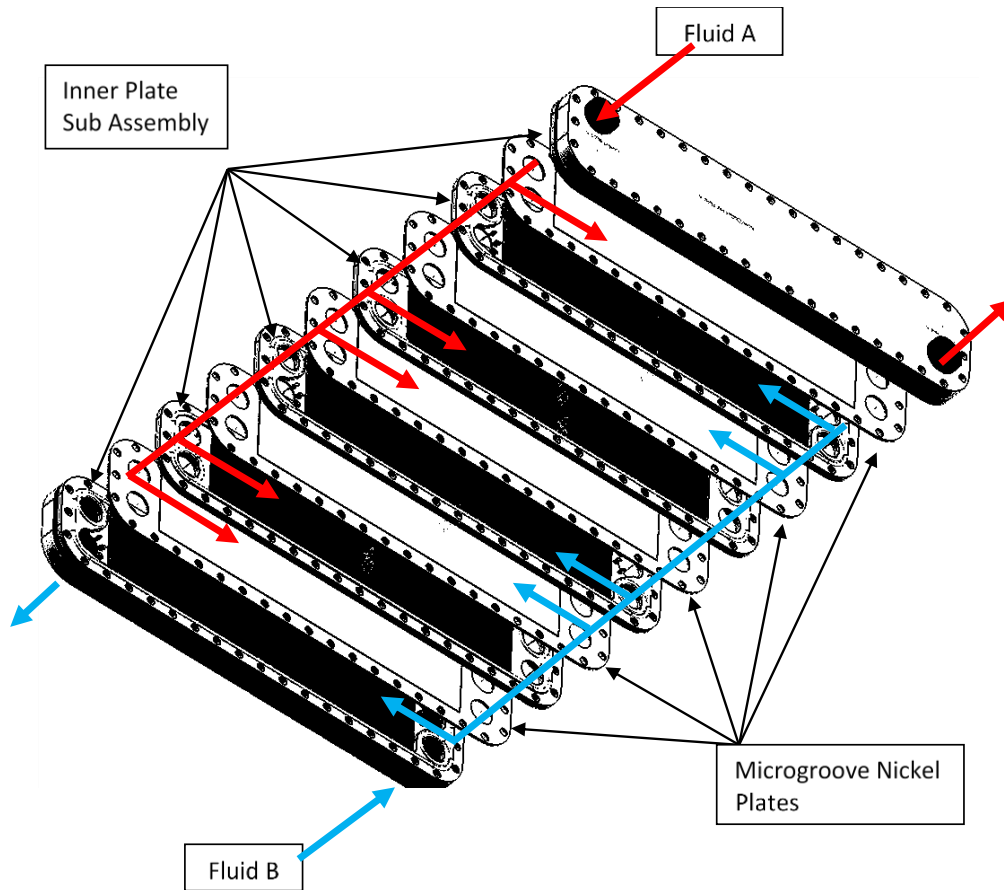
Figure 3-9: Flow configuration of Heat Exchanger

3.3 Experimental Single Phase Testing

In order to assess the capability of the heat exchanger in single phase flow, a single plate of the heat exchanger was tested with water as a fluid on both sides. The flow rate for both the sides was controlled such that the flow rate on both the sides would be the same for all test cases. The flow rate was measured by a rotameter and varied from 9 g/s to 20g/s. T – Type Thermo couples were used to measure the temperature at the inlet and outlet for both the fluids. Two chillers were used to provide cold and hot water to the heat exchanger. A single pressure transducer was used to obtain the pressure drop readings for one side of the heat exchanger. The other side of

the heat exchanger was assumed to have the same pressure drop due to same geometry on both the sides. The following diagram (Figure 3-10) shows the test loop which was used to obtain the heat transfer results:
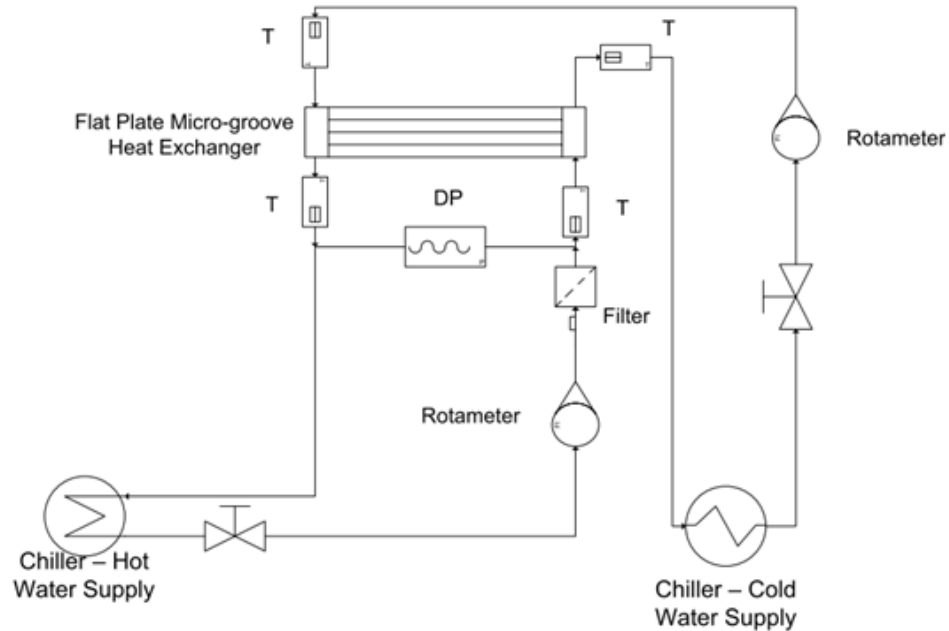
Figure 3-10: Flat Plate Heat Exchanger Experimental Test Loop

Temperature & pressure measurements and water flow rate is recorded through Agilent Datalogger and a GPIB interface with PC. Mass flow rate for water is recorded manually based on the rotameter reading. The test matrix consists of following parameter.

➢ Input

- Water flow rate (Cold and hot side)

- Water Inlet temperature (Cold and hot side)

➢ Output

- Water exit temperature (Cold and hot side)

- Pressure drop

The measurement is recorded once the system reaches steady state and flow rates are stable and constant. The input values are limited by transducer limits but the operating limit of the solution heat exchanger is well within the range and hence complete assessment can be done. The list of instruments used in the experimental setup and its brief details are given in the Table 3-2 below.

Table 3-2: List of instruments

Component Name	Manufacturer	Model	Operating Range	Accuracy
Cold Water Side Chiller	NESLAB	M75	-15 ºC to +35 ºC	± 0.15 ºC
Hot Water Side Chiller	Neslab	HX150	+5 ºC to +35 ºC	± 0.1 ºC
Rota meter	Omega	FL 1502A	0.145-1.45GPM	± 2 %
Thermocouples	Omega	T-type	-200 ºC to +350 ºC	± 0.3 %
Pressure Transducers	Validyne	P55D	0 -12 PSI	± 0.25 % FS
Data Acquisition system	Agilent	34970A	20 analog input channels	NA

The raw data then obtained through the Data acquisition system was parsed through Microsoft Excel in order to obtain meaningful results and thermal performance calculations.

3.4 Governing Equations

Ideally, the energy balance for the heat exchanger should be maintained. However, due to internal friction, measurement and instrumentation errors and other energy losses, there is a slight difference between the heat transfer by both the sides. The heat transfer for one side of the heat exchanger can be calculated as:

$$Q_{hot} = \dot{m} * Cp * \left(T_{hot_{in}} - T_{hot_{out}}\right) \qquad \text{Eq. 7}$$

$$Q_{cold} = \dot{m} * Cp * \left(T_{cold_{out}} - T_{cold_{in}}\right) \qquad \text{Eq. 8}$$

$$Q_{diff} = \left(1 - \left(\frac{Q_{cold}}{Q_{hot}}\right)\right) * 100\ \% \qquad \text{Eq. 9}$$

The LMTD for counter flow configuration can be calculated from the measured values as follows:

$$LMTD = \frac{\left(\left(T_{hot_{in}} - T_{cold_{out}}\right) - \left(T_{hot_{out}} - T_{cold_{in}}\right)\right)}{Ln\left(\frac{\left(T_{hot_{in}} - T_{cold_{out}}\right)}{\left(T_{hot_{out}} - T_{cold_{in}}\right)}\right)} \qquad \text{Eq. 10}$$

For calculating the overall heat transfer coefficient we use the following equations:

$$Q_{mean} = \frac{Q_{hot} + Q_{cold}}{2} \qquad \text{Eq. 11}$$

$$A_{surface} = (280 * 57) * 10^{-6} [m^2] \qquad \text{Eq. 12}$$

$$U = \frac{Q_{mean}}{A_{surface} * LMTD} \qquad \text{Eq. 13}$$

The flat plate heat exchanger was tested with horizontal orientation. The geometry and the flow on both sides was the same. Using this knowledge, a safe assumption was made that the pressure drop and the heat transfer coefficient was the same on both the sides.

$$\left(\frac{1}{U}\right) = \left(\frac{1}{h_{hot}}\right) + \left(\frac{1}{h_{cold}}\right) + \left(\frac{t_{base}}{k_{nickel}}\right) \qquad \text{Eq. 14}$$

$$h_{cold} = h_{hot} = h \qquad \text{Eq.15}$$

$$\left(\frac{2}{h}\right) = \left(\frac{1}{U}\right) - \left(\frac{t_{base}}{k_{nickel}}\right) \qquad \text{Eq. 16}$$

The pressure drop for the heat exchanger can be directly read by the data acquisition unit and would require no governing equations for further calculations.

3.5 Experimental Results

The test results obtained indicates superior performance of the NFFM applied to low heat flux applications. An overall heat transfer coefficient of close to 20 kW/m²K was obtained at flow rates as low as 20g/s. The advantage of using NFFM is clearly visible in this case. As the fluid enters the microchannel through the manifold channel, the change in area of flow causes the fluid to enter a developing region, thereby

increasing the heat transfer coefficient for this region. This effect can also be attributed to the superior thermal performance of NFFM.

Additionally, as the flow increases, the velocity through the microchannel increases which increases the heat transfer coefficient. The plot in Figure 3-11 below shows the variation of overall heat transfer coefficient against the water flow rate.
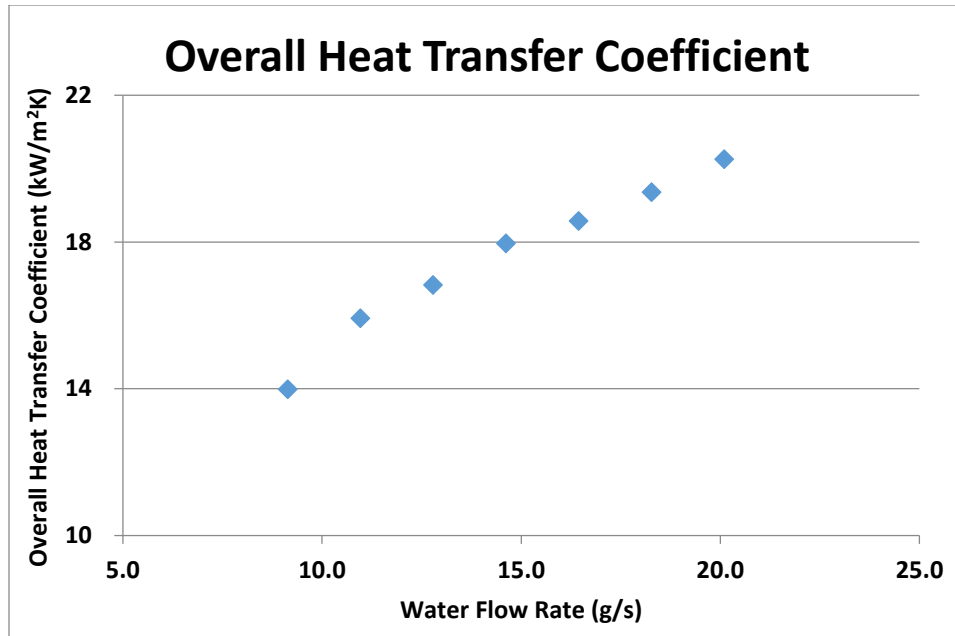
Figure 3-11: Variation of overall heat transfer coefficient with water flow rate

The variation of average heat transfer coefficient with increasing flow rate is as given in the Figure 3-12 below:
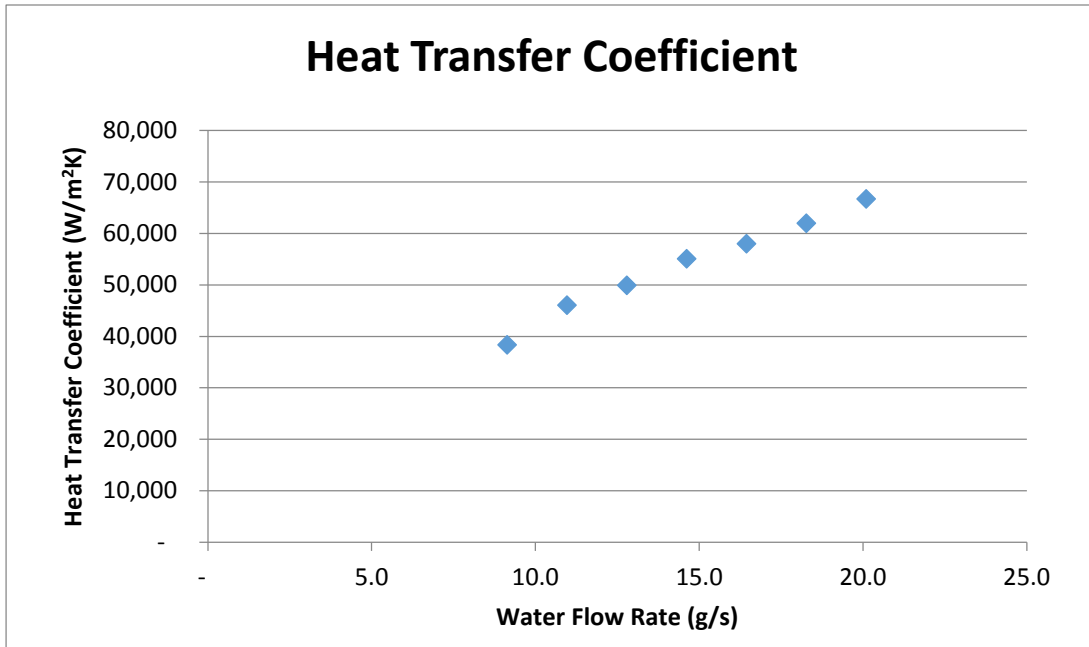
Figure 3-12: Variation of Heat transfer coefficient with water flow rate

The geometry and the flow rates being same on both the sides, the heat transfer coefficient was considered equal on both the sides. Figure 3-13 below shows the variation of heat transfer versus the pressure drop. This is also indicative of the overall performance of the microchannel plate. The comparison between pressure drop and heat transfer coefficient of the experimental and numerical simulation will be explained in the "Numerical Validation" section.
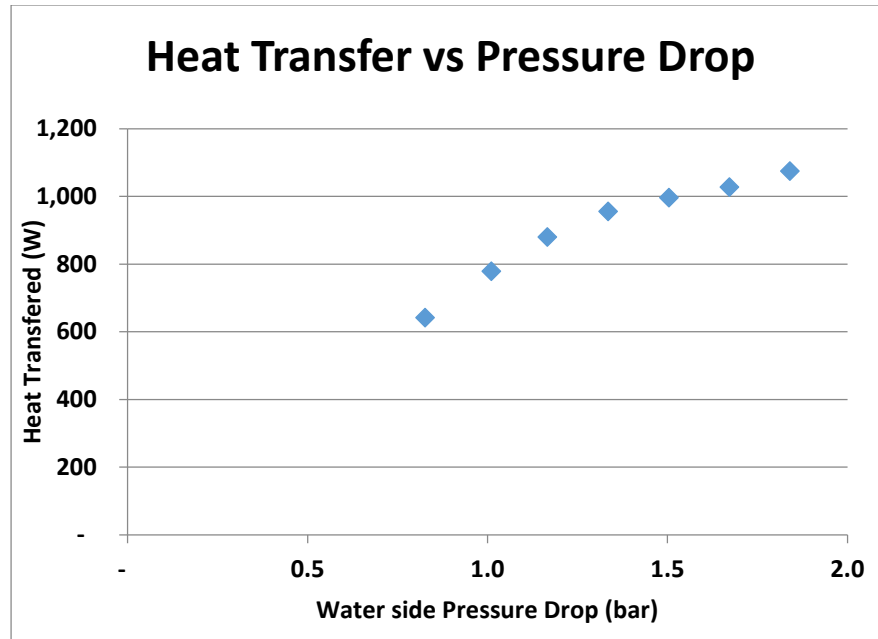
Figure 3-13: Variation of heat transfer capacity with pressure drop

The above results show the total capacity of the heat transfer capacity was found to be around 1 kW. Based on these results, for a total capacity of 11kW, the number of plates required would be around 12. This would lead to an increase in the overall size of the heat exchanger. The difference in the heat transfer between both the sides was observed to be less than 5% at all times. The LMTD variation with water flow rate is shown in Figure 3-14 below:
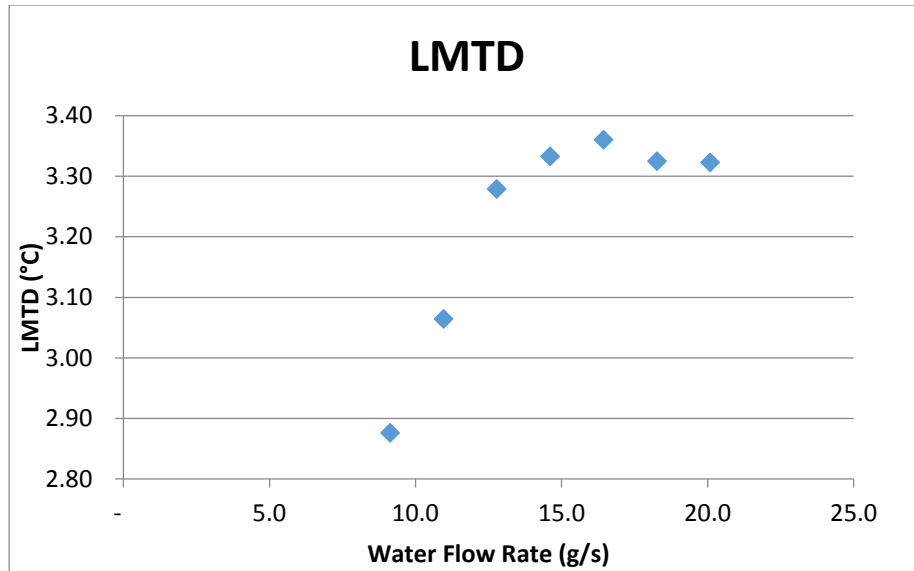
Figure 3-14: Variation of LMTD with water flow rate

All the results shown above show the performance of microchannel flat plate solution heat exchanger, tested in the lab using water on both sides. The average uncertainty for the experimental investigation was calculated using inbuilt EES functions. The average uncertainty for heat transfer, heat transfer coefficient and overall heat transfer coefficient was found to be approximately 5.3%, 24.4% and 16.4%.

3.6   Numerical Validation

In order to support the findings made through the experimental testing, a numerical validation would prove to be very useful. An agreement between these values would also indicate the accuracy of experimental results obtained. In addition, for future testing of the heat exchanger performance, a full scale lab testing may not be

necessary. The results from the simulations can be obtained to assess the performance of the heat exchanger at different conditions.

The results obtained through experimental testing were validated by a numerical model using ANSYS Fluent. Based on the chiller flow rates with which the heat exchanger was tested, the actual flow rate in a single microchannel was calculated. A constant heat flux boundary condition was considered at the base of the microchannel. This heat flux was calculated based on the total heat transferred in the heat exchanger divided by the base area. The variation in heat transfer coefficient and pressure drop with the inlet temperature of working fluid is very small. The only change which may be observed would be due to the slight variation of fluid properties. The temperature of the inlet fluid for the numerical study was assumed to be 300 K for all cases.

The flow rate of water through the microchannels was calculated based on the number of open manifold channels and the number of microchannels per pass. Out of the total 28 channels, only half of the channels are open to the inlet fluid (the others being block by the baffles). Based on the dimensions of the total number microchannels fabricated on the plate are approximately 2153. Therefore, every manifold pass supplies water to 107 microchannels. Furthermore, the water supplied by each manifold channel divides into two streams which go in opposite directions through the microchannels. The Figure 3-15 below provides a pictorial explanation of the flow through each microchannel.
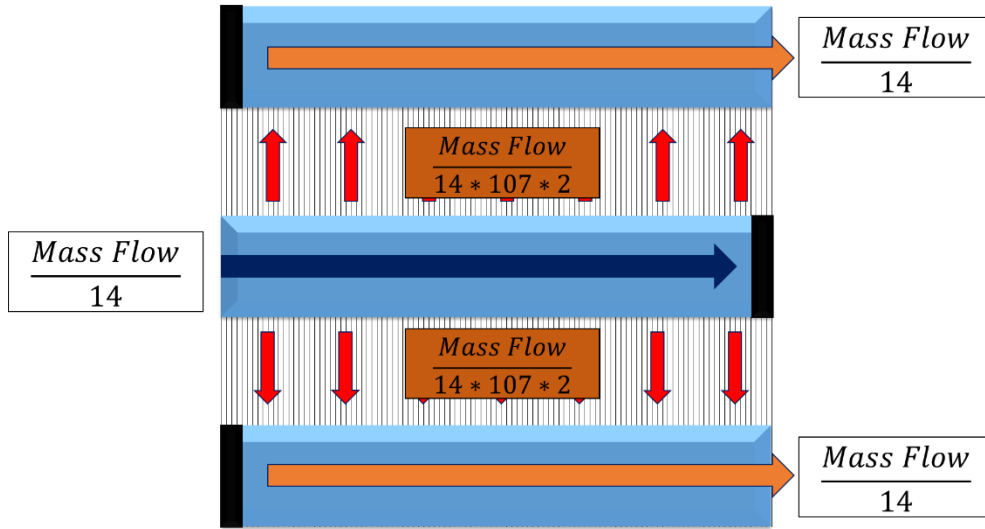
Figure 3-15: Branching of flow through manifold microchannel assembly

Therefore, for each experimental test point, the flow rate through the microchannels was calculated as the total flow rate divided by 2996.

$$\dot{m}_{channel} = \frac{\dot{m}_{chiller}}{14 * 107 * 2}$$

Eq. 17

Using the microchannel geometry provided in the, Table 3-1 a single channel model was created and meshed in gambit. The model consisted of inlet and outlet zones of the manifold section, two microchannel fin walls and a base. Each fin had a thickness of half of that of the actual microchannel wall. Moreover, the fin was coupled to the base to conduct heat flux from base to fins and by convection to water. Base thickness was calculated based on total thickness of microchannel plate divided by 2. Heat flux was provided from the bottom of the base. Heat entering the base would conduct through the base. In doing so, conduction through the base would also contribute to the thermal resistance. The schematic diagram in the Figure 3-16 below would help in understanding different parts of microchannel model.

53
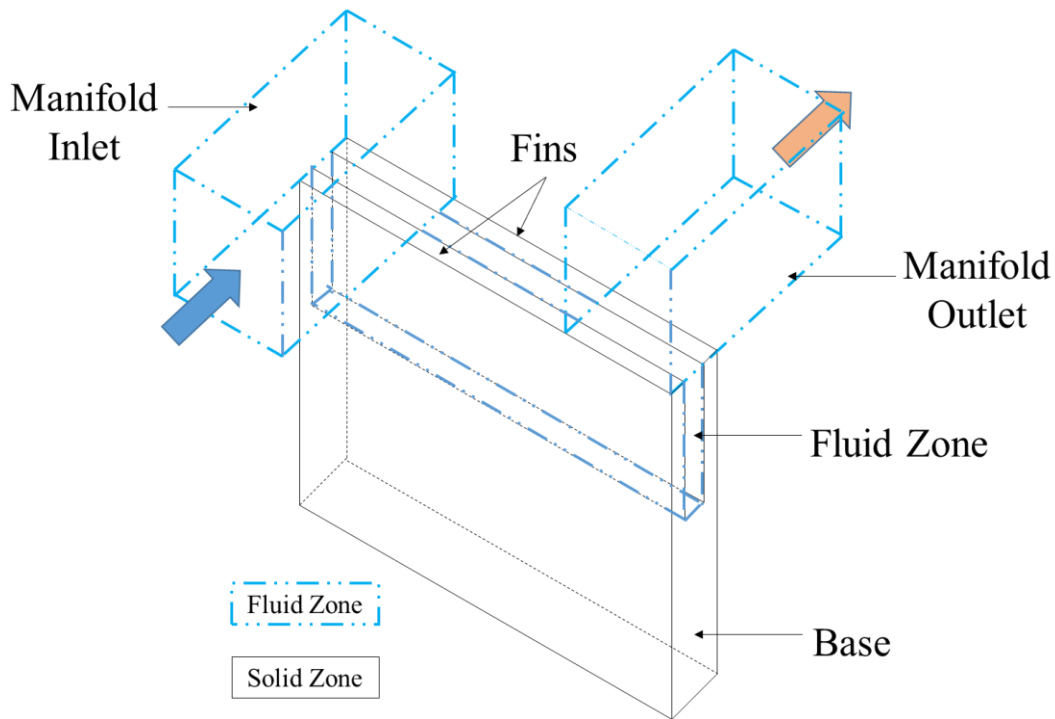
Figure 3-16: Numerical model for manifold microchannel CFD simulation

The numerical model accounted for the pressure drop due to the 90° bend in the flow from the inlet manifold to the microchannel and from the microchannel to the outlet manifold. The flow thus travels from the manifold and impinges normal to the microchannel base. This impingement creates a stagnation zone where the velocity of the flow reaches 0. The base material was Nickel which was chosen from the fluent database of materials. The working fluid was water. As the flow enters the microchannel as shown in the Figure 3-16 above, it encounters a 90° bend into the microchannel. This is accompanied by a significant reduction in area from 0.625 mm^2 to 0.02 mm^2 which amounts to a reduction of approximately 96.8%. This reduction in area results in significant pressure drop. However, what this reduction in flow area also does is increase the local velocity of the fluid which enters the microchannel.

Additionally, it induces the fluid into a developing flow region. These two contributing factors are responsible for the increase in the heat transfer coefficient in the microchannels. As the fluid enters the microchannel, its local velocity increases as it moves through the microchannel. The outlet of this fluid is characterized by two more 90° bends which allow the fluid to be removed from the microchannel to the outlet manifold. Another effect which may also potentially contribute to the enhanced heat transfer is the centripetal momentum that the fluid experiences as it bends twice. This centripetal momentum allows the fluid closer to the base of the microchannel to have a greater velocity which would further enhance the local heat transfer coefficient. All the effects mentioned earlier can be seen in the simulation results obtained through numerical modeling.
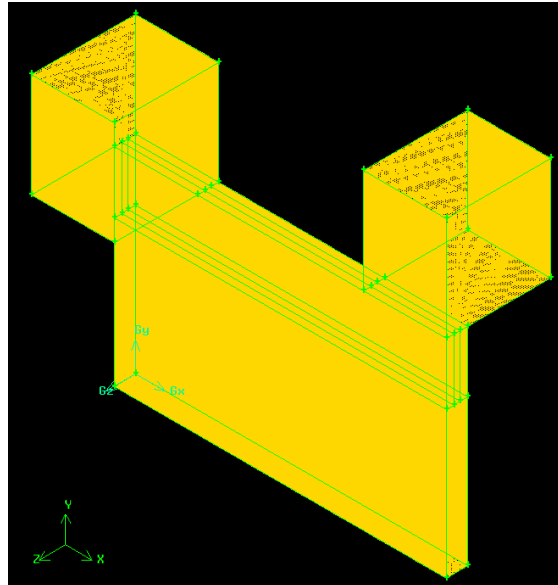
Figure 3-17: Meshed model for numerical simulation using ANSYS Fluent

In order to obtain a converged solution, a grid independence study was conducted for obtaining grid independence of the pressure drop and the heat transfer

values. Hexagonal meshes were generated using Gambit which had nodes ranging from 750,000 to 2,900,000. The Figure 3-18 below depicts the grid independence for the value obtained through simulations.
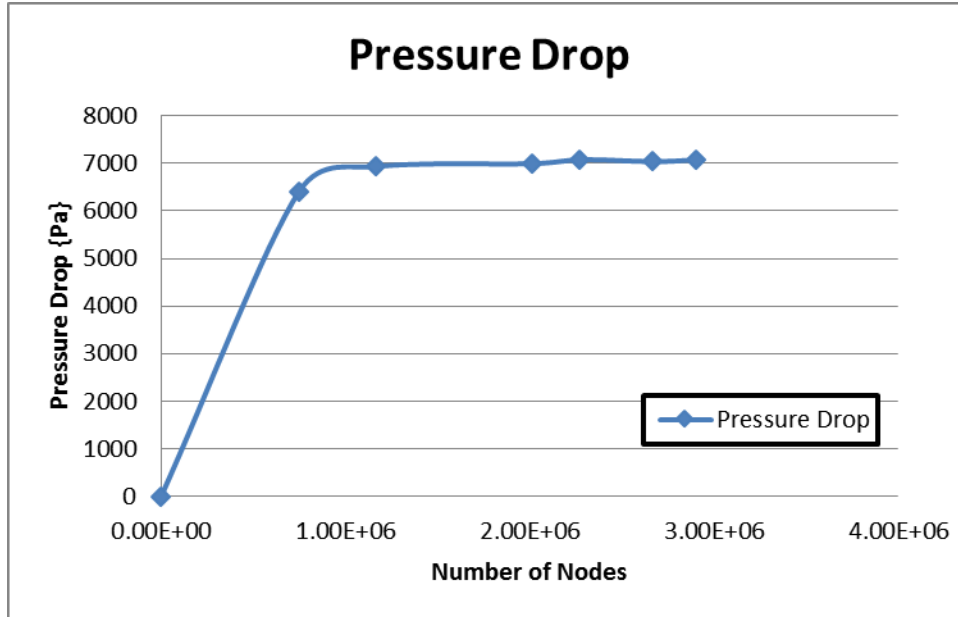
Figure 3-18: Grid independence of numerical model

A similar grid independence was carried out to check the convergence of the heat transfer performance. Simulations were run for a mesh having 2,274,000 and 2,016,400 nodes. The results for water outlet temperature and base temperature both these cases were found to be within 1%. This indicated that simulation results obtained for the mesh having 2,274,000 nodes was independent of the grid. This mesh was used to run all the simulation results for different operating conditions. The Table 3-3 below shows the test matrix which was used to run all the simulations.

Table 3-3: Numerical testing matrix

Test Number	Mass flow in Microchannels [kg/s]	Heat Flux [W/m^2]
1	3.03E-06	40,210.33

2	3.64E-06	48,795.13
3	4.24E-06	55,165.80
4	4.85E-06	59,859.57
5	5.45E-06	62,407.14
6	6.06E-06	64,383.90
7	6.66E-06	67,316.46

In order to capture the nature of the flow, three properties were chosen namely, Pressure, Temperature and Velocity. Contour plots were developed for all the test points for these properties. The Table 3-4 and Table 3-5 below shows the results obtained through numerical modeling.

Table 3-4: Contour plots for Pressure, Temperature and Velocity for Test number 2

Temperature Gradient		
Velocity Profile		
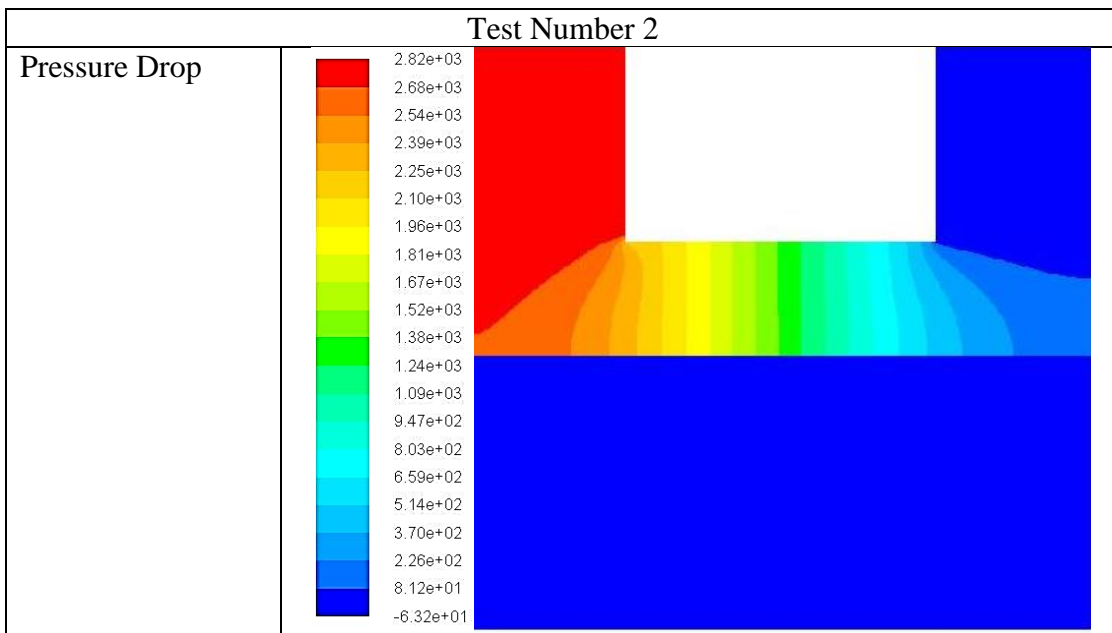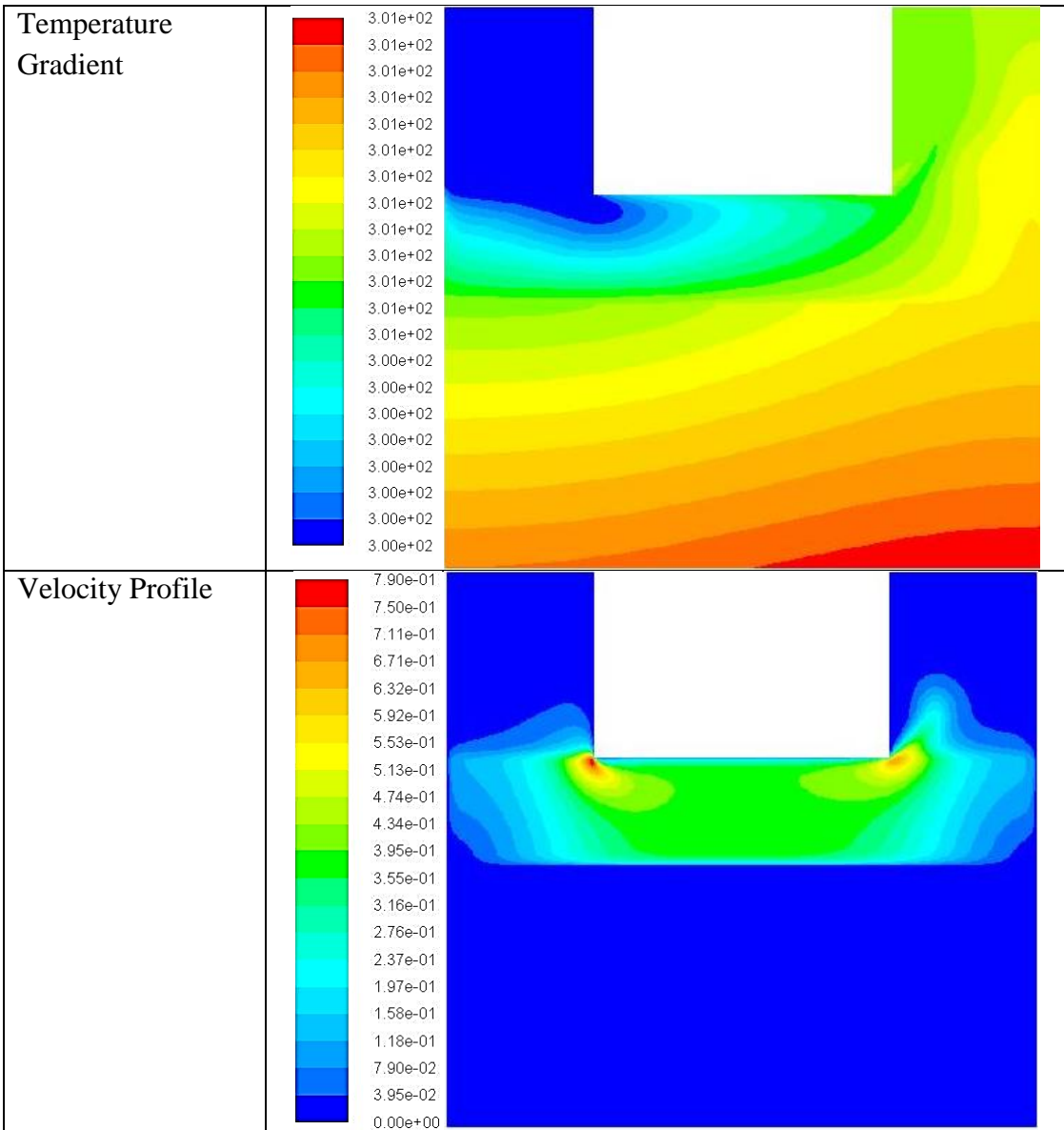
Table 3-5: Contour plots for Pressure Temperature and Velocity for Test number 7

Test Number 7	
Pressure Drop	
Temperature Gradient	

Velocity Profile	
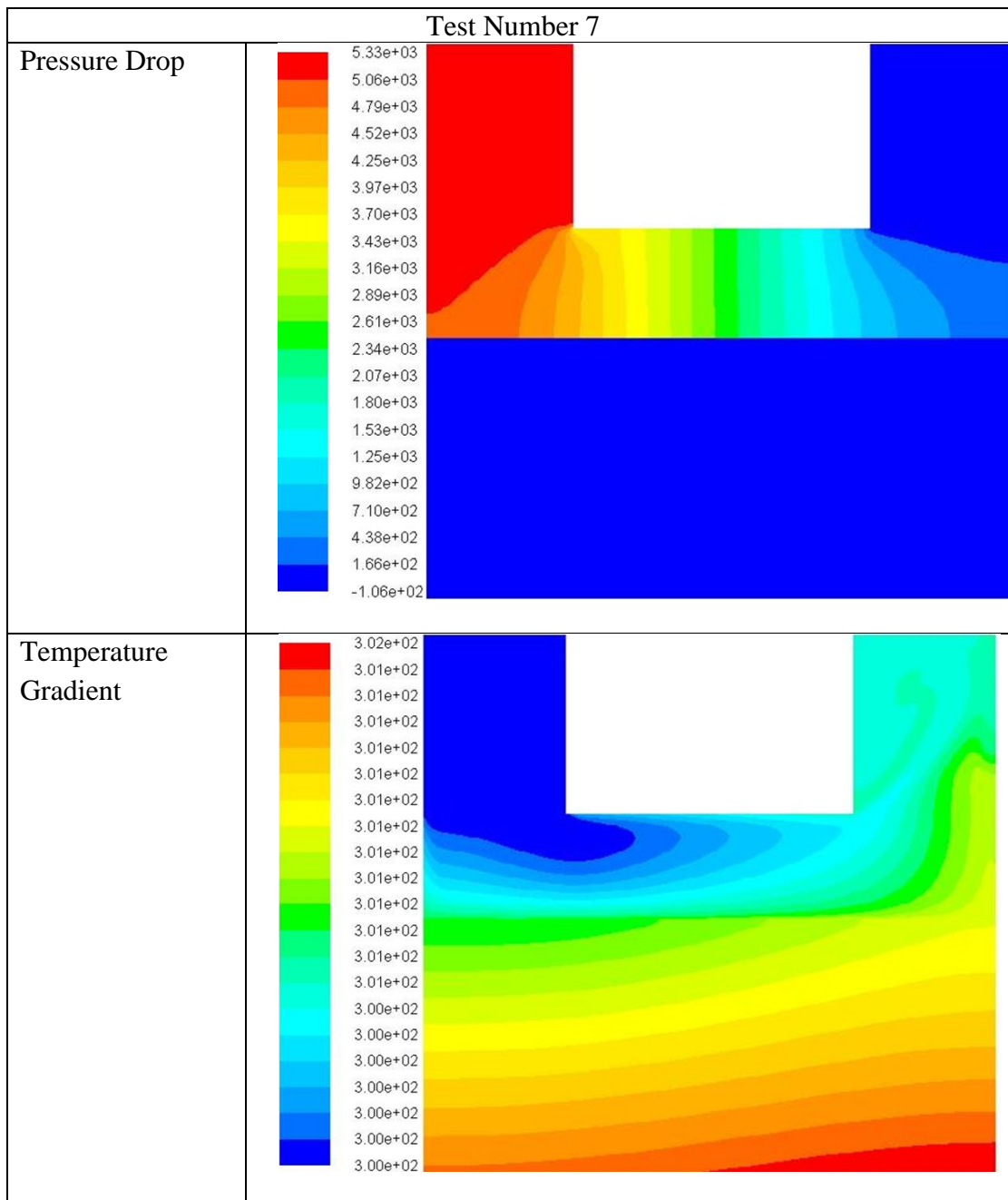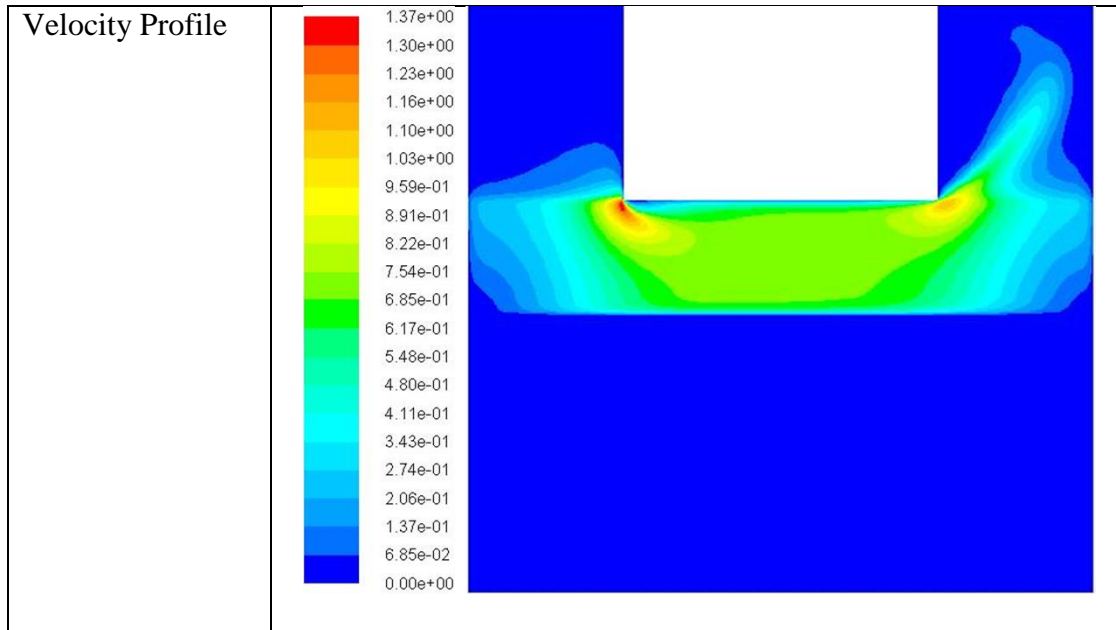
The results obtained by considering area weighted average of different properties was plotted against the experimental values obtained. The results indicate a close agreement between both the findings. The experimental results for pressure drop are higher than numerical predictions. This is expected because the pressure drop measurement ports are located outside the heat exchanger. The numerical results do not take into account the pressure drop from the supply tubes to the heat exchanger and from the constriction in area as the flow goes from supply tube to the manifold. The numerical predictions only take into account the pressure drop in the manifold and the microchannels. Therefore, there is a higher difference between the pressure drop results. The heat transfer coefficient on the other hand compares very well with the experimental findings. The graphs (Figure 3-19) below indicate the comparison of the experimental and the numerical results.
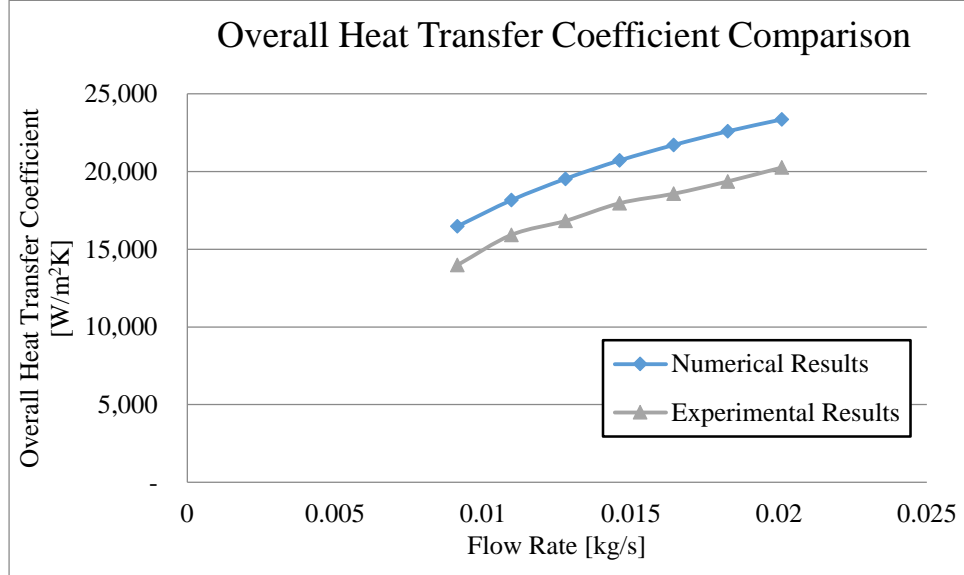
Figure 3-19: Comparison of numerical and experimental results for overall heat transfer coefficient

The Numerical predictions provide information about the fin and the base heat transfer coefficient. The base heat transfer coefficient is calculated considering the heat flux through the fins and the average wall temperature. The base heat transfer coefficient is calculated considering the base average temperature and the heat flux through the base.

$$h_{base_{avg}} = \frac{Q_{flux_{base}}}{T_{base_{avg}} - T_{in}}$$ **Eq. 18**

$$h_{fin_{avg}} = \frac{Q_{flux_{fin}}}{T_{fin_{avg}} - T_{in}}$$ **Eq. 19**

As per the results, the fin heat transfer coefficient is lower than the base heat transfer coefficient. This is mainly because of the larger area associated with the fin wall. This reduces the heat flux transferred from the wall. However, the total heat transferred from the wall constitutes almost 70 % of the total heat transferred to the fluid. Therefore, the in walls create a tangible impact on the performance of the heat exchanger. The comparison of the results for the pressure drop are highlighted in Figure 3-20 below:
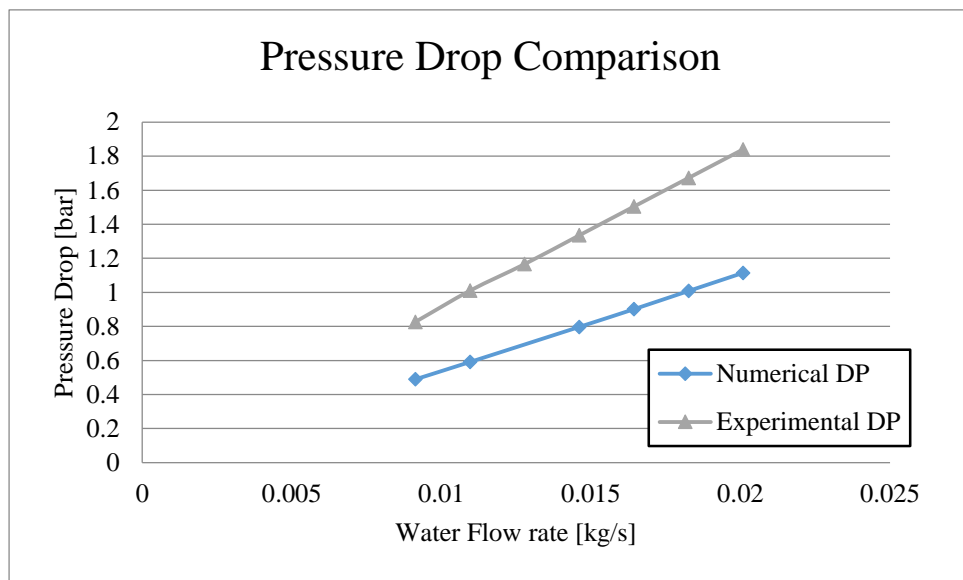
Figure 3-20: Comparison of numerical and experimental results for pressure drop

CHAPTER 4:   COUNTER FLOW TUBULAR MICROCHANNEL HEAT EXCHANGER (WITH 3D PRINTED MANIFOLD)

Fabrication of microchannels using microdeformation technology is new and equipment has to be mature to get competitive on the market. However similar microgroove geometry is currently manufactured on the high performances heat transfer tubes as for example Wolverine Turbo C-III. In this chapter we will explore utilization of those commercially available structures for fractal microchannel heat exchanger.

4.1   Design of Tubular Microchannel Heat Exchanger

The tubular heat exchanger was developed using the following components:

1. Heat Transfer Tube: The heat transfer tube which is also the microchannel tube was designed and fabricated by Wolverine Inc. The material used was plain carbon steel. The tube was a conventional ¾" plain carbon steel tube having microgrooves outside and a rifling structure inside. The rifling structure provided circumferential direction component to the velocity which increased the local Reynolds number near the surface. This increased the Nusselt number thereby improving thermal performance. The microstructures on the outer surface improved the wetting capabilities of the tube. This enabled higher heat flux to be transferred from the tube. The example of the tube can be seen in

Figure 4-1 while the detailed dimensions of this tube have been provided in the Table 4-1.
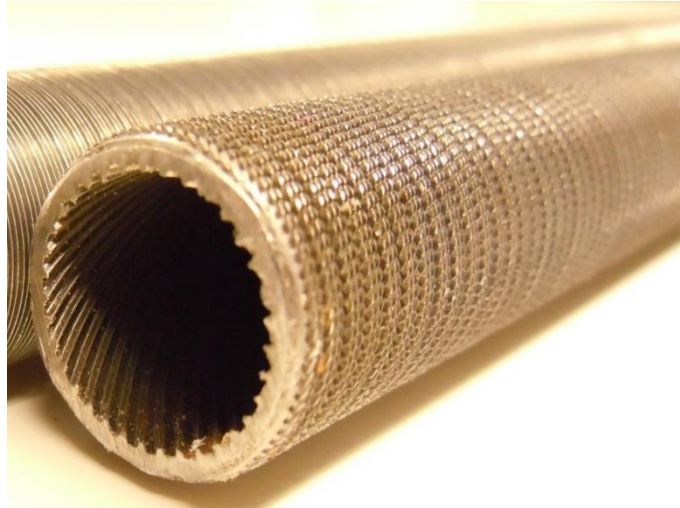
Figure 4-1: Plain carbon steel microchannel tube – Wolverine Turbo C III

2. Manifold: One of the most challenging tasks of development of the Normal flow feed mechanism for a tubular heat exchanger was the manifold. In order to develop a tubular heat exchanger, a new manifold design having a T-shaped cross-section was conceptualized. A preliminary design of the manifold was developed in PRO E. Many different fabrication techniques were surveyed for the fabrication however, most of these techniques were incapable of handling such complex and delicate work. Such complex geometries require more intricate fabrication processes. Sheet metal works with laser cutting was also surmised, but due to high cost, the process was disqualified.

3D printing is one of the novel techniques which has come up in recent times and is making significant strides in fabricating complex designs for

various applications. The Mechanical Engineering machine shop houses a 3D printing machine which uses ABS plastic – Acrylonitrile Butadiene Styrene to make complex geometries and shapes. This process was successfully used to develop the manifold for the tubular heat exchanger. Figure 4-2 shows the prototype manifold which was developed by 3D printing technology.
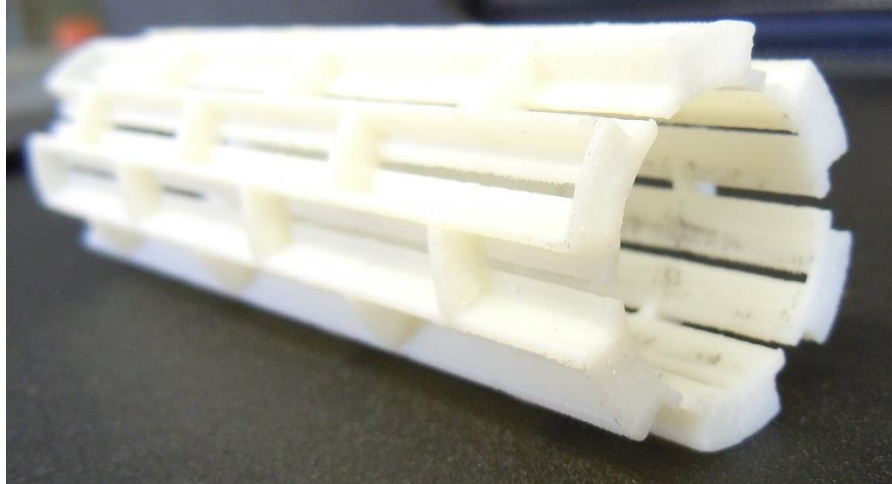
Figure 4-2: 3D Printed manifold

The 3D printer used by the machine shop is a Dimension SST 1200es, which uses CAD design drawings in STL format as an input to print complex geometries by additively depositing ABS plastic. The machine consists of a deposition mechanism which is supported in order to provide 6 degrees of freedom. The material depositor has 4 degrees of freedom on the horizontal plane ($\pm$x and $\pm$y axis) and the plate carrying the item which is being made has two degrees of freedom in the vertical direction ($\pm$z axis). In order to make complex geometries which contain hollow sections, the 3D printer uses a filler material in order to fill any gaps or voids. The printing takes place at temperatures which are higher than the melting point of the raw material – ABS

plastic, therefore, the raw material needs to be deposited on a support material in order to prevent it from collapsing owing to its semi-molten state. This is where the filler material is useful. The filler material is essentially made from animal fats which are not miscible with the ABS plastic. Once the printing is complete, the filler material can be easily separated from the raw material by immersing the entire component in hydroxide base soap solution. The filler material dissolves in this solution, leaving behind the required part. Figure 4-3 shown an example of 3-D printing in operation.

Support carriage for depositor

Depositor
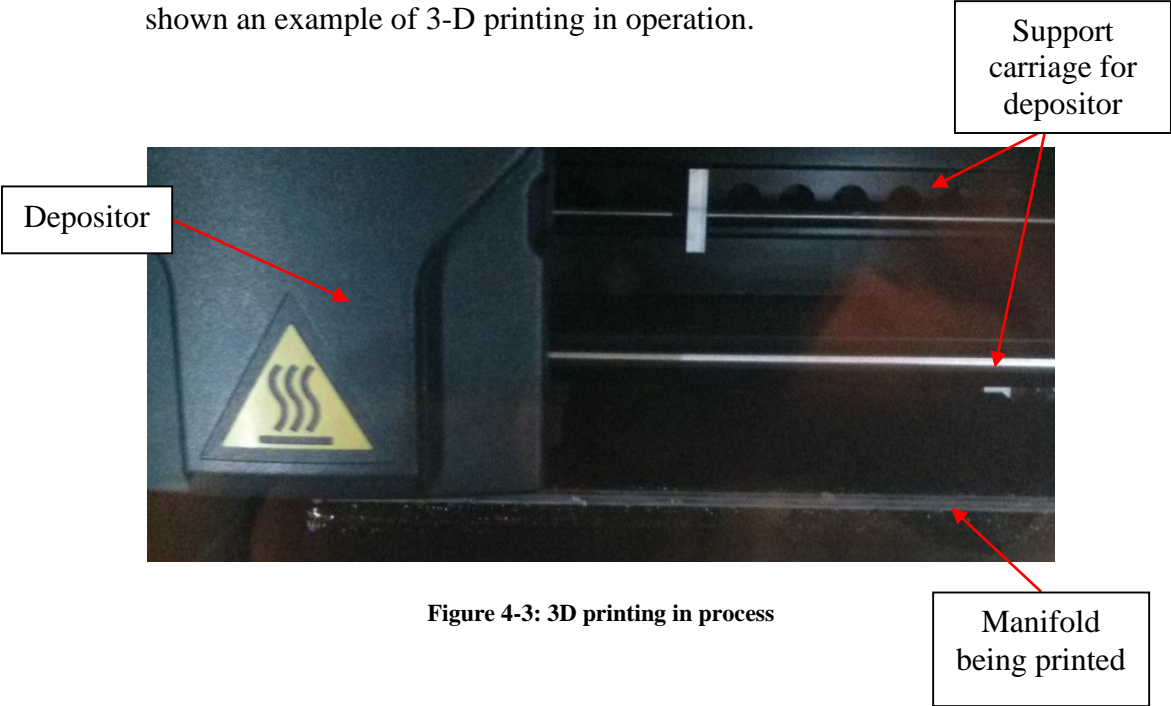
Figure 4-3: 3D printing in process

Manifold being printed

Once the printing is complete, the raw manifold block is obtained. Figure 4-4 below is a picture of the manifold with the filler material after the printing job is completed:

Figure 4-4: 3D printed manifold after printing is complete

3. Outer Tube: A Stainless Steel (Grade 316) standard tube was used for the outer tube of the heat exchanger. The tube dimensions are provided in the geometry Table 4-1 below. The tube was selected based on the minimum possible thickness which can be used to operate at 30bar pressure.

4. Connection ports: Swagelok fittings were used as connection ports for the heat exchanger. Cross-section drawing for the Swagelok fittings is shown in the Figure 4-5 below. A ¾" to 1" tube connecting joint was used to make the connection ports. The central threaded flanges were drilled and welded with a 3/8" male threaded connection port which provided flow for the fluid for the outer surface.
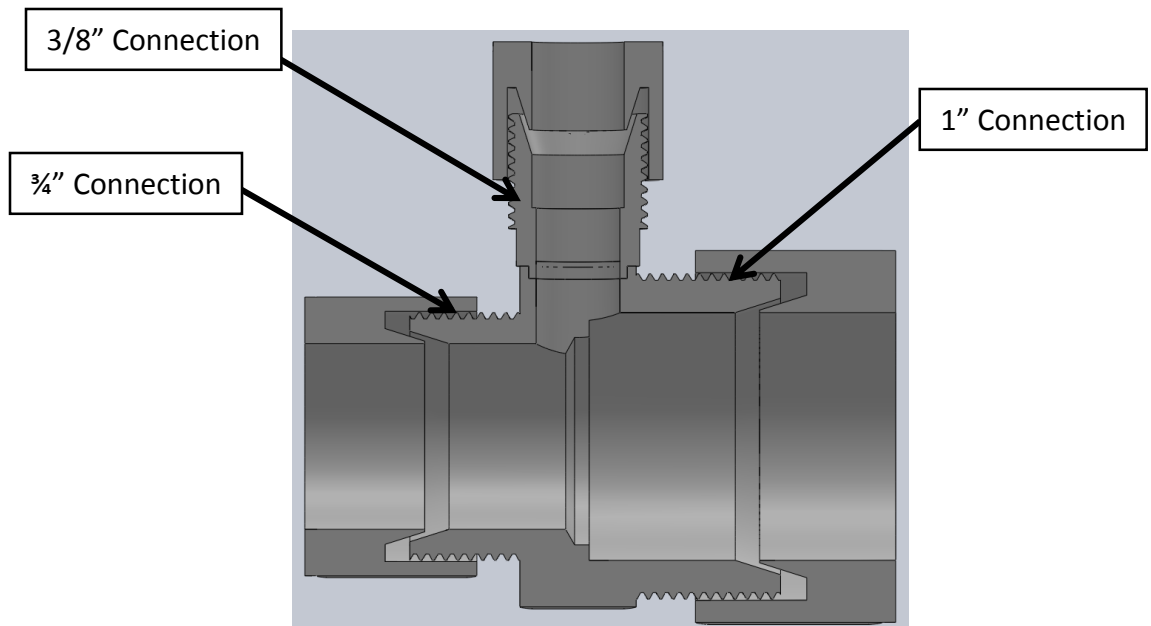
Figure 4-5: Connections

The ¾" connection port was used to provide flow to the inside of the main heat transfer tube. In order to aid interchangeability of tubes if required in order to test different surfaces, Teflon ferrules were used to provide leak proof connection. The ¾" inch heat transfer tube has to pass through the entire Swagelok connection, to enable this, the Swagelok fitting was drilled using a ¾" drill bit.
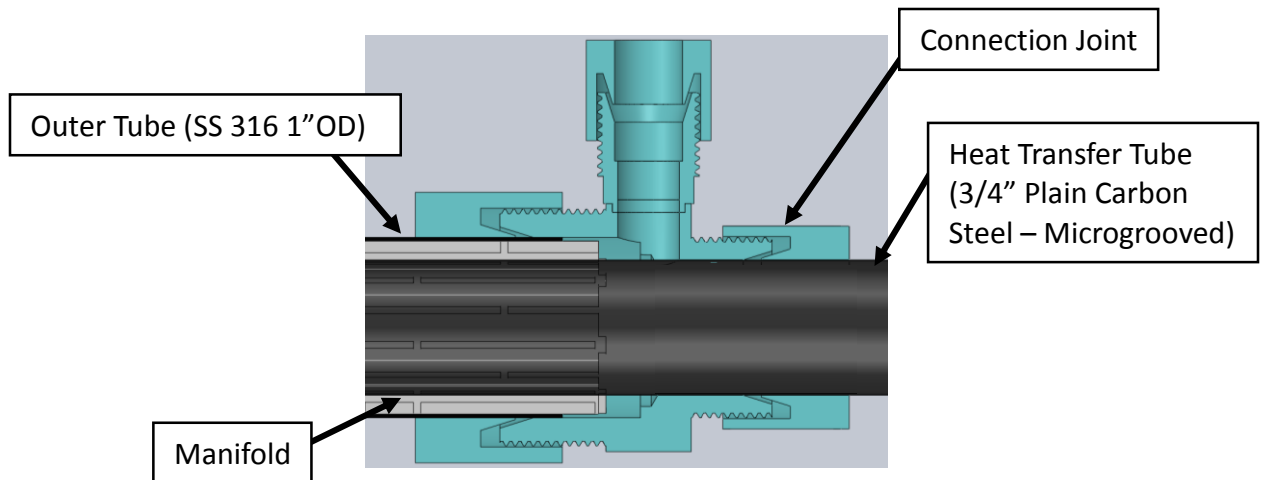
Figure 4-6: Assembly of connections

The Table 4-1 below summarizes the geometrical specifications of the

solution heat exchanger:

Table 4-1: Geometrical Specifications of the actual tubular microchannel heat exchanger

Components	Material	Geometrical parameters
Microgroove Tube	Plain Carbon Steel (Thermal Conductivity – 43 W/m-K at 25 °C)	OD: 18.8 mm ID: 16.2 Minimum wall under fins: 0.6 mm Fins per inch : 43 Wall thickness: 1 mm Length: 914 mm
Manifold	Acrylonitrile Butadiene Styrene (ABS) (Thermal conductivity – 0.17 W/m-K at 23 °C)	ID: 18.8 mm OD:24.4 mm Wall thickness: 1 mm

69

		Manifold channel width: 1 mm
		Pass Length: 25.4 mm
		Length: 4 manifolds, 228.6 mm each (Total 3 ft)
Outer Tube	Stainless Steel (Type 316) (Thermal conductivity – 16 W/m-K at 25 ºC)	ID: 24.4 mm OD:25.4 mm Length: 914 mm

Using the above mentioned components, the solution heat exchanger can be easily assembled and tested. However, in order to assemble the final design of the heat exchanger and prior to delivery, the following issues presented a problem towards the making of the heat exchanger:

1) The in-house testing facility can only use water-water for single phase heat exchange. Testing with ammonium hydroxide solution was not possible owing to lack of proper infrastructure. The results obtained from the water-water testing would have to be extrapolated based on thermo-physical properties of ammonium hydroxide solution.

2) The heat transfer tube was a plain carbon steel tube which is resistant to ammonium hydroxide corrosion. The use of this tube with water however,

would lead to rusting or oxidation resulting in degradation of the heat transfer-microgroove surface.

3) This is for the first time that a 3D printed manifold would be used with NFFM for the microchannel heat exchanger. No prior knowledge or experience about the performance was available.

Bearing these important and pressing problems in mind, it was decided to develop a prototype using a copper tube having the same geometry and microgroove sizes. Additionally, the outer tube was replaced with a transparent plastic tube. This would enable visualization of the flow through manifold.

The prototype heat exchanger was developed from a copper tube having the same geometrical specifications as the main heat transfer (plain carbon steel tube). A 6" manifold using the 3D printing was developed and fit onto the copper tube. Copper fittings were used to make connection fittings at both the ends to provide flow both inside and outside the heat transfer tube.

Below (Table 4-2) are the geometrical specifications for the prototype solution heat exchanger:

Table 4-2: Geometrical specifications of prototype tubular microchannel heat exchanger

Components	Material	Geometrical parameters
Microgroove Tube	Copper (Thermal Conductivity – 401 W/m-K at 25 ºC)	OD: 16.2 mm OD: 18.8 mm Minimum wall under fins: 0.6 mm Fins per inch : 43

		Wall thickness: 1 mm
		Length: 304 mm
		Effective Length: 152.4 mm
Manifold	Acrylonitrile Butadiene Styrene (ABS) (Thermal conductivity – 0.17 W/m-K at 23 °C)	ID: 18.8 mm
		OD: 24.4 mm
		Wall thickness:1 mm
		Manifold channel width: 1 mm
		Pass Length: 25.4 mm
		Length: 152.4 mm
Outer Tube	Transparent Plastic Tube	ID: 18.8 mm
		OD:25.4 mm
		Length: 203 mm
Volume		0.001125 m^3
Heat Transfer area		0.008458 m^2
Heat Transfer area to volume ratio		7.517 m^2/m^3

The assembled prototype solution heat exchanger is shown in the picture (Figure 4-7) below. It is important to note here that the thermal conductivity of copper is close to 100 times higher than that of plain carbon steel. However, the conduction thermal resistance is a very small factor of the overall thermal resistance of the heat exchanger. Therefore, the change in thermal conductivity between copper and carbon steel would not cause a significant change in the overall heat transfer coefficient of the

entire heat exchanger. This will be proved in the governing equations section later in the report.

Figure 4-7: Prototype tubular microchannel heat exchanger
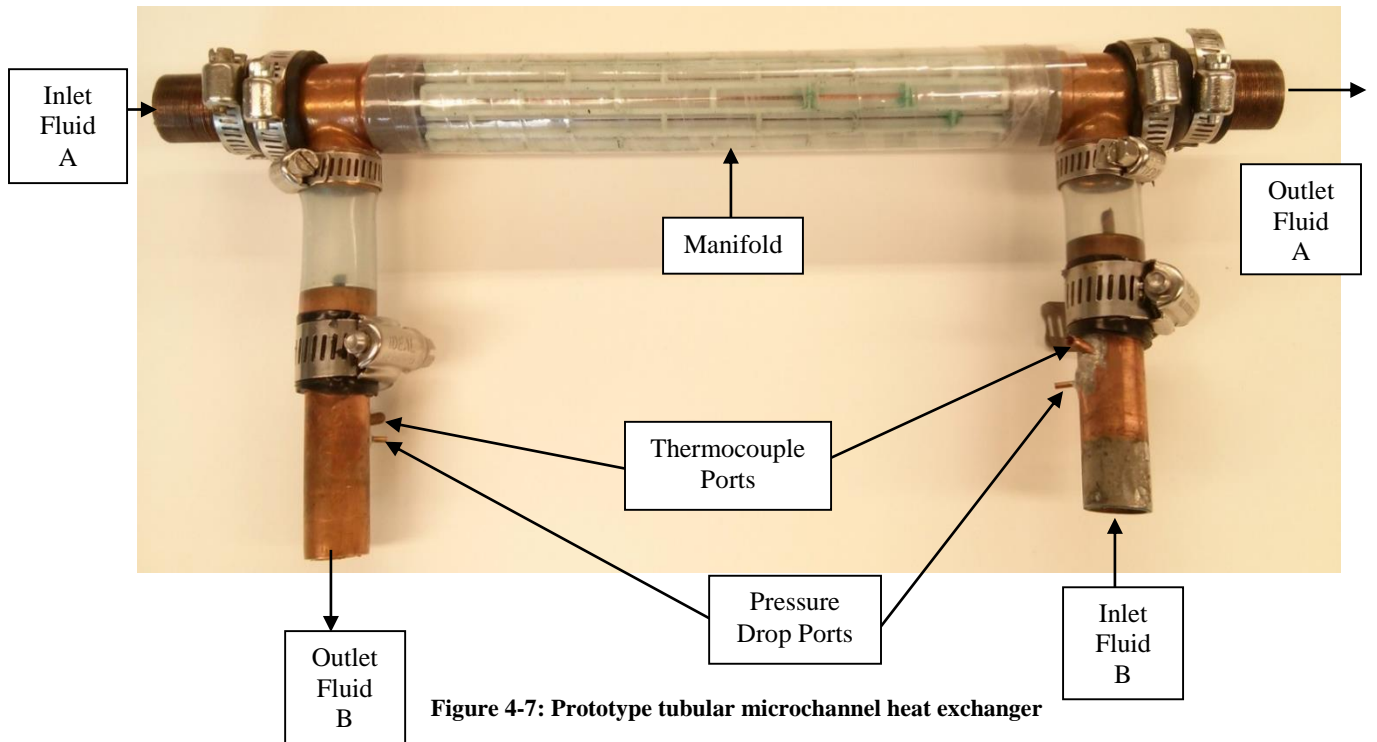
The thermocouple and pressure ports for the other side of the heat exchanger were built in the tube connections which were used while testing.

4.2 Experimental testing

In order to test the prototype heat exchanger, with water on both sides. The inlet and outlet temperatures for both the sides were measured using T-Type thermocouples. Pressure drop on the manifold side was measured using a pressure transducer. All the measured signals were processed and read using the Agilent 34970A Data logger – Data Acquisition unit.

Warm water was provided by a chiller and was passed through the heat transfer tube. The cold water also supplied by a chiller was passed through the manifold side. The instrumentation for the test set up was similar to the one used for the flat plate heat exchanger. Below is the Table 4-3 containing the list of instruments, which were used for the experimental testing.

Table 4-3: Testing equipment and instrumentation

Component Name	Manufacturer	Model	Operating Range	Accuracy
Cold Water Side Chiller	NESLAB	M75	-15 ºC to +35 ºC	± 0.15 ºC
Hot Water Side Chiller	NESLAB	HX500	+5 °C to +35 °C	± 0.1 °C
Rotameter	Omega	FL 1502A	0.145-1.45GPM	± 2 %
Mass Flow meter	GPI	A108GMN100NA1	1-50GPM	±1.5%
Thermocouples	Omega	T-type	-200 ºC to +350 ºC	± 0.3 %
Pressure Transducers	Validyne	P55D	0 -12 PSI	± 0.25 % FS
Data Acquisition system	Agilent	34970A	20 analog input channels	NA

It is important to note here that the pressure drop for the internal side of the heat transfer tube was not measured. Through its data sheet [33] Wolverine has provided

correlations to measure the inside pressure drop and the heat transfer coefficient. In order to ensure the applicability of the pressure drop correlation, experimental testing was carried out to measure the inside pressure drop for a 5ft long tube having the same internal geometry. The experimental results were verified with the correlations provided by Wolverine Tube Inc. The same correlation was then used for calculating the internal pressure drop for the prototype heat exchanger for a 6" length of the tube. The experimental pressure drop testing results are shown in the Figure 4-8 below:
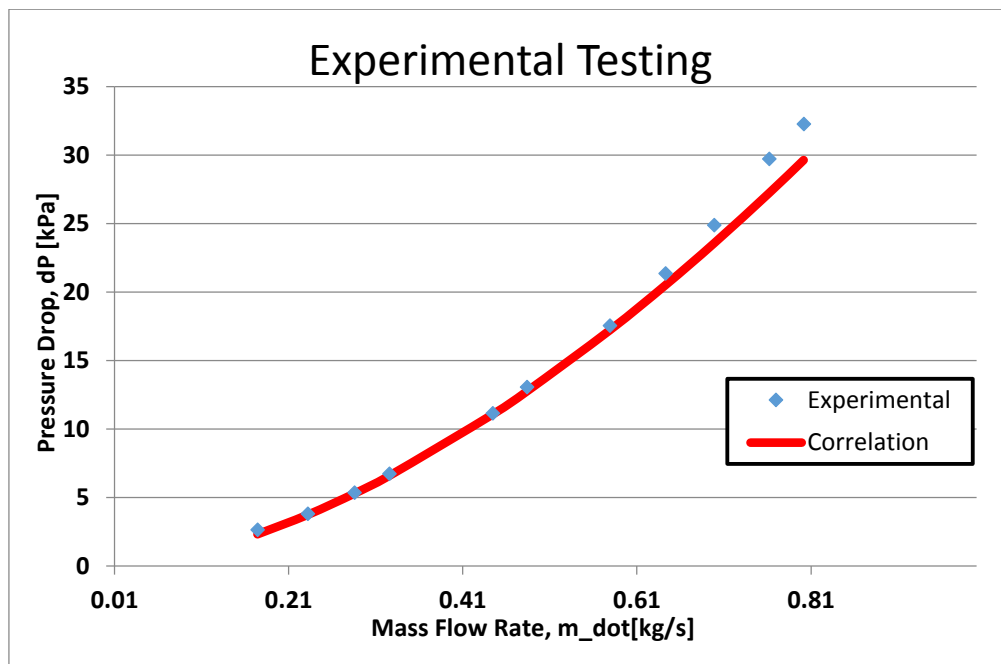
Figure 4-8: Pressure drop experimental testing and comparison with correlation

In order to test the prototype heat exchanger, the following test matrix (Table 4-4) was used to carry out the experiments:

Manifold Side Flow Rate	Manifold Side Inlet Temperature	Inside Flow Rate	Inside Inlet Temperature
9 – 100 g/s	15°C	3-13 GPM	30°C

4.3   Governing Equations

The Reynold's number and the velocity of the flow can be calculated using the continuity equation:

$$\dot{m} = \rho * A_{flow} * v \qquad\qquad \text{Eq. 20}$$

$$A_{flow} = \pi * D_i^2 \qquad\qquad \text{Eq. 21}$$

$$Re = \frac{4 * \dot{m}}{\pi * D_i * \mu} \qquad\qquad \text{Eq. 22}$$

Based on the Reynold's number, the pressure drop and the heat transfer coefficient for a 6" tube can be calculated using the wolverine correlations [33] (Table 4-5):

Table 4-5: Correlation coefficients

Parameter	Value
Tube model no.	95-4350028
STC	0.078
C	1.773
D	0.331

$$f_{darcy} = C * Re^{-D} \qquad \text{Eq. 23}$$

$$\Delta P = \frac{f_{darcy} * l * \rho * v^2}{2 * D_i} \qquad \text{Eq. 24}$$

For internal heat transfer coefficient, we use the following correlation provided by Wolverine Tubes Inc. [33]

$$h_i = \left(\frac{k}{D_i}\right) * (STC) * Re^{0.8} * \Pr^{\left(\frac{1}{3}\right)} * \left[\frac{\mu}{\mu_{wall}}\right]^{0.14} \qquad \text{Eq. 25}$$

Based on the above equations we can obtain the internal heat transfer coefficient and the pressure drop for the inside of the heat transfer tube. The heat transfer coefficient for internal flow will later be used to obtain the manifold side heat transfer coefficient.

For the outer – microchannel surface, the fluid flows into the manifold channels and is distributed microchannels. Each manifold pass is 1 inch long. Based on the geometry in Table 4-2, the microchannel surface has 43 fpi. Therefore, there are 43 fins for each manifold channel. Also, it is important to keep in mind that the flow through the microchannels can be in both the directions. Using this, the flow rate of water through the microchannels can be calculated:

$$\dot{m}_{channel} = \frac{\dot{m}_{total}}{n_{pass} * n_{channelperpass} * 2} = \frac{\dot{m}_{total}}{6 * 43 * 2} \qquad \text{Eq. 26}$$

$$Re_{channel} = \dot{m}_{channel} * \frac{D_{h_{channel}}}{\mu * A_{flow_{channel}}} \qquad \text{Eq. 27}$$

Where,

$$D_{h_{channel}} = A_{flow_{channel}} * \frac{4}{Perimeter_{channel}} \qquad \text{Eq. 28}$$

77

And,

$$A_{flow_{channel}} = w_{channel} * h_{channel}$$
Eq. 29

$$Perimeter_{channel} = 2 * (w_{channel} + h_{channel})$$
Eq. 30

The pressure drop per microchannel was measured by dividing the total pressure drop obtained through experimental reading by the number of passes. This was done so, based on the assumption that the pressure drop in the manifold channel is practically negligible as compared to the pressure drop in the microchannels.

$$\Delta P_{channel} = \frac{\Delta P_{total}}{n_{passes}} = \frac{\Delta P_{total}}{6}$$
Eq. 31

Also,

$$\Delta P_{channel} = \frac{\rho * f_{darcy} * l_{channel} * v^2}{2 * D_{h_{channel}}}$$
Eq. 32

$$l_{channel} = \pi * \frac{D_o}{12}$$
Eq. 33

The length of the microchannel from one manifold pass to the other is $1/12^{th}$ of the total circumference of the heat exchanger tube. The velocity was calculated using continuity equation,

$$\dot{m}_{channel} = \rho * A_{flow_{channel}} * v$$
Eq. 34

The above equation (Eq. 32) provided us the value for the friction factor which was later compared with conventional designs. Similarly, the Nusselt number was calculated using the following equations:

$$Nu_{experimental} = \frac{h_o * D_{h_{channel}}}{k_{water}}$$
Eq. 35

The Nusselt number was later compared with different correlations. The rest of the governing equations for the prototype heat exchanger remain similar to flat plate heat exchanger.

$$Q_{manifold} = \dot{m} * Cp * \left(T_{cold_{out}} - T_{cold_{in}}\right)$$

<div align="right">Eq. 36</div>

LMTD for counter flow configuration can be calculated from the measured values as follows:

$$LMTD = \frac{\left(\left(T_{hot_{in}} - T_{cold_{out}}\right) - \left(T_{hot_{out}} - T_{cold_{in}}\right)\right)}{LN\left(\frac{\left(T_{hot_{in}} - T_{cold_{out}}\right)}{\left(T_{hot_{out}} - T_{cold_{in}}\right)}\right)}$$

<div align="right">Eq. 37</div>

For calculating the overall heat transfer coefficient we use the following equations:

$$Q_{manifold} = U * A_{surface} * LMTD$$

<div align="right">Eq. 38</div>

The surface area for the inner and outer surface can be calculated as follows:

$$A_{surface_{inside}} = \pi * D_i * l$$

<div align="right">Eq. 39</div>

$$A_{surface_{ousidet}} = \pi * D_o * l$$

<div align="right">Eq. 40</div>

The mean surface area can therefore be calculated as

$$A_{surface} = \frac{A_{surface_{inside}} + A_{surface_{outside}}}{2}$$

<div align="right">Eq. 41</div>

Now, the overall heat transfer coefficient can be calculated as

$$\left(\frac{1}{U * A_{surface}}\right)$$

Eq. 42

$$= \left(\frac{1}{h_i * A_{surface_{inside}}}\right) + \left(\frac{LN\left(\frac{D_o}{D_i}\right)}{2 * \pi * k_{tube} * l}\right)$$

$$+ \left(\frac{1}{h_o * A_{surface_{outside}}}\right)$$

From the above equation, we can obtain the manifold side heat transfer coefficient, while the pressure drop can be directly read through the data acquisition unit.

4.4   Experimental Results

The prototype heat exchanger was tested with water on both sides. The outside surface was supplied with cold water. This side is also referred to as the Manifold side or microchannel side or simply outside. The inside was supplied with warm water. This side is simply referred to as inside or warm water side.

Preliminary results obtained from testing suggest significant improvement in performance of the tubular heat exchanger over the flat plate heat exchanger. The results show drastic reduction in pressure drop on the manifold side and also a significant increase in capacity. The variation of the overall heat transfer coefficient with manifold side mass flow rate is as shown in the graphs (Figure 4-9) below:
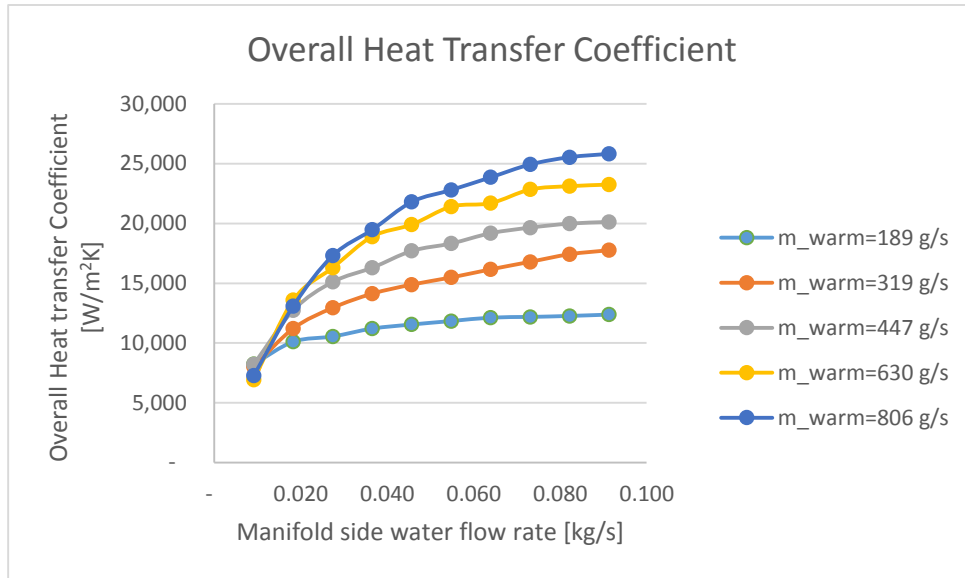
Figure 4-9: Overall Heat Transfer coefficient

The overall heat transfer coefficient is found to increase with the increase in manifold side mass flow rate. As the flow rate for the inside warm water is increased gradually, the overall heat transfer coefficient was found to increase. Such variation is expected with an increase in flow rate. As the flow rate is increased, so does the Reynold's number of that flow. This influences the Nusselt number. Based on the calculations, the maximum Reynold's number which is associated with the maximum flow rate test condition, was found to be 507. According to the classical theory the Nusselt number for a fully developed laminar flow and a constant aspect ratio of rectangular channel, is constant. However, based on experimental results, in spite of the flow through the channel remaining in the laminar flow region (Re<2300), the heat transfer coefficient has an increasing trend with the water flow rate. This lends credibility to the belief that the flow which enters the microchannels is essentially under developed flow. The smaller flow lengths due to NFFM allow this to occur. A similar trend was observed for the outside heat transfer coefficient which is essentially also

81

representative of the trend for the Nusselt number. The outside or manifold side heat transfer coefficient was calculated using the Eq. 42. The Figure 4-10 shows the variation of manifold side heat transfer coefficient with water flow rate.
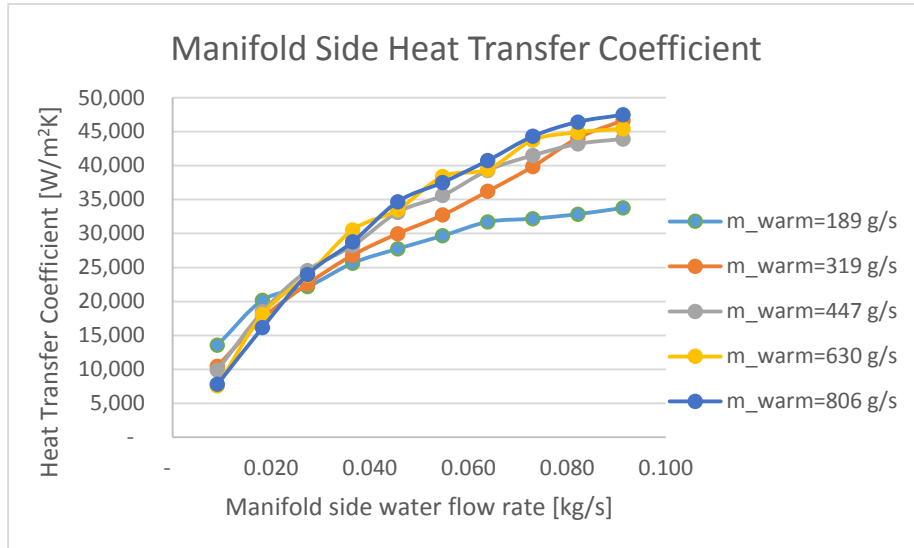
Figure 4-10: Variation of manifold (outside) heat transfer coefficient with water flow rate

The inside heat transfer coefficient was calculated using the wolverine correlations and was found to follow the expected trend. It was found to vary only with the inside water flow rate. The pressure drop for the manifold side was found to increase with the outside water flow rate. The variation for the outside pressure drop is shown in Figure 4-11 below:
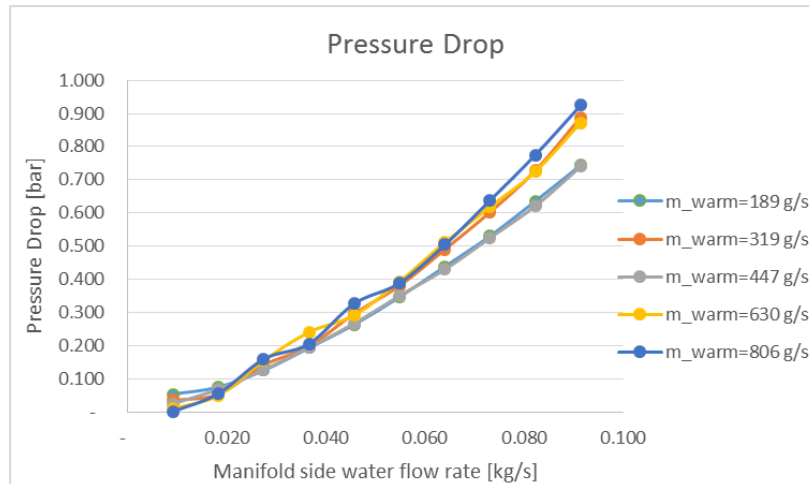
Figure 4-11: Variation of pressure drop with water flow rate

The total heat transfer obtained for the 6" prototype was found to be much higher than that of the flat plate heat exchanger. Figure 4-12 below shows the variation of heat transfer capacity with water flow rate.
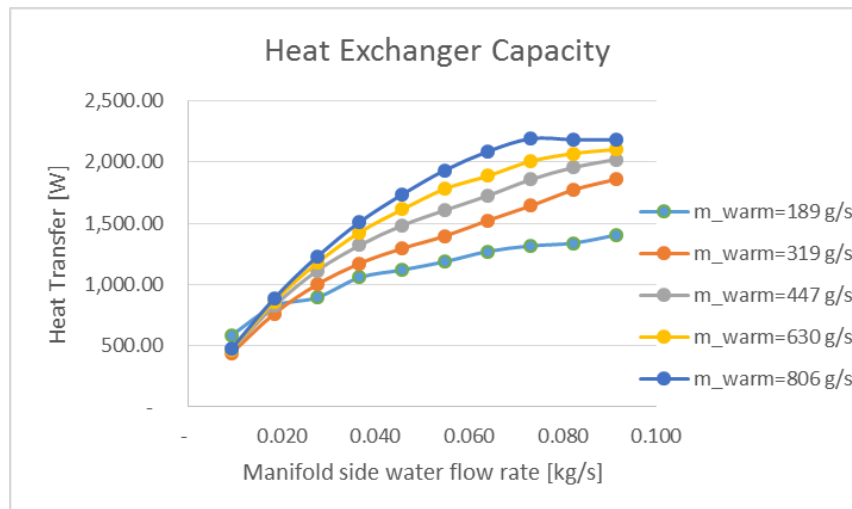
Figure 4-12: Heat Transfer vs water flow rate for tubular heat exchanger

The results show considerably high heat transfer capacity for the small 6" tube. Using the results for the pressure drop and the heat transfer capacity, it would be possible to assess the total length of the heat exchanger that would be required to meet the required specifications for an 11kW solution heat exchanger

CHAPTER 5:   COMPARISON OF HEAT EXCHANGERS

The two single phase heat exchangers discussed in chapter 3 and chapter 4 were compared with each other to observe the thermal performance. Although the first heat exchanger is a tubular heat exchanger while the other heat exchanger is a flat plate heat exchanger, both the heat exchangers were compared on the basis of the following parameters:

5.1   Comparison of Flat Plate and Tubular Heat Exchangers

1) Heat flux vs Pressure Drop

The variation of the heat flux with the pressure drop provides the heat transferred per unit area of the heat exchanger as against the pressure drop penalty it incurs. This gives us an idea of the performance of the heat exchanger for a certain limiting value of the pressure drop. So, if we have a limit of 1 bar, then for the same geometry the maximum capacity for both the heat exchangers can be obtained. The Figure 5-1 given below shows the comparison of heat flux vs pressure drop for both the heat exchangers.
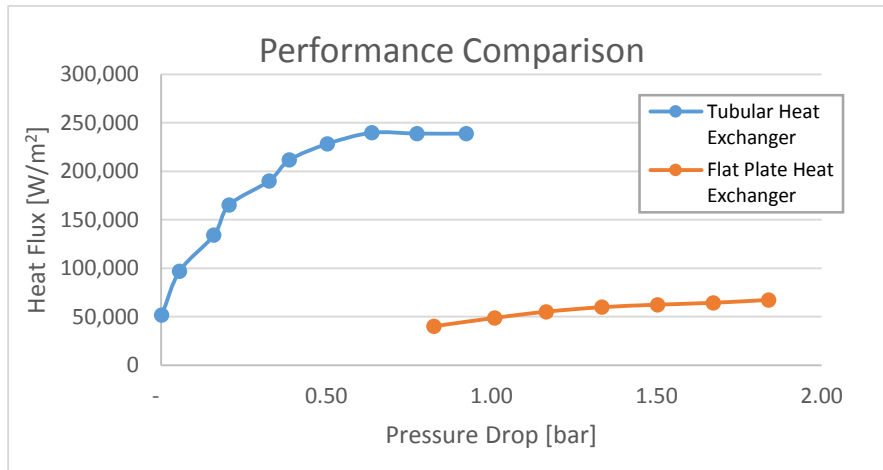
Figure 5-1: Comparison of heat flux vs pressure drop for flat plate and tubular heat exchangers

2) Heat Transfer and Pressure Drop density

The heat transfer density is calculated by dividing the total capacity of the heat exchanger divided by the total box volume of the heat exchanger. The box volume of the heat exchanger is mentioned in Table 4-2. The box volume represents the cubical volume formed by multiplying the maximum dimensions of the heat exchanger in x, y and z direction. The Figure 5-2 shows the comparison of heat transfer per volume with water flow rate. Similarly, the pressure drop density is defined as the ratio of the pressure drop and the box volume. Figure 5-3 shows the variation of pressure drop density with water flow rate.
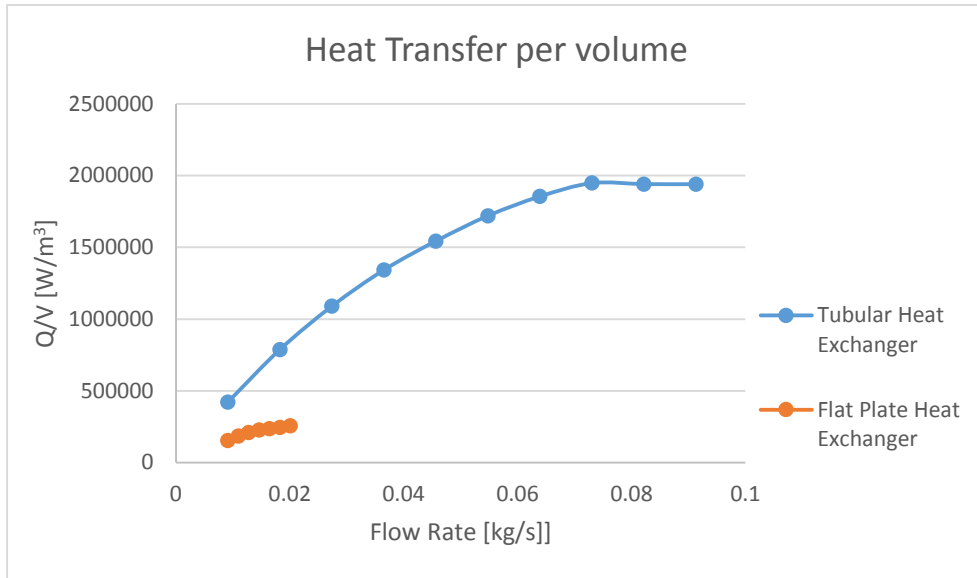
Figure 5-2: Comparison of heat transfer per volume of the heat exchangers
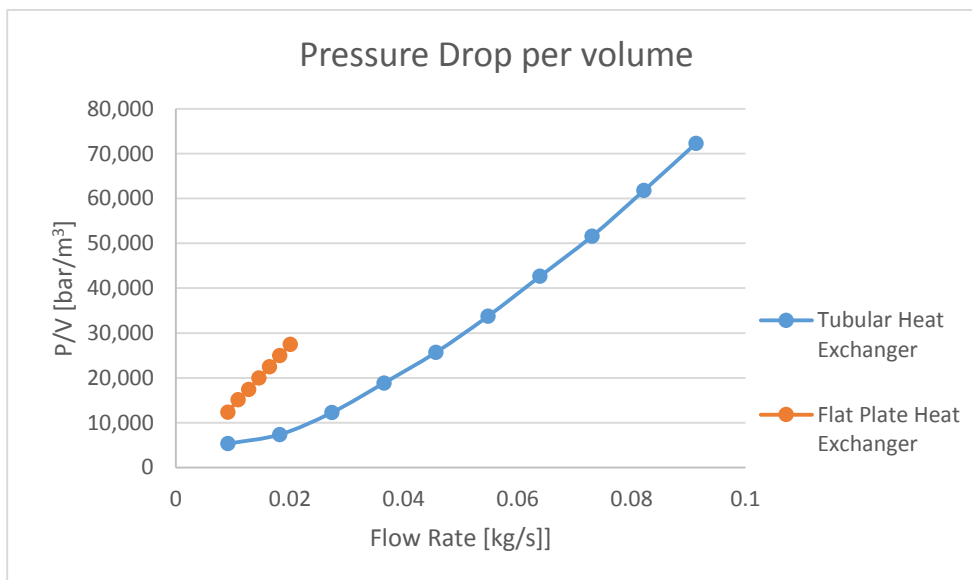
Figure 5-3: Pressure drop per volume of the heat exchangers

3) Heat Transfer Area to Volume ratio:

The ratio of heat transfer area to total volume is a property of the heat exchanger which defines the compactness of the heat exchangers. Based on the results the tubular heat exchanger has a higher heat transfer area to volume ratio. This indicates that the tubular heat exchanger is more compact then the flat plate heat exchanger (Figure 5-4).
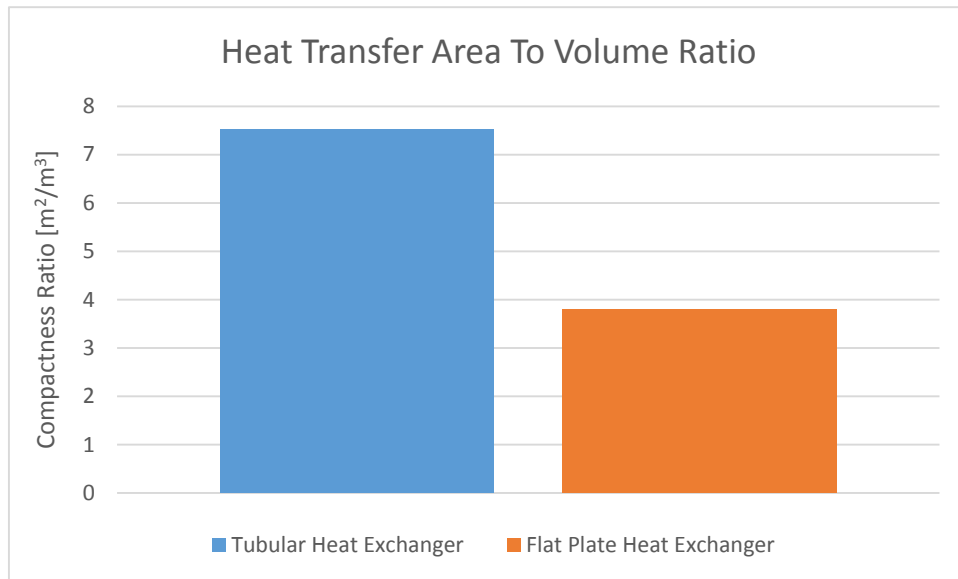
Figure 5-4: Comparison of heat transfer are to volume ratio

Based on the results highlighted above for comparison of both the heat exchangers, it may be noted that the thermal performance of the tubular heat exchanger is significantly higher than the flat plate heat exchanger. The flat plate heat exchanger also offers a much higher pressure drop which is also the reason why the heat exchanger was never tested for higher flow rates. Finally, the compactness ratio for the tubular heat exchanger is more than double the ratio for the flat plate heat exchanger. This clearly indicates that the tubular heat exchanger is more compact than flat plate heat exchanger.

5.2   Comparison of Performance with Existing Correlations

Extensive research has been conducted on laminar and turbulent flow through heat exchangers. This includes flow through circular and non-circular channels. As mentioned earlier there is less agreement among these different correlations and this makes the comparison of the experimental data with the existing correlations all the more challenging.

As mentioned earlier, one of the main reasons for enhancement in thermal performance is because of the influence of developing region heat transfer. As the fluid passes from the manifold channel to the microchannel, the change in area causes the fluid to enter the developing region. Theoretically, the heat transfer coefficient in the developing region is much higher than the heat transfer coefficient in the fully developed region. For Laminar flow, based on conventional correlations, the heat transfer coefficient is highest at the entrance and decreases to a constant value in the developed flow region. This trend is shown through the Figure 5-5 given below:

$$\xi = \frac{x/D}{Re_D Pr}$$
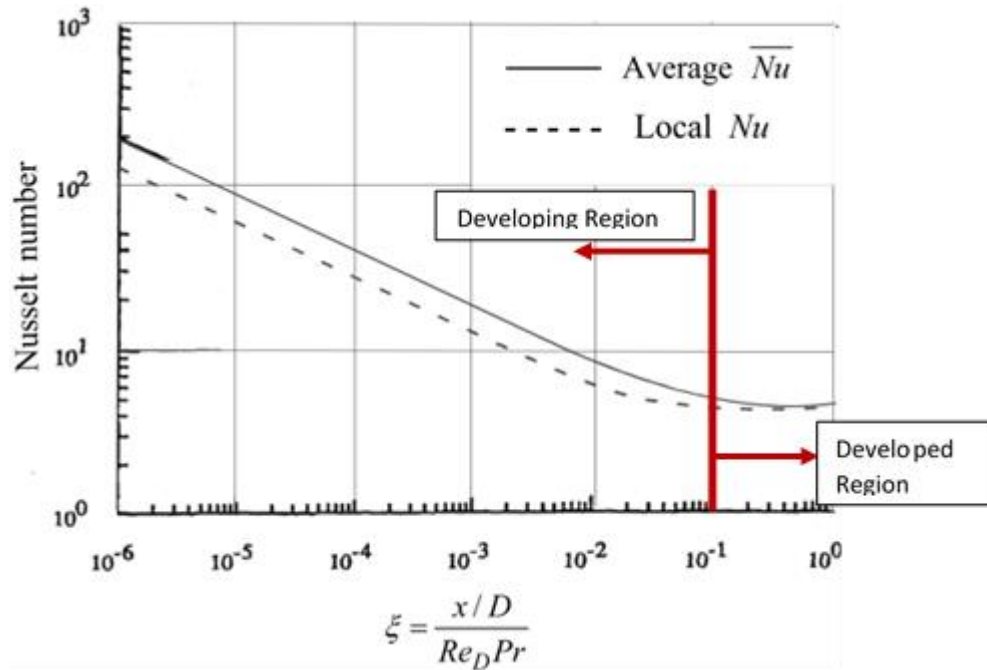
Figure 5-5: Variation of Nusselt number with charateristic length for a typical channel flow

The transition from a continuously decreasing trend to a constant value marks the entrance region length for the channel. This length depends on the geometry of the channel, the flow specifications and the fluid properties. A similar trend was observed for the channel flow through the tubular microchannel heat exchanger. The result was also compared with existing correlations, to observe if the experimental results conform to any established correlation.
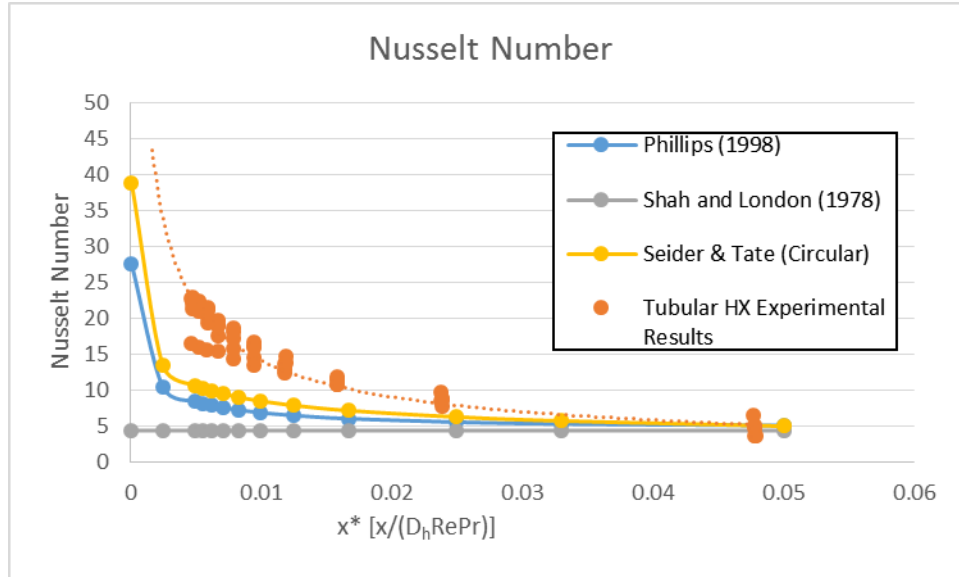
Figure 5-6: Comparison of experimental testing results with existing correlations

From the comparison above (Figure 5-6), it is clear that the thermal performance of the experimental results are close to the predictions made by Phillips [34]. The correlation developed by Phillips uses the Shah and London[35] correlation; for laminar flow through rectangular microchannels for constant heat flux condition; as an input value.

Shah and London [35]:

$$Nu_{FD} = 8.235 * \left(1 - \frac{2.0421}{\alpha} + \frac{3.0853}{\alpha^2} - \frac{2.4765}{\alpha^3} + \frac{1.0578}{\alpha^4} - \frac{0.1861}{\alpha^5}\right) \qquad \textbf{Eq. 43}$$

Where, α ($\alpha \geq 1$) is the channel aspect ratio, if $\alpha < 1$ it is recommended to use α^{-1}.

Phillips [34]:

$$Nu_3 = Nu_4 * \left(\frac{Nu_{FD_3}}{Nu_{FD_4}}\right)$$

Where, Nu_{FD_3} and Nu_{FD_4} are Nusselt number for fully developed Lamniar flow for uniform surface heat flux, with heating provided from 3 sides and 4 sides respectively. The Nu_4 is the Nusselt number for Laminar flow in a rectangular microchannel for thermally developing flow with heating from all four sides.

The values for these Nusselt number values were extrapolated from the following Figure 5-7 and Figure 5-8 [36]

	$Nu_{D_h(4)}$					$Nu_{D_h(3)}$
z^*	$A = 1.0$	$A = 2.0$ or 0.5	$A = 3.0$ or 0.333	$A = 4.0$ or 0.25	$0.1 \geq A \geq 10$	$A \geq 10$
0.0001	25.2	23.7	27.0	26.7	31.4	31.6
0.0025	8.9	9.2	9.9	10.4	11.9	11.2
0.005	7.10	7.46	8.02	8.44	10.0	9.0
0.00556	6.86	7.23	7.76	8.18	9.8	8.8
0.00625	6.60	6.96	7.50	7.92	9.5	8.5
0.00714	6.32	6.68	7.22	7.63	9.3	8.2
0.00833	6.02	6.37	6.92	7.32	9.1	7.9
0.01	5.69	6.05	6.57	7.00	8.8	7.5
0.0125	5.33	5.70	6.21	6.63	8.6	7.2
0.0167	4.91	5.28	5.82	6.26	8.5	6.7
0.025	4.45	4.84	5.39	5.87	8.4	6.2
0.033	4.18	4.61	5.17	5.77	8.3	5.9
0.05	3.91	4.38	5.00	5.62	8.25	5.55
0.1	3.71	4.22	4.85	5.45	8.24	5.40
1.0	3.60	4.11	4.77	5.35	8.23	5.38

Adapted from Phillips (1988).

Figure 5-7: Nusselt numbers for laminar thermally developing flow for different aspect ratio of channels with respect to thermal entry length z*. The subscripts 4 and 3 refer to heating being provided from four sides and three sides respectively. All values are for constant surface heat flux condition

And [36],

$A = W/H$	$Nu_{D_h(4)}$	$Nu_{D_h(3)}$
0.0	8.24	8.24
0.1	6.70	6.94
0.2	5.70	6.07
0.3	4.97	5.39
0.4	4.46	4.89
0.5	4.11	4.51
0.6	3.88	—
0.7	3.74	3.99
0.8	3.66	—
0.9	3.61	—
1.0	3.60	3.56
1.43	3.74	3.20
2.0	4.11	3.15
2.5	4.46	3.17
3.33	4.97	3.31
5.0	5.70	3.64
10.0	6.70	4.25
∞	8.24	5.39

Adapted from Phillips (1988) and Shah and London (1978), with
results attributed to F.W. Schmidt.

**Figure 5-8: Nusselt numbers for laminar fully developed
flow for different aspect ratios A. The subscripts 4 and 3
refer to heating being provided from four sides and three
sides respectively. All values are for**

The results are also close in agreement with the Seider and Tate's[37]

correlation for circular microchannels.

Sieder and Tate [37]:

$$Nu_{Dh} = 1.86 * (x^*)^{-0.33}$$

Eq. 45

Where x* is the thermal entry length scale which is calculated as:

$$x^* = \frac{L_{chnnel}}{D_{h_{channel}} * Re_{Dh} * Pr}$$

Eq. 46

Where Re refers to the Reynold's number of the flow through the microchannel

and Pr refers to the Prandtl number which is calculated based on average water

temperature obtained through experimental data. The behavior of Nusselt number with

the variation in length scale x* also follows the expected trend from developing region

to fully developed conditions. Although the experimental predictions over predict the

theoretical values, the fact that they essentially follow a similar trend, ensures credibility

of the experimental findings. The difference in both the values may also be due to the NFFM mechanism. The effect due to centripetal motion of the flow and due to the impingement of the flow on the microchannel base was not considered in the theoretical correlations. Therefore, it is certain that the theoretical predictions would be lower than the experimental results.

Apart from validation of experimental results, the comparison also provides useful information regarding the fact that the advantages of using NFFM is not just restricted to the fact that the flow is through the microchannels. The normal flow which causes the impinging of the flow and the curving of the fluid flow through the channel are equally important contributors to the enhancement in heat transfer performance due to NFFM.

5.3 Comparison with Contemporary State-of-the-Art Heat Exchangers

The tubular heat exchanger was also compared with conventional state of the art designs of heat exchangers. The Chevron plate heat exchanger was chosen for comparison. Many research articles have studied the chevron plate heat exchanger. Correlations for the heat exchangers are based on the chevron angle and the Reynold's number of the flow through the chevron channels. Only the tubular heat exchanger was compared with the heat exchangers. The flat plate heat exchanger was not tested with a higher range of flow rates. Therefore, its Reynold's number was limited to 34. Also it was difficult to predict the performance of the heat exchanger for higher flow rates based on the experimental test range. For comparison, a range of different correlations

have been presented by Ayub [38]. From all the different correlations, the correlation developed by Kumar [39] was used for comparison (Figure 5-9).

Kumar [5]
$$Nu = C_1 Re^m Pr^{0.33}(\mu/\mu_w)^{0.17}$$
$$f = C_2/(Re)^p$$

Water, herringbone plates, $\phi = 1.17$
$C_1, C_2, m,$ and p are constants and given as:

β	Re	C_1	m	Re	C_2	p
≤ 30	≤ 10	0.718	0.349	<10	50.0	1.0
	>10	0.348	0.663	10–100	19.40	0.589
				>100	2.990	0.183
45	<10	0.718	0.349	<15	47.0	1.0
	10–100	0.400	0.598	15–300	18.29	0.652
	>100	0.300	0.663	>300	1.441	0.206
50	<20	0.630	0.333	<20	34.0	1.0
	20–300	0.291	0.591	20–300	11.25	0.631
	>300	0.130	0.732	>300	0.772	0.161
60	<20	0.562	0.326	<40	24.0	1.0
	20–400	0.306	0.529	40–400	3.24	0.457
	>400	0.108	0.703	>400	0.760	0.215
≥ 65	<20	0.562	0.326	<50	24.0	1.0
	20–500	0.331	0.503	50–500	2.80	0.451
	>500	0.087	0.718	>500	0.639	0.213

Figure 5-9: Correlations for Chevron plate heat exchanger for different chevron angles, laminar flow conditions as developed by Kumar (1984) mentioned in Ayub (2010)

The correlation used was for 4 different chevron angles ($\beta \geq 65, \beta = 60, 50, 45$). The graphs (Figure 5-10) below show the variation of Nusselt number with the Reynold's number for different Chevron angles.
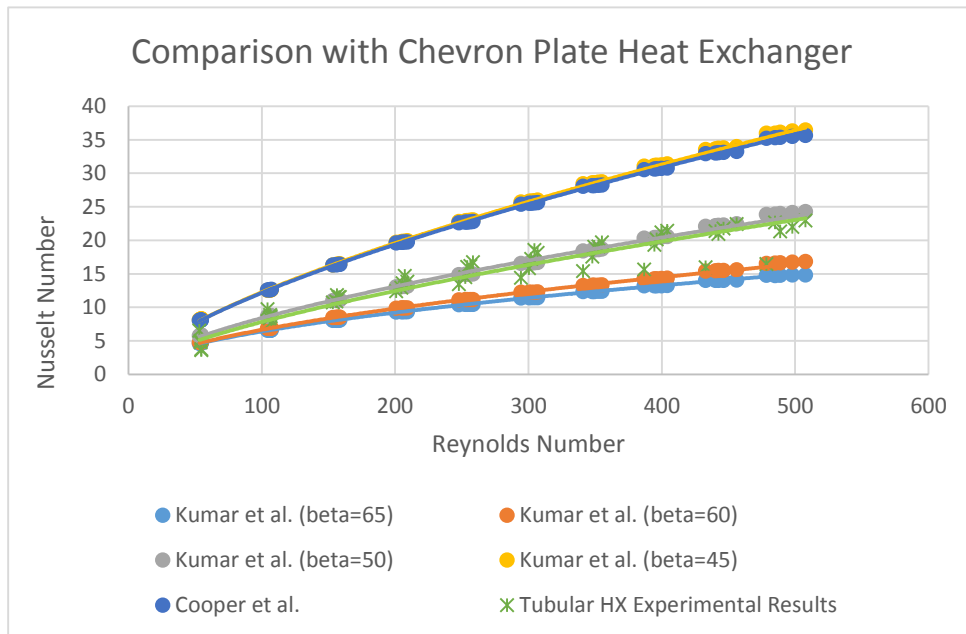
Figure 5-10: Comparison of Nusselt number of Tubular heat exchanger with state of the art heat exchangers

95

The plot shows that the tubular heat exchanger has a performance which is comparable to the state of the art designs. Based on the graph it may be construed that the performance of the heat exchanger matches best with a Chevron flat plate heat exchanger having a chevron angle of 50°. It is also important to note here that although the performance of both these heat exchangers seem to be similar, the actual size weight and dimensions were not considered. Due to the compactness of the tubular heat exchanger, the overall reduction in size may be an important factor. Similar to the previous graph, the tubular heat exchanger was compared with other state of the art heat exchangers for the variation in friction factor with the Reynold's number (Figure 5-11).
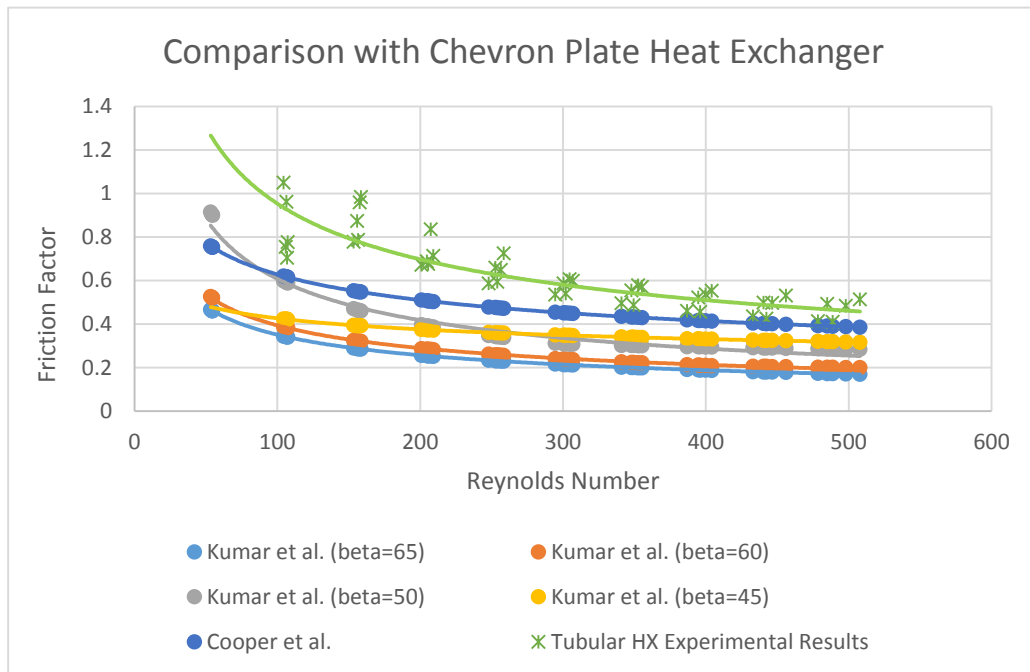
Figure 5-11: Comparison of friction factor of tubular heat exchanger with state of the art heat exchangers

The comparison of the friction factor indicates that the resistance to flow through the channels of the heat exchanger is higher in case of the tubular heat exchanger. The Chevron plate heat exchanger has a lower frictional resistance to flow. The reason for a higher friction factor, might arise from the fact that microchannels are associated with a larger pressure drop. Another important point which might play an influence is the fabrication of the microchannels. The chevron plate channels are easy to fabricate as compared to microchannels on a tubular surface. Further, different polishing techniques may be employed to reduce the surface roughness of the chevron plate channels. The microchannels on the other hand are difficult to polish and minute roughness issues remain inherent in the microchannels.

5.4 Comparison of Effectiveness and NTU

Another important comparison which could be made for the heat exchanger is with respect to the effectiveness and NTU of the heat exchanger. The effectiveness of a heat exchanger is a measure of the efficiency of the heat exchanger. It refers to the ratio of the actual heat transferred by the heat exchanger with the maximum possible heat which can be transferred by the heat exchanger.

$$Q_{max} = C_{min} * (T_{hot_{in}} - T_{cold_{in}})$$

Eq. 47

Where, C refers to the heat capacity

$$C_{cold} = \dot{m}_{cold} * Cp_{cold}$$

Eq. 48

$$C_{hot} = \dot{m}_{hot} * Cp_{hot}$$

Eq. 49

C_{min} refers to the minimum value of the heat capacity between the cold side and the hot side. The lower the value of the heat capacity, the large would be the value of

97

the temperature difference. Therefore, for obtaining the maximum possible heat transfer which takes in the maximum possible temperature difference, the heat capacity would be C_{min}. In order to calaulate the effectiveness we use the following equation Eq. 50:

$$\varepsilon = \frac{Q_{actual}}{Q_{max}}$$

Eq. 50

Where, Q_{actual} refers to the actual heat transfer capacity. The NTU for a heat exchanger can be calculated using the following equation Eq. 51:

$$NTU = \frac{UA}{C_{min}}$$

Eq. 51

Using equations Eq. 50 and Eq. 51 the effectiveness and NTU of both the flat plate and the tubular heat exchanger were calculated. These effectiveness and NTU values were then compared with the correlations for Counter flow heat exchanger [40]. The correlation for counter flow heat exchanger for effectiveness – NTU for different heat capacity ratios is given below:

For $C_r < 1$

$$\varepsilon = \frac{1 - e^{(-NTU(1-C_r))}}{1 - C_r\left(e^{(-NTU(1-C_r))}\right)}$$

Eq. 52

For $C_r = 1$

$$\varepsilon = \frac{NTU}{1 + NTU}$$

Eq. 53

Where, C_r is the heat capacity ratio which is given by:

98

$$C_r = \frac{C_{min}}{C_{max}}$$

Using the above equations the value of effectiveness vs NTU for a counter flow heat exchanger was compared with the values obtained from experimental testing of the flat plate heat exchanger. For this, the flow rates on both the sides of the heat exchanger were equal. Moreover, minor variations in Cp as a result of difference in temperature of 15°C were ignored. As a result the C_r calculated for this heat exchanger was equal to 1. The Figure 5-12 [40] below shows the comparison of flat plate heat exchanger with NTU-effectiveness relationship for counter flow heat exchangers.
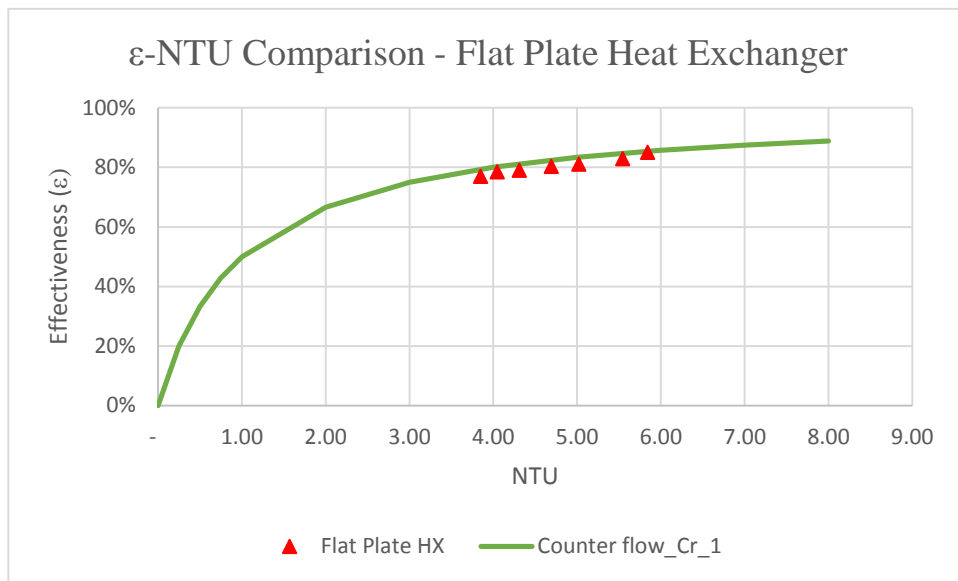
Figure 5-12: Comparison of Counter flow heat exchanger effectiveness- NTU correlation with experimental test results for flat plate heat exchanger

Similarly, for the tubular heat exchanger, the values of Cr and NTU which were considered were taken based on experimental data (Figure 5-13). The correlation [40] was used to calculate the actual relationship of effectiveness and NTU for counter flow heat exchanger. This was subsequently compared with experimentally obtained values.
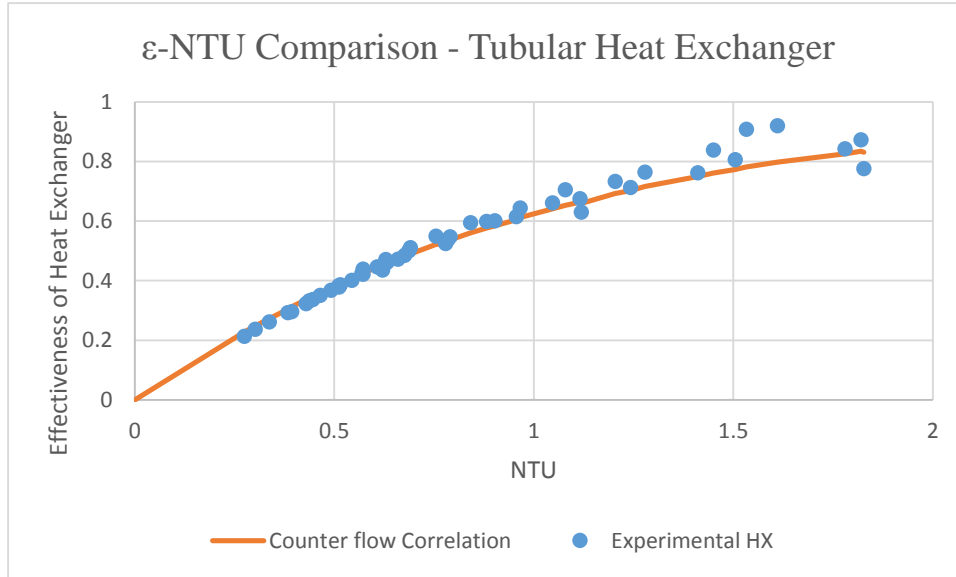
Figure 5-13: Comparison of Effectiveness-NTU correlation for counter flow heat exchanger with experimental results of tubular microchannel heat exchanger.

The comparison of the heat exchanger experimental performance with existing correlations shows a strong match. This verifies the fact that the heat exchanger perform as a counter flow heat exchanger.

CHAPTER 6:   CONCLUSION AND

FUTURE WORK

6.1   Summary and Conclusions

The fractal normal flow heat exchanger combines high heat transfer characteristics of microchannels with very low pressure drop, however they are naturally suited for cross-flow configuration due to short length of fractal microgrooves. At the same time majority of industrial processes require counter flow heat transfer arrangement that improves efficiency of the processes. Counter flow heat exchanger can be made of those short fractal manifold microchannel sections by arranging them in a multi-pass flow arrangement. For this a baffled manifold design was conceived and evaluated for first time in this work. Two single phase flow heat exchangers were developed to serve as potential solution heat exchangers for an ammonia water absorption refrigeration system. Both heat exchangers were tested in lab with water.

First, a proof of concept heat exchanger was fabricated using a flat plate design. Nickel microgroove plates were used which were manufactured by Wolverine Tube Inc. A Teflon plate was used to fabricate the manifold by creating minichannels on it. The heat exchanger demonstrated high effectiveness of around 80% and approach temperatures of both hot and cold satisfied the requirement for actual operation as solution heat exchangers. The overall heat transfer coefficient of 20,000 W/m^{2}K was obtained at flow rates as low as 20g/s. This corresponds to a heat transfer coefficient of

close to 45,000 W/m^{2}K, which is significantly higher as compared to plate heat exchangers commonly used for this application. In spite of superior thermal performance, the pressure drop of this heat exchanger was relatively high due to small hydraulic diameter of microchannels on individually produces nickel plates.

In order to advance this concept further, a low cost manufacturing process was used for developing a second counter flow heat exchanger. This time the concept was applied to a tubular design. For this purpose, a commercially produced tube manufactured by Wolverine Tube Inc. was used for heat exchanger development. The other unique aspect about this heat exchanger is the application of additive manufacturing for manifold development. By using additive manufacturing, parts of heat exchangers which are not required to transfer heat (such as – manifolds and headers) can be made from polymer based materials. For such purposes – especially for complex geometries, 3D printing is ideally suited. To the best knowledge of the author, this was for the first time that 3D printing and additive manufacturing techniques were applied for manifold development of microchannel heat exchangers.

The tubular heat exchanger demonstrated excellent thermal performance. An effectiveness of over 90% was obtained through experimental testing. It was also found to outperform the flat plate heat exchanger on three fronts:

1) Heat flux vs the pressure drop – For the same value for pressure drop around 0.8 bar, the heat flux removal for tubular heat exchanger was about 250,000 W/m2 while that of flat plate heat exchanger was only 50000 W/m2K. This indicates a thermal performance enhancement of around 5 times

2) Heat transfer capacity and pressure drop per box volume – For the same flow rate the tubular heat exchanger thermal performance was found to be 3 times higher than the flat plate design while the pressure drop per volume was found to be 3.3 times lower for the tubular design.

3) Heat transfer area per unit volume – The heat transfer area per volume of the heat exchanger indicates the compactness of the heat exchanger. It was found that the tubular design had an area to volume ratio of around 7.5 which was twice as more compact as compared to the flat plate design which had a surface area to volume ratio of 3.8.

The performance of the tubular heat exchanger was also compared with conventional correlations. The experimental results over predicted most of these correlations, suggesting that the performance was prominently better than simply flow through the microchannels. Finally the heat exchanger was also compared with contemporary state of the art heat exchangers. Correlations for chevron plate heat exchanger provided by Kumar (1984) [39] for different Chevron angles was used for comparison. The heat exchanger was found to compare well with these results. The friction factor of the heat exchanger was marginally higher than the chevron plate heat exchanger. The Nusselt number on the other hand had better performance than the higher chevron angle heat exchangers. Although the heat exchangers may not have the best performance as compared to the chevron plate heat exchanger, lack of data regarding the size and dimensions of the chevron plate heat exchanger make the comparison difficult. The current dimensions of the tubular heat exchanger are not optimized, thus there is sufficient scope available to further improve the performance.

The thermo-fluidic optimization can be done on both the manifold design and heat exchanger core as well.

6.2   Proposed Future Work

Counter flow heat exchangers which use normal flow feed mechanism show significant opportunity in developing high performance, compact heat exchangers. The current study paves the way for future development in this area. Using the experience of the flat plate and the tubular heat exchanger optimized heat exchangers can be developed which would potentially perform better than current state of the art heat exchangers. The following bullet points sum up the future work and possibilities in developing heat exchangers with Normal Feed Flow Mechanism:

1) The performance of the heat exchangers may be improved by developing an optimization model. Current non-optimized design performs close to current state-of-the-art heat exchangers.

2) The use of 3D printing technology must be expanded to two phase flow and flat plate heat exchanger.

3) Intricate designs of the manifold can now be developed with ease because of the 3D printing technique. This should promote further testing of different manifold feed designs.

4) The numerical model developed for the flat plate heat exchanger may also be used for testing of different manifold designs. By developing an optimization model which uses the CFD code to numerically predict the heat transfer and

flow performance would be a useful package to experiment with innovative designs.

5) Although Nickel has a superior thermal conductivity as compared to stainless steel or plan carbon steel, fabricating Nickel is a tough challenge. The option of using steel should be considered. Furthermore, if the thickness of the heat exchanging surface is reduced, the thermal resistance reduces. This also makes the heat exchanger performance less dependent on the heat exchanging material.

References

1. Cengel, Y.A., Turner, R. H., Cimbala, J. M., *Fundamentals of Thermal-fluid Sciences*. 4th edition ed. 2012, London: McGraw Hill Higher Education.
2. Vali, A., et al., *Numerical model and effectiveness correlations for a run-around heat recovery system with combined counter and cross flow exchangers.* International Journal of Heat and Mass Transfer, 2009. **52**(25–26): p. 5827-5840.
3. Zhan, C., et al., *Comparative study of the performance of the M-cycle counter-flow and cross-flow heat exchangers for indirect evaporative cooling – Paving the path toward sustainable cooling of buildings.* Energy, 2011. **36**(12): p. 6790-6805.
4. Kays, W.M., R.K. Jain, and S. Sabherwal, *The effectiveness of a counter-flow heat exchanger with cross-flow headers.* International Journal of Heat and Mass Transfer, 1968. **11**(4): p. 772-774.
5. Shah, R.K. and D.P. Sekulic, *Fundamentals of Heat Exchanger Design*. 2003, New Jersey: John Wiley & Sons, Inc.
6. Chen, Y. and P. Cheng, *Heat transfer and pressure drop in fractal tree-like microchannel nets.* International Journal of Heat and Mass Transfer, 2002. **45**(13): p. 2643-2648.
7. Wang, X.-Q., A.S. Mujumdar, and C. Yap, *Thermal characteristics of tree-shaped microchannel nets for cooling of a rectangular heat sink.* International Journal of Thermal Sciences, 2006. **45**(11): p. 1103-1112.
8. Tuckerman, D.B. and R.F.W. Pease, *HIGH-PERFORMANCE HEAT SINKING FOR VLSI.* Electron device letters, 1981. **EDL-2**(5): p. 126-129.
9. Samalam, V., K, *Convective Heat Transfer in Microchannels.* Journal of Electronic Materials, 1989. **18**.
10. Adams, T.M., et al., *Applicability of traditional turbulent single-phase forced convection correlations to non-circular microchannels.* International Journal of Heat and Mass Transfer, 1999. **42**(23): p. 4411-4415.
11. Adams, T.M., et al., *An experimental investigation of single-phase forced convection in microchannels.* International Journal of Heat and Mass Transfer, 1998. **41**(6–7): p. 851-857.
12. Gnielinski, V., *New equations for heat and mass transfer in turbulent pipe and channel flow.* International Chemical Engineering 1976(16): p. 359–368.
13. Lee, P.-S., S.V. Garimella, and D. Liu, *Investigation of heat transfer in rectangular microchannels.* International Journal of Heat and Mass Transfer, 2005. **48**(9): p. 1688-1704.
14. Harms, T.M., M.J. Kazmierczak, and F.M. Gerner, *Developing convective heat transfer in deep rectangular microchannels.* International Journal of Heat and Fluid Flow, 1999. **20**(2): p. 149-157.

15. Grigull, U. and H. Tratz, *Thermischer einlauf in ausgebildeter laminarer rohrströmung.* International Journal of Heat and Mass Transfer, 1965. **8**(5): p. 669-678.

16. Rahman, M.M., *Measurements of heat transfer in microchannel heat sinks.* International Communications in Heat and Mass Transfer, 2000. **27**(4): p. 495-506.

17. Owhaib, W. and B. Palm, *Experimental investigation of single-phase convective heat transfer in circular microchannels.* Experimental Thermal and Fluid Science, 2004. **28**(2–3): p. 105-110.

18. Papautsky, I., T. Ameel, and A.B. Frazier, *A Review Of Laminar Single-Phase Flow In Microchannels*, in *ASME International Mechanical Engineering Congress and Exposition*, ASME, Editor. 2001: New York, NY.

19. Peng, X.F., et al., *Experimental investigation of heat transfer in flat plates with rectangular microchannels.* International Journal of Heat and Mass Transfer, 1995. **38**(1): p. 127-137.

20. Wang, B.X. and X.F. Peng, *Experimental investigation on liquid forced-convection heat transfer through microchannels.* International Journal of Heat and Mass Transfer, 1994. **37, Supplement 1**(0): p. 73-82.

21. Kandlikar, S.G., et al., *Heat Transfer in Microchannels—2012 Status and Research Needs.* Journal of Heat Transfer, 2013. **135**(9): p. 091001-091001.

22. Palm, B., *HEAT TRANSFER IN MICROCHANNELS.* Microscale Thermophysical Engineering, 2001. **5**(3): p. 155-175.

23. Sobhan, C.B. and S.V. Garimella, *A COMPARATIVE ANALYSIS OF STUDIES ON HEAT TRANSFER AND FLUID FLOW IN MICROCHANNELS.* Microscale Thermophysical Engineering, 2001. **5**(4): p. 293-311.

24. BCS, I., *Waste Heat Recovery: Technology and Opportunities in U.S. Industry.* 2008.

25. Shi, J. and S. Bushart, *Strategic Program: Water Use & Availability.* 2013, Electric Power Research Institute: Palo Alto CA.

26. Brooks, F.J., *GE Gas Turbine Performance Characteristics.* GE Power Systems: Schenectady NY.

27. Dessiatoun, S.V., E. Al-Hajri, and M. Alshehhi, *HIGH EFFICIENCY ENERGY RECOVERY AND GAS SWEETNING UTILIZING ADVANCED MICROCHANNEL HEAT & MASS EXCHANGERS* 2013, University of Maryland: College Park MD.

28. Hwang, Y., *Absorption Technologies.* 2013, Center for Environmental Energy Engineering.

29. Ericson, D.E., *Heat Actuated Cooling System: Light Weight 1.5 Ton AARU* 2012, Energy Concepts Co. LLC. .

30. Xu, B., et al., *Experimental study of a novel manifold structure of micro-channel heat exchanger.* AIP Conference Proceedings, 2013. **1547**(1): p. 68-74.

31. Boteler, L., et al., *Numerical investigation and sensitivity analysis of manifold microchannel coolers.* International Journal of Heat and Mass Transfer, 2012. **55**(25–26): p. 7698-7708.

32.   Ryu, J.H., D.H. Choi, and S.J. Kim, *Three-dimensional numerical optimization of a manifold microchannel heat sink.* International Journal of Heat and Mass Transfer, 2003. **46**(9): p. 1553-1562.

33.   Inc., W.T., *Turbo C-III® For Refrigerant Applications*, W.T. Inc., Editor. 2009, Wolverine Tube Inc.

34.   Phillips, R.J., *Forced-convection, liquid-cooled, microchannel heat sinks*, in *Dept. of Mechanical Engineering*. 1987, Massachusetts Institute of Technology.

35.   Shah, R.K. and L.A. L., *Laminar flow forced convection in ducts : a source book for compact heat exchanger analytical data*. 1978, New York: Academic Press.

36.   Incropera, F.P., *Liquid cooling of electronic devices by single-phase convection*. Vol. 1. New York: Wiley.

37.   Sieder, E.N. and G.E. Tate, *Heat Transfer and Pressure Drop of Liquids in Tubes.* Industrial & Engineering Chemistry, 1936. **28**(12): p. 1429-1435.

38.   Ayub, Z.H., *Plate Heat Exchanger Literature Survey and New Heat Transfer and Pressure Drop Correlations for Refrigerant Evaporators.* Heat Transfer Engineering, 2003. **24**(5): p. 3-16.

39.   Kumar, H., *The plate heat exchanger: Construction and design*. 1984, Institute of Chemical Engineering. p. 1275 - 1288.

40.   Incropera, F.P. and D.P. DeWitt, *Fundamentalsof Heat and Mass Transfer*. Fifth ed. 2002: Wiley.